TOPICS IN HIGH-ENERGY ASTROPHYSICS: X-RAY TIME LAGS AND GAMMA-RAY FLARES

by

John J. Kroon
A Dissertation
Submitted to the
Graduate Faculty
of
George Mason University
In Partial fulfillment of
The Requirements for the Degree
of
Doctor of Philosophy
Astrophysics

Committee:

____________________	Dr. Peter A. Becker, Dissertation Director
____________________	Dr. Joseph Weingartner, Committee Member
____________________	Dr. Mario Gliozzi, Committee Member
____________________	Dr. J.E. Lin, Committee Member
____________________	Dr. Maria Dworzecka, Department Chair
____________________	Dr. Donna M. Fox, Associate Dean, Office of Student Affairs & Special Programs, College of Science
____________________	Dr. Peggy Agouris, Dean, College of Science
Date: ____________________	Spring Semester 2016 George Mason University Fairfax, VA

Topics in High-Energy Astrophysics: X-ray Time Lags and Gamma-ray Flares

A dissertation submitted in partial fulfillment of the requirements for the degree of Doctor of Philosophy at George Mason University

By

John J. Kroon
Master of Science
George Mason University, 2013
Bachelor of Science
James Madison University, 2010

Director: Dr. Peter A. Becker, Professor
Department of Physics and Astronomy

Spring Semester 2016
George Mason University
Fairfax, VA

Dedication

I dedicate this dissertation to my father, who could not be here to see the completion of my degree and all that my career may hold. He was my greatest teacher and is my inspiration for becoming a physicist and for pursuing greatness in life and in all that I do.

Acknowledgments

I would like to thank my grandfather Garafola for his undying support and admiration of my goals and ambitions and for never doubting me.

I would like to thank the Garafola and Stamm families including, but not limited to, Steve, Peter, Ellen, Susan, Lenny, Michael, and Lauren. I would also like to thank all my grandparents as well for their support and admiration of my ambitions.

I would like to thank my brothers Lucas, Jed, Jim, and Chris and my sisters Katherine and Anna for their support in my ambitions, as well as my close friends Nhut Do, Cody Ruggles, Victoria Owen, John Keady, Nathan Secrest, Milton Ballard, Pancakes (Alex Panka), Sina Simangalam, Veronique Bonhomme, Erald Kolasi, Steven Brown, Raj Koju, Derek Fertig, Martin Robertson, Michael McClain, Hecny Gonzales, George Ashmeade, Scott Pruitt, Tiffany Lewis, and Jason Lee. I also thank all of my friends and colleagues for all their support.

I would like to thank Christine and John Mercier for the impact that they have had on my life.

I would like to thank Mary Mentzer for having my back and standing by my side. She gave me strength and joy as well as sight in ways that she probably doesn't realize. I also thank her for reviving and resuscitating me on multiple occassions. It was a pleasure working through the latter parts of my dissertation research with her by my side.

I would like to thank my math teacher Mr. J.Y. Miller for extraordinary teaching and inspiration as well as for being a true friend, kind and wise, through all the years of my life in which I have known him.

I would like to thank the Chambers family as well as Mr. Robert Henry for the significant impact that they have had on my life.

I would like to thank my mother for her support and guidance throughout all the years of my life, but especially those years of my dissertation research in which she played an extraordinary role.

I would like to thank my adviser, Dr. Peter A. Becker, and my committee members, Dr. Joseph Weingartner, Dr. Mario Gliozzi, and Dr. J.E. Lin, for absolutely outstanding guidance and patience with me as I worked through my dissertation. I could not have asked for a better committee.

Table of Contents

List of Tables

List of Figures

Abstract

TOPICS IN HIGH-ENERGY ASTROPHYSICS: X-RAY TIME LAGS AND GAMMA-RAY FLARES

John J. Kroon, PhD

George Mason University, 2016

Dissertation Director: Dr. Peter A. Becker

The Universe is host to a wide variety of high-energy processes that convert gravitational potential energy or rest-mass energy into non-thermal radiation. Arguably two of the most prevalent non-thermal emission mechanisms are bremsstrahlung and synchrotron radiation from charged particles, and the Comptonization of these radiation fields. Prevailing models of X-ray emission from accreting Black Hole Binaries (BHBs) struggle to simultaneously fit the quiescent X-ray spectrum and the transients which result in the phenomenon known as X-ray time lags. And similarly, classical models of diffusive shock acceleration in pulsar wind nebulae fail to explain the extreme particle acceleration in very short timescales as is inferred from recent γ-ray flares from the Crab nebula. In this dissertation, I develop new exact analytic models to shed light on these intriguing processes.

I take a fresh look at the formation of X-ray spectra and time lags in compact sources using a new mathematical approach in which I obtain the exact solution to the Fourier transformed transport equation. The resulting Green's function allows one to explore a variety of injection scenarios, including both monochromatic and broadband (bremsstrahlung) seed photon injection. I obtain essentially the exact solution for the dependence of the time lags on the Fourier frequency, for both homogeneous and inhomogeneous clouds. The model

can successfully reproduce both the observed time lags and the quiescent X-ray spectrum using a single set of coronal parameters, based on the impulsive injection of bremsstrahlung seed photons instead of monochromatic radiation. I show that the implied coronal radii in the new model are significantly smaller than those obtained in the Monte Carlo simulations, hence greatly reducing the coronal heating problem.

Recent bright γ-ray flares from the Crab nebula observed by AGILE and Fermi reaching GeV and even TeV energies and lasting several days challenge the contemporary model for particle acceleration in pulsar wind nebulae, specifically the diffusive shock acceleration model. Simulations indicate electron/positron pairs in the Crab nebula pulsar wind must be accelerated up to PeV energies in the presence of ambient magnetic fields with strength $B \sim 100\,\mu\mathrm{G}$. No comprehensive model has been presented that simultaneously and self-consistently explains the energetic and temporal properties of the observed flares. In this component of my dissertation research, I revisit the problem based on an analytical approach using a transport equation that includes terms describing electrostatic acceleration, stochastic wave-particle acceleration, synchrotron losses, and particle escape. I obtain an exact solution and use it to compute the resulting γ-ray synchrotron spectrum. I find that the spectra of all the *Fermi*-LAT flares from the Crab nebula can be reproduced with this model using magnetic fields that are in agreement with multi-wavelength observations.

Chapter 1: Introduction

The sky has been observed from the beginning of human civilization. Over the centuries, the observations have become more systematic and scientific. The development of telescopes facilitated great progress, but for centuries, astronomy remained limited to the optical and radio bands due to atmospheric absorption. In the 1960s, the development of space astronomy made it possible to access the entire electromagnetic spectrum, revealing for the first time the existence of a very active and dynamic universe. There are a variety of astrophysical objects (e.g. active galactic nuclei, pulsars, supernova, galactic black holes, planetary nebulae, etc.) which are host to many high-energy processes that produce non-thermal radiation extending over a broad range of photon energies.

Non-thermal radiation is far more common than Planck radiation (e.g. blackbody) in many high-energy astrophysical objects. In these sources, the electron distribution is able to reach equilibrium at temperature T_e, but there is generally not enough time or energy available to fully equilibrate the radiation field to a Planck distribution. This situation is referred to as "local thermodynamic equilibrium" (LTE), in which the electrons (and protons) have a Maxwellian distribution, but the radiation field is non-thermal, meaning that it deviates strongly from a black-body (Planck) distribution. In many cases, the high-energy radiation spectrum displays a characteristic power-law form, extending up to a maximum energy where recoil losses cause an exponential turnover.

Radiative processes such as bremsstrahlung, Compton scattering, and synchrotron are known to operate in high-energy astrophysical environments depending on what object is specifically being studied. Observational studies of a particular source allow one to develop models, which can be used to interpret observational data and extract source parameters for a given object. Hence, theoretical models for non-thermal processes can be used as important tracers of the relevant physics. Detailed theoretical models will be developed in Chapters 2-4. In this chapter, I summarize and outline the observational history and characteristics of accreting X-ray Binaries (XRBs), Active Galactic Nuclei (AGNs), and the Crab nebula. For the XRBs and AGNs, the observations are separated into spectral and temporal variability categories. In the case of the Crab nebula, I discuss the γ-ray emission detected during a sequence of strong flares from 2007-2013.

1.1 Historical Summary of Black Hole Binaries and AGNs

Black holes are defined by only three parameters, namely, mass, spin, and charge (this is referred to as the "no-hair" theorem). They range in mass by as much as nine orders of magnitude, with the supermassive black holes occupying the centers of quasars and AGNs at the high mass end of the distribution, with a mass range of about $10^{6-10}\,M_{\odot}$. Supermassive black holes, that are actively accreting, can be very luminous (from radio to hard X-rays) and were known as quasars when they were first discovered. Gravity is the "prime mover," governing the wide variety of behaviors observed from black holes of any mass, and the associated phenomena are thought to be largely scale-invariant. The less massive (galactic) black hole counterparts to AGNs include XRBs, Black Hole Binaries (BHBs), and the galactic center, Sgr A*. Here I will primarily focus on XRBs and BHBs, which are sometimes referred to as microquasars.

A prime example of a well-studied galactic X-ray source is the canonical XRB Cyg X-1, which has a wealth of observational data accumulated from a variety of X-ray observatories, starting with the launch of *UHURU* and later Skylab, ROSAT, and RXTE. Observations revealed Cyg X-1 to be a very bright source of X-rays that is variable on short timescales, strongly suggesting the presence of an accreting black hole. The rapid X-ray variability indicates activity on spatial scales comparable to the radius of the event horizon in a $\sim 10 M_{\odot}$ black hole. Accretion onto a black hole is a very efficient means of producing large quantities of energy, and is even more efficient per unit mass than nuclear fusion!

The Eddington luminosity is the maximum luminosity an accreting black hole (or star) can achieve before radiation pressure generates a strong wind that blows away the infalling matter. This limit is set at a point of hydrostatic equilibrium where the outward radiation pressure balances the inward gravitational force on the accreting matter. In spherical symmetry, it is given by

$$L_{\rm Edd} \equiv \frac{4\pi G M m_{\rm p} c}{\sigma_{\rm T}} = 1.38 \times 10^{38} \frac{M}{M_\odot} \text{ ergs s}^{-1} \ . \tag{1.1}$$

For comparison, the Sun's luminosity is $3.9 \times 10^{33}\,\text{ergs}^{-1}$, which is five orders of magnitude below its Eddington luminosity. The high-energy emission from a black hole is ultimately powered by the accretion of matter, which occurs at the rate $\dot{M}$. The dimensionless accretion rate, $\dot{m}$, plays a major role in the structure of the accretion disk and the resulting high-energy radiation spectrum, where

$$\dot{m} \equiv \frac{\dot{M}}{\dot{M}_{\rm Edd}} \ , \tag{1.2}$$

and the Eddington accretion rate, $\dot{M}_{\rm Edd}$, is defined by

$$\dot{M}_{\rm Edd} \equiv \frac{L_{\rm Edd}}{c^2} \ . \tag{1.3}$$

Accreting black holes with mass $\sim 10\ M_\odot$, such as Cyg X-1, will have an Eddington luminosity on the order of 10^{39} ergs s^{-1}. We review the observational history for XRBs and AGNs in turn below.

XRBs display a variety of spectral states, the most commonly studied are known as the high/soft and low/hard states (Tananbaum et al. 1972). These states are classified based on the relative luminosity observed in the soft and hard X-ray energy bands, typically $0.2 - 2\,$keV and $2 - 10\,$keV, respectively, although these energy channels are sometimes delineated as emission below and above $2\,$keV. *UHURU* had an energy range sensitive to $2 - 20\,$keV, which encompasses the X-ray emission from the high-temperature region of the disk, but does not include the soft X-ray and UV emission from the cooler part of the disk. However, subsequent generations of X-ray telescopes had the capability of observing soft energies. Classically, the high/soft state was defined as the spectral state in which UV and X-ray disk emission dominates (peaking around 1 keV) over the power-law component, which extends out to 100 keV (see Figure 1.1).

On the commonly used *log-log* plots the spectra of XRBs show a non-thermal power-law whose slope is known as the photon index, Γ. The spectra usually extend to energies far above the thermal component and can also exhibit a break or an exponential turnover, but are usually well-described by the power-law phenomenology. Although a variety of state classification nomenclature has developed over the decades of X-ray astronomy, ultimately the spectral state is based on the relative flux ratio of the soft and hard channels which is quantified by the value of the power-law photon index, Γ.

Using the soft energies as a probe of the inner accretion disk, the observed spectra imply the presence of an accretion flow that extends down to, or very near, the innermost stable circular orbit (ISCO). However, state transitions have been observed in which the bolometric luminosity decreases by a factor of at least a few and a prevalent radio component appears. In this state, the disk emission dramatically decreases, and a significant increase in the hard energy flux is observed (Nowak et al. 2012 arXiv:1107.2391). Therefore, this state is called the low/hard state, characterized by a photon index of $\Gamma \sim 1.7$.

At accretion rates even lower than those found in the hard state ($\dot{m} \sim 0.001 - 0.01$), we find the quiescent state. In quiescence, as the term implies, the black hole is not accreting significantly and thus its luminosity is very faint ($L \sim 10^{30-34}$ ergs s^{-1}, for a $10 M_{\odot}$ black hole). Additionally, the photon index is usually hard, $\Gamma = 1.5 - 2$. This implies both a lack of thermal flux from the disk, and the presence of a comparatively higher flux in the power-law component. It isn't clear if the quiescent state is distinct from the hard state or if it is a special case of the hard state in a lower Eddington ratio regime.

A surprisingly luminous state of GX 339-4 was observed with the *Ginga* satellite. It was characterized by a high luminosity and a steep power-law component, with a photon index

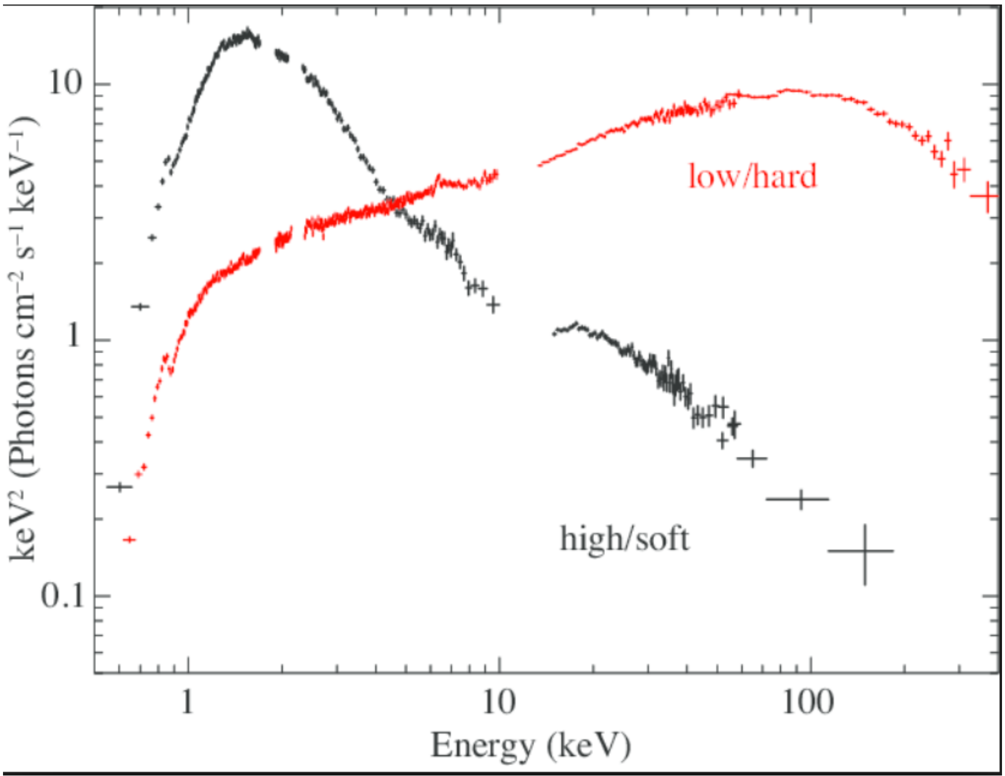

Figure 1.1: Comparison of the soft and hard state spectra for Cyg X-1.

$\Gamma \sim 2.5$ (Miyamoto et al. 1993 403-L39) and in addition, a strong thermal component. Due to the steep photon index and the high luminosity, this state was called the "very high" state. As the observational data accumulated, new state classifications rapidly proliferated, such as the intermediate, strong very high, and weak very high states.

Of particular interest in the study of XRBs is the wealth of data showing rapid variability on timescales down to seconds and even milliseconds (e.g. Nowak et al. 1999). A popular way to analyze the time variability is to generate a power spectral density (PSD) plot which shows the power generated as a function of Fourier frequency. Broad peaks in the PSD are known as quasi-periodic oscillations (QPOs) which occur at some characteristic frequency, and generally appear in certain states. The soft state is usually characterized by a lack of QPOs and a general decrease in the amplitude of the rms power (Remillard & McClintock

2006). The very high state usually has an rms power a few times larger than that in the soft state, and exhibits weak QPOs in the $0.1 - 30\,\mathrm{Hz}$ frequency range. In contrast to these states, the hard state generally displays strong QPOs and large rms amplitudes.

Remillard & McClintock (2006) combine spectral and timing properties of an accreting black hole to define a more detailed state classification scheme than the former "soft" and "hard" prescription. Their classification is based on four parameters, comprising 1) the disk fraction f which is the ratio of the disk luminosity to the total luminosity in the $2 - 20$ keV band, 2) the power-law index, Γ, 3) the rms power, r, in the PSD from $0.1 - 10$ Hz, and 4) the integrated rms amplitude a of any QPOs in the frequency range $0.1 - 30$ Hz. They also rename the traditional high/soft, low/hard, and very soft states as thermal, hard, and steep power-law, respectively. The disk fraction f in the thermal state is greater than 75%, in the hard state is less than 20%, and in the steep power-law (SPL) is less than 50%. These state definitions are thought to correspond to specific physical conditions in the accreting black hole system.

A temporal phenomenon known as time lags has been observed in which the hard energy data stream lags behind the soft energy channel (hard lag). Light curves are often Fourier transformed and timing analysis is conducted in the Fourier domain. The magnitude of the time lags increase for a given source as the separation between low and hard energy channels increases (Nowak et al. 1999). The Comptonization of soft seed photons in a hot diffuse corona is thought to be the primary mechanism (barring any intrinsic variability in the source) for the observed hard X-ray flux out to $\sim 100\,\mathrm{keV}$. The "Compton reverberation" idea set forth by Payne (1980) describes the time delay of the hard component as being due to the upscattering time from an initially soft population of seed photons. The upscattering time is inversely proportional to both the electron number density and the (constant) electron temperature. It is also directly proportional to the natural logarithm of the ratio of the hard and initial photon energies. The statistical nature of the diffusion process allows some photons to undergo fewer scattering events than others. The photons which have spent more time diffusing through the cloud will escape the system with a hard energy and thus the hard time lag distribution can be qualitatively described. Cyg X-1 has been observed to produce a time lag profile (as a function of Fourier frequency) that displays a power-law with a negative slope on the order of $1.4 - 1.7$ (Nowak et al. 1999).

Analysis of time-dependent data from accreting black holes can provide important details regarding the nature of the accretion flow such as the geometry and morphology of the system as well as the nature of the transient that produces the variability and resulting time lag signal. However, due to the inherent complexity of the phenomenon, as well as a list of unknown constraints on relevant physical parameters, studies are often forced to make a variety of simplifying assumptions. A spherical homogeneous distribution of hot electrons is a reasonable starting point for a coronal model.

The injection spectrum, location, and physical extent of the spontaneous transient has also been simplified. Miyamoto et al. (1988) employed the Compton reverberation scenario (Payne 1980) to produce theoretical time lags applied to Cyg X-1 while it was observed in its hard state. The injection spectrum was assumed to be monochromatic to model the relatively cool blackbody spectrum from the inner accretion disk. They found a flat time lag profile (independent of Fourier frequency) whose magnitude depended on the electron number density. It was interesting to see that they concluded from this study that the Compton reverberation process may not be the underlying physical mechanism producing the observed time lag profiles since their resulting time lag profile, δt, was independent of Fourier frequency, in stark contrast to the $\delta t \propto f^{-1.7}$ power-law in the data.

AGNs are known to be galaxies with an accreting supermassive black hole in the galactic center which produces copious quantities of electromagnetic radiation across a wide range of frequencies, and can have bolometric luminosities around $\sim 10^{46-49}$ ergs s^{-1}. Although most of the accretion physics from XRBs transfer to AGNs, there are some additional observational difficulties that arise when studying AGNs. Firstly, the hundreds of billions of stars that compose a galaxy, as well as the intervening dust and gas, contaminate the nuclear emission. The observed flux at the detector is also much lower than XRBs, because although supermassive black holes can be 6 to 9 orders of magnitude more massive than microquasars, they are very distant and since the flux observed varies according to the inverse square law, the observed AGN flux is much lower than that of a typical XRB.

There are a variety of spectral features that have resulted in a list of different source types such as Seyfert I and II galaxies, radio galaxies, LINERs, quasars, BL Lacs, and OVV galaxies. Some of these classifications depend on the presence of broad or narrow emission lines, highly polarized optical emission, and the ratio of radio to X-ray luminosities. A unification has taken place in which type I and II Seyfert galaxies have been proposed to be the same type of object with different inclination angles to the line of sight (Bianchi, Maiolino, Risaliti 2012).

In general, AGNs operate on much longer timescales than XRBs. State transitions can last at least a century and so a complete state change has never been observed. For example, the PSD of NGC 5506 in the $2 - 10$ keV band shows a plateau feature (red noise) from frequencies $10^{-9} - 10^{-6}$ where the spectrum turns over to a power-law of slope negative one extending down to frequencies of about 10^{-2}. This implies an X-ray emitting region of about 10^{13} cm. For a supermassive black hole with a mass of about $10^8 M_\odot$ this corresponds to only several gravitational radii.

The idea that AGNs are scaled-up versions of XRBs has been considered (e.g. Hardy et al. 2006). If this is true, then it provides a means of indirectly, but legitimately, studying the very long timescales in which AGNs operate. The very low-frequency, $\sim 10^{-10} - 10^{-7}$ Hz (although the frequency range is dependent on the black hole mass), portion of some supermassive black holes' PSDs are difficult, if not nearly impossible, to observe due to the long observation time that would be required ($\sim 10^{1-2}$ years). Several decades of frequency in PSDs are readily observed in the brighter and more rapidly varying XRBs. If conclusions drawn from careful analysis of time variability of XRBs can inform the study of AGNs, then it is important to establish confidence in the idea of scale-invariance.

This scale-invariance hypothesis tested by Hardy et al. (2006) references other studies (i.e. McHardy 1988, Edelson & Nandra 1999, Uttley, McHardy, Papadakis 2002) which showed that the PSDs contained characteristic timescales. In the study, Hardy et al. 2006, possible correlations between this break timescale, T_{B}, and other relevant parameters in the high-frequency portion of the PSDs where the slope changed from -2 to -1, was studied. They performed a parameter correlation study relating the break timescale, T_{B}, black hole mass, M_{BH}, and the bolometric luminosity, L_{bol}. By using a simple parameter grid search relating these quantities logarithmically, they constrained the scaling coefficients which would be used to map observational data from XRBs to AGNs. After obtaining these coefficients, they tested their hypothesis by including two bright XRBs (Cyg X-1 and GRS 1915+105) and found that the high-frequency portion of the PSDs were well described by the same model that fit a sample of AGNs. After statistical analysis of these results, they concluded that variability properties between AGNs and XRBs can be seen to be scale-invariant.

The time lag properties of AGNs reveal important information about the mass of the black hole when one considers the magnitude and frequency at which the hard (positive) lag becomes soft (negative; DeMarco et al. 2013). Hard lags are generally found below the break frequency in the PSDs where the red noise turns over into a power-law. At higher frequencies, the time lags can be negative indicating a "reflection" or "reverberation" in which the (soft photon) reflecting region responds to a change in continuum radiation. The lag corresponds to the light crossing time from the source to the reflector (DeMarco et al. 2013). These reverberation lags provide a mechanism to probe the shortest characteristic distance scale which in turn allows estimates on the mass of the black hole. However, this method may be limited by the spectral state and other parameters that are either poorly constrained observationally or whose significance in the framework of this mass-determination model is not understood well.

Fabian et al. (2009) published the first significant observation of such a negative (soft) lag from the source 1H0707-495. They found negative lags at frequencies higher than 6×10^{-4} Hz with a magnitude of 30 s. By considering the break frequency and the magnitude of the negative lag, they estimate a black hole mass on the order of $7 \times 10^{6} M_{\odot}$. The width of Iron L and K lines suggest a dimensionless spin parameter, a, of about 0.98 and they therefore posit that most of the reflected emission originates from within a few gravitational radii.

Over a dozen AGN sources have observed soft lags (Zoghbi & Fabian 2011, 418, 2642). What is curious, but perhaps sensible, is the remarkable qualitative parallels between the time lags and PSDs of AGNs and microquasars. Soft lags have also been observed from the microquasar GX 339-4 (Uttley et al. 2011, 414, L60). In the reverberation scenario, high-energy power-law emission from the Compton corona can impinge upon the "cold" accretion disk and down scatter to soft energies which is a possible explanation for soft lags in AGNs and microquasars.

Alternatively, the plasma may cool in response to the upscattering of the radiation, which may also lead to soft lags. Such behavior was seen in Centaurus A (Cen A) using the Monitor of All-sky X-ray Image (MAXI) in three energy bands (2-4, 4-10, and 10-20) keV. They discovered a 5 day lag between the 2-4 and 4-10 keV bands (Tachibana et al. 2016). They interpret these soft lags as due to cooling of Comptonizing electrons in a corona over the disk.

The fundamental plane (Merloni et al. 2003) relates the X-ray luminosity, the black hole mass, and the radio luminosity. The radio luminosity is thought to originate from synchrotron emission from the jet which is thought to be generated by the spin of the black hole. The fundamental plane, however, does not imply an additional free parameter to consider (i.e. black hole spin) due to the little scatter in the plot. It is possible that black hole spin rates are confined to a narrow range which would not provide sufficient variance in the data that populates the fundamental plane (Yuan & Narayan 2014). There are two classes of jets to consider: steady and episodic (Fender & Belloni 2004). Episodic jets are formed during the hard to soft state transition when the accretion rate increases, and the resulting jet is composed of discrete blobs. The steady jets form a continuous jet stream and are formed in the low luminosity hard state of XRBs such as Cyg X-1 (Fender et al. 2006). Therefore, there would be no jet power-black hole spin correlation if episodic jets are powered by the disk mechanism (Yuan et al. 2009a).

1.2 Radiative Processes

As discussed above, the radiative processes producing all the observations associated with X-ray emission from accreting XRBs can be attributed to bremsstrahlung (free-free) radiation as well as the inverse Compton scattering process. Technically the latter is a scattering phenomenon as opposed to a radiative process, however the Compton energy exchange can be classified as an emissivity. Although blackbody radiation (Planck radiation) is relevant for some of the observations presented, this phenomenon is largely irrelevant to the high energy production mechanisms of interest in the models to be presented here and so will not be discussed.

1.2.1 Compton Scattering

Compton scattering is an inelastic collision between a photon and electron. If the electron is at rest and a high energy photon collides with it, then the electron will recoil and the incident photon will lose energy and be deflected at some angle. Inverse Compton scattering can be thought of Compton scattering taking place in reverse. Since a photon cannot be at rest, consider a photon with less energy than a moving electron. In these instances, the scattering cross-section is the classical Thomson cross-section if the photon energy is much less than the electron rest mass energy. For inverse Compton scattering, the collision will transfer energy from the electron to the photon.

The astrophysical environments of interest in this application are populated by countless quantities of photons and electrons and usually with some distribution of energy for each species and each of which is assumed to have an isotropic spatial distribution. The time-independent Comptonization process has been solved and the corresponding differential equation that describes the energization process is known as the Kompane'ets equation and is given by

$$\frac{\partial n}{\partial t} = 0 = \frac{k_{\mathrm{B}} T_{\mathrm{e}}}{m_{\mathrm{e}} c^2} N_{\mathrm{e}} \sigma_{\mathrm{T}} c \frac{1}{x^2} \frac{\partial}{\partial x} \left[x^4 \left(\frac{\partial n}{\partial x} + n + n^2 \right) \right] , \tag{1.4}$$

where n is the photon number density, x is dimensionless photon energy defined as

$$x \equiv \frac{E}{m_{\rm e}c^2} \ , \tag{1.5}$$

$k_{\rm B}$ is Boltzmann's constant, $m_{\rm e}$ is the electron rest mass, c is the speed of light, $N_{\rm e}$ is the electron number density of the corona, and $\sigma_{\rm T}$ is the Thompson scattering cross-section, and E is the photon energy. The terms in the square bracket correspond to energy diffusion, electron recoil, and stimulated non-linear emission, respectively.

Payne (1980) solved this equation neglecting the non-linear term and adding a source term and a probabilistic escape formalism that depends on a geometric factor denoted by α giving

$$\frac{1}{x^2}\frac{\partial}{\partial x}\Big[x^4\Big(\frac{\partial n}{\partial x}+n\Big)\Big] - \frac{4\alpha}{y} + q(x) = 0 \ , \tag{1.6}$$

where $q(x)$ is the photon source function and

$$y \equiv \frac{4k_{\rm B}T_e}{m_ec^2}\tau^2 = N_e\sigma_T c\left(4\frac{k_{\rm B}T_e}{m_ec^2}\right)t_{\rm esc} \ , \tag{1.7}$$

τ is the optical depth of the electron cloud, $t_{\rm esc}$ is the mean escape timescale, and y is the Compton y-parameter. The Compton y-parameter quantifies the efficiency of Comptonization and is the average fractional energy change per scattering times the mean number of scatterings (before escape). There are three regimes to consider: $y \ll 1$, $y \approx 1$, and $y \gg 1$. In the first instance, the total energy of the injected radiation field is not significantly altered. Due to the product of optical depth and electron thermal energy, this regime could either be composed of an optically thin cloud or a very low temperature electron plasma, or both. In the case where the y-parameter is of order unity, the resulting spectrum will be unsaturated characterized by a power-law spectrum with a turnover energy. Lastly, if the y-parameter is significantly larger than unity, then the spectrum can be saturated and will display a Wein bump where pileup has occurred. In either case, we restrict our attention to non-relativistic thermal distributions of electrons. For a treatment of the relativistic case, see Rybicki & Lightman (1976).

The solution above the source energy is composed of a power-law, an exponential, and Kummer functions U (see Abramowitz and Stegun 1965) and is given by

$$n(x) \propto x^{-(3+p)} e^{-x} U(-3-p, -2-2p, x) \ , \tag{1.8}$$

where $p \equiv -1.5 + \sqrt{\frac{9}{4} + \frac{4\alpha}{y}}$. The asymptotic forms for the radiation intensity $I(E) = E^3 n$, where E is the photon energy, are given by

$$I(E) \propto E^{-p} \ , \tag{1.9}$$

for $E \ll k_{\rm B}T_{\rm e}$ and

$$I(E) \propto E^3 e^{-\frac{E}{k_{\rm B}T_{\rm e}}} \ , \tag{1.10}$$

if and only if $y \gtrsim 1$. In this regime, one finds that the spectral slope depends on the y-parameter and a "knee" around $E \sim k_{\rm B}T_{\rm e}$. The time-dependent solution has also been analytically solved (Payne 1980) to show the evolution of the input spectrum as it diffuses and broadens in energy space. The Kompaneet's equation is actually a special case of the Fokker-Planck equation which considers the time-dependent evolution of an input spectrum based off the physical process that modify it.

1.2.2 Thermal Bremsstrahlung Radiation

In the previous subsection we considered, briefly, the time-independent behavior of the solution to the seminal Comptonization study of the classical Kompaneet's equation. In the summary, we focused on blackbody or quasi-blackbody input spectra (the latter defined loosely by the presence of thermal spectra emitted by each annulus of an accretion disk, for example). As alluded to earlier, we wish to present the basic quantitative and qualitative aspects of thermal bremsstrahlung which play a significant role in the production of time-dependent phenomenon (to be outlined in the body of this work). The plasma that often characterize high-energy environments are composed of electrons and ions. Although most (if not all) prior models of temporal phenomenon such as time lags and PSDs rely on the injection spectrum being blackbody, it is instructive to develop a broadband injection scenario where bremsstrahlung radiation is the injected radiation field.

Bremsstrahlung comes from a German word meaning "breaking radiation" and is, in its essence, free-free emission. In this summary, we restrict our attention to nonrelativistic bremsstrahlung and consider only an isothermal finite plasma. In general, the plasma surrounding an accreting black hole, for example, will be composed of electrons and ions (protons). However, due to the significantly larger mass of a proton, its radiative contributions are negligible. Therefore, without loss of generality we consider a plasma composed purely of non-relativistic electrons.

The emission per unit time per unit volume per unit frequency is given in Rybicki & Lightman (1976) for the emission of bremsstrahlung as

$$\frac{dW}{d\omega dV dt} = \frac{16\pi e^6}{3\sqrt{3}c^3 m_{\rm e}^2 v} n_{\rm e}^2 g_{ff} \ , \tag{1.11}$$

where the electron and ion number densities are equal, the ion charge factor, $Z = 1$, and the Gaunt factor is given by

$$g_{ff}(v,\omega) = \frac{\sqrt{3}}{\pi} \ln\left(\frac{b_{\rm max}}{b_{\rm min}}\right) \ . \tag{1.12}$$

The b quantities in the logarithm are the impact parameter for an electron's interaction with an ion.

Consider an isothermal Maxwellian distribution of electrons in velocity space such that the differential probability, dP, of finding an electron in the velocity interval d^3v is

$$dP = e^{-\frac{m_e v^2}{2k_B T_e}} d^3v \ . \tag{1.13}$$

Before integrating this, one must consider the lower limit of integration. The kinetic energy of the electron must be at least equal to the photon energy that it will create. By equating these two energies and solving for the velocity we obtain $v_{\min} = \sqrt{\frac{2h\nu}{m_e}}$ where h is Planck's constant. The integration can now be performed and is expressed as

$$\frac{dW}{dV dt d\omega} = \frac{\int_{v_{\min}}^{\infty} \frac{dW}{d\omega dV dt} v^2 e^{\frac{-mv^2}{2kT}} dv}{\int_0^{\infty} v^2 e^{\frac{-mv^2}{2kT}} dv} \ , \tag{1.14}$$

where $d\omega = 2\pi d\nu$. The result obtained from Rybicki & Lightman is

$$\frac{dW}{dV dt d\omega} = \frac{2^5 \pi q^6}{3 m_e c^3} \sqrt{\frac{2\pi}{3 k_B m_e}} T^{-1/2} n_e^2 e^{-\frac{h\nu}{k_B T}} g_{ff} \ . \tag{1.15}$$

The Gaunt factor is usually of order unity, but does depend on the energy of the electron and the frequency of emission. For the applications in this study, the Gaunt factor can largely be ignored. The bremsstrahlung spectrum at low frequencies will be flat all the way down to the cut-off frequency if the medium is optically thin. For a review of bremsstrahlung absorption as well as relativistic bremsstrahlung emission, see Rybicki & Lightman (1976).

1.2.3 Blackbody Radiation

A body in thermodynamic equilibrium will emit a spectrum depending only on the equilibrium temperature. The radiated spectrum is known as blackbody radiation or a Planck spectrum, but since this spectrum depends only on the thermal temperature of the radiating body this spectrum is also sometimes referred to as thermal radiation. For a given temperature, the Planck spectrum will have a peak at a characteristic photon frequency. In this subsection, we summarize the features of this radiative process and present the relevant equations.

This subsection is motivated by the anticipated application of blackbody radiation to the hottest portion (innermost region) of an accretion disk around XRBs. Matter orbiting a black hole in the accretion disk will have orbital velocities as a function of radius from the black hole. Therefore, adjacent orbital annuli would have different orbital speeds which will cause viscous dissipation of angular momentum. This friction causes matter to radiate some of its orbital energy in the form of electromagnetic energy thereby falling inward and accreting onto the black hole.

As the gravitational force increases closer to the black hole, orbital velocities also increase according to Kepler's laws (Newtonian mechanics provide a decent approximation even in the inner regions of the accretion disk). Therefore, the hottest part of the disk will be in the innermost region. The hottest part of the disk will also be the most luminous and so disk seed photons will be dominated by the spectrum of the inner region. We now quantify the blackbody radiation spectrum.

Planck's law states that the power radiated per unit area of an emitting surface per unit solid angle, per unit frequency by a blackbody at temperature T is given by,

$$I(\nu, T) = \frac{2h\nu^3}{c^2} \frac{1}{e^{\frac{h\nu}{k_{\mathrm{B}}T}} - 1} \ , \tag{1.16}$$

where h is Planck's constant, ν is the photon frequency, c is the speed of light, k_{B} is Boltzmann's constant, and I is the spectral radiance. There is a useful relationship between the peak photon wavelength, λ_{peak}, and the blackbody temperature. This relationship is known as Wien's displacement law and is given by

$$\lambda_{\mathrm{peak}} = \frac{0.289\,\mathrm{cm\,K}}{T} \ , \tag{1.17}$$

where the temperature is given in Kelvin units and the photon wavelength is in centimeters.

The temperature of the innermost region of an accretion disk around a $M \sim 10M_\odot$ black hole is about 10^6 K which corresponds to a peak photon wavelength of $\lambda_{\rm peak} = 2.89$ nm which is a 0.43 keV photon. In the X-ray model developed in Chapter 2, we will assume that the quiescent spectrum is produced by time-independent Comptonization of continual injection of monochromatic radiation of energy $\epsilon \approx 0.1$ keV which is roughly equal to the peak photon energy in a 10^6 K blackbody spectrum when one considers the fact that a blackbody spectrum is quite narrow. In other words, the vast majority of energy radiated per second by a blackbody is tightly constrained near the peak photon energy. Therefore, the monochromatic injection paradigm is a decent and useful approximation to model Comptonization of disk seed photons.

1.3 Black Hole Accretion Models

As observational data of canonical XRBs accumulated in the early years of space-based X-ray astronomy, a wealth of theoretical models developed which attempted to explain what was being observed. Arguably one of the most impactful theoretical studies was presented in 1973 by Shakura and Sunyaev. Starting with fundamental laws of conservation of energy and angular momentum, these authors derived the structure of the blackbody-dominant accretion disk. They found angular momentum is transferred outward allowing matter to accrete via viscous dissipation, but also briefly considered roles of strong magnetic fields threading the disk. Their solutions show an optically thick, geometrically thin disk, where "thin" is defined as the limit $H/R \ll 1$, where H is the disk half-thickness and R is the accretion disk radius. They derive the disk parameters (temperature, velocity, optical depth, etc.) and compute the radiative emissivity throughout the disk for different accretion rates.

The Shakura-Sunyaev model focuses on the accretion disk and the radiation produced therein. They briefly consider a corona composed of hot evaporated disk particles that surround the disk with a slab-geometry. In general, they do not restrict their attention to a specific limiting Eddington ratio (very high or low). It is interesting to consider the accretion flow in the small Eddington ratio regime, because the disk component of the observed flux accounts only for the soft X-rays up to or around 2 keV.

The production of high-energy ($2 - 100$ keV) X-rays is generally thought to come from the Comptonization of soft seed disk photons in a surrounding hot tenuous medium known as a corona. A relatively early model for the corona was presented in 1977 by Ichimaru who builds off previous models (Thorne and Price 1975, Eardley, Lightman, Shapiro 1975) by attempting to posit an origin for the change between soft and hard spectral states. The transition from soft to hard states occurs under conditions in which the viscous heating rate is greater than the radiative cooling via bremsstrahlung.

Bremsstrahlung cooling is a two-body process and so its efficiency depends on the gas density. When viscous heating overwhelms the cooling rate the disk, at some critical radius, expands into a hot tenuous configuration which is geometrically thick and optically thin. This radiatively inefficient state is known as RIAF. In the case where the accretion of coronal matter onto the black hole is dominated by advection (the so-called ADAF), the energy contained in the plasma from viscous heating is lost into the black hole and so does not contribute to the total observed luminosity. Hence, observations have shown the low/hard state to be less luminous than the high/soft state which exists at higher accretion rates.

As accretion rates approach the Eddington ratio the gas becomes optically thick and is therefore unable to radiate the energy acquired from viscous dissipation of gravitational potential. In this scenario, the diffusion timescale for radiation in an optically thick accretion flow will exceed the advection timescale and so will be lost to the black hole. The Eddington accretion ratio is a function of both the Eddington Luminosity *and* the radiative efficiency which is a free parameter that is state and model-dependent. As the efficiency in this scenario is small, the luminosity becomes less than $0.1\dot{M}c^2$ (Begelman 1979, Begelman & Meier 1982). This is the slim disk model. The slim disk and the thin disk represent radiatively inefficient flows, but for different physical mechanisms. The thin disk is advection-dominated due to a long cooling time (or heating that dominates over bremsstrahlung radiative cooling). In this case, the inner accretion flow becomes an ADAF and is optically thin and geometrically thick. However, in the case of the slim disk model, the accretion flow is advection dominated, but due to long radiative diffusion time.

ADAFs are expected to have two temperatures, an ion and electron temperature (Ichimaru 1977). The more massive ions (protons for the case of fully ionized hydrogen) cannot radiate their energy nearly as efficiently as electrons. The hot low-density plasma cannot thermalize through Coulomb interactions especially since the advection timescale is much shorter than the cooling timescale in this radiatively inefficient state. Although this ADAF material that comprises the Compton corona is largely accepted as the quantity responsible for the power-law spectral component, a comprehensive spectral state classification scheme does not follow from considerations of ADAF physics alone.

Instead, the variety of observed spectral states has been categorized as a function of the Eddington ratio, $\dot{m} \equiv \dot{M}/\dot{M}_{\rm Edd}$. A simple model was presented by Esin et al. (1997) where the relevant features of the accretion disk and corona are qualitatively defined and represent a gradual or modular transition between the five distinct states (quiescent, low/hard, intermediate, high/soft, and very high). This model also defines a "critical" accretion rate $\dot{m}_{\rm crit} = 0.08$ which defines the approximate accretion rate at which the ADAF disappears. The authors posit that this critical rate is related to the viscosity parameter, α, via $\dot{m}_{\rm crit} \sim 1.3\alpha^2$.

Starting with the quiescent state the accretion rate in Eddington units, $\dot{m}$ is around 0.001 or at most $\dot{m} < 0.01$ and has an accretion flow composed of an inner two-temperature ADAF which extends to the disk truncation radius, $r_{\rm tr} \sim 10^2 - 10^4$ Schwarzschild radii, after which exists the standard thin accretion disk. This state is marked by ultra-low luminosity. As the accretion rate increases up to about 0.01 the black hole enters the low state, yet is still below the critical value of 0.08 and so an ADAF region is still present. However, Esin et al. (1997) classifies the low state as existing in the domain for which $0.01 \leq \dot{m} \leq \dot{m}_{\rm crit} = 0.08$ and as the accretion rate increases the radiative efficiency of the ADAF increases which increases the luminosity. The spectrum in this state is very hard and extends up to about

100 keV.

As $\dot{m}$ increases past $\dot{m}_{\rm crit}$ the ADAF shrinks due to increasingly efficient bremsstrahlung cooling and the truncation radius of the disk correspondingly decreases (moves inward toward the black hole). As the inner disk is replenished and the corona dissipates, the spectrum enters the intermediate state characterized by a hard power-law yet with increased soft emission from the disk. After the accretion rate continues to increase, the ADAF cools sufficiently to disappear and the geometrically thin disk replaces it, moving all the way down to the ISCO (or of that order). With the corona depleted and the ADAF gone, the spectrum is dominated by soft disk emission and a weak high energy tail above 10 keV. This is the soft state.

Lastly, Esin et al. (1997) discuss the very high state in which the spectrum is characterized by extraordinary luminosity (compared with the other states) and a high energy tail that extends well past 100 keV and shows no signs of breaks or turnovers even up to 1 MeV, but has a photon index of about 2.5. Although the ADAF is absent in this state, the significant high-energy emission in the tail is proposed to be due to Compton upscattering of soft seed photons in an optically thick corona (Sunyaev & Titarchuck 1980). However, Esin et al. (1997) hypothesize that the corona is denser and has a higher accretion rate in this very high state than in the high spectral state. The significant soft flux is likely due to the thin disk in a state of high accretion very close to the black hole.

A rather useful mathematical tool was presented by van der Klis et al. (1987) and was applied to Cyg X-2 and GX 5-1. The time lags were computed using a cross-spectrum or a complex cross-spectral technique in which the soft and hard energy channels are treated as data streams in the Fourier domain. The phase lag is computed by multiplying the Fourier transforms of the complex conjugate of the soft channel with the hard channel and then performing the argument operation on that product. The time lag is computed by simply dividing the phase lag by the corresponding Fourier frequency. They applied this timing analysis routine to two sources.

The time lag profile produced by Cyg X-1 in its hard state was previously modeled using the Compton reverberation idea by Miyamoto et al. (1988) and they prematurely concluded that Comptonization could not likely be the underlying mechanism since their results did not agree with the observational data. Future studies employed numerical simulations to revisit this problem with the added complexity of an electron number density that depended on radius (an inhomogeneous Compton cloud) under the prediction that the relaxation of the homogeneous corona would more successfully explain the data. This simulational study was conducted and published by Hua, Kazanas, and Cui (1999) (hereafter HKC). Furthermore, they conducted the simulation in an optically thin cloud and studied the resulting time lags as a function of the radial dependence of electron number density.

They found that the time lags from Cyg X-1 could be reproduced well if the number density was inversely proportional to the radius. Their injection spectrum was quasi-monochromatic, employing an approximation of a blackbody spectrum emitted close to the black hole from the inner disk. They studied homogeneous coronae and confirmed the Miyamoto result and also studied the resulting time lags when the electron number density fell off quickly with a $-3/2$ radial dependence. They found that this produced a time lag profile that was less steep than the data and so rejected it. The optically thin cloud that they used to model the corona of Cyg X-1 was considerably large ($\sim 10^4$ gravitational radii) which raises concerns regarding a mechanism for sufficient heating to sustain the very hot, optically thin corona at those distances. Nonetheless, their model confirmed and then expanded on the Miyamoto study by introducing an inhomogeneous corona whose number density is inversely proportional to radius. However, no author had (until now) considered the resulting time lags from an impulsive injection of *broadband* radiation from, for example, thermal bremsstrahlung radiation.

1.4 The Crab Nebula

In the year 1054 AD Chinese astronomers noticed a new star which suddenly appeared and was bright enough to be seen during the day for a few weeks. Although they did not know what they were seeing, we know it was a supernova explosion. Today the expanding supernova remnant is known as the Crab nebula. There is a rotating neutron star, or pulsar, at the center which powers the nebula. It is active across the electromagnetic spectrum and has been observed with a variety of different telescopes such as radio observations using the Very Large Array (VLA), Spitzer telescope for infrared observations, optical observations from the Hubble Space Telescope (HST), the Chandra X-ray observatory, and the *Fermi* γ-ray telescope to name a few. The Crab nebula is perhaps one of the most studied objects in the night sky. It has been studied in great detail lending to its relative close proximity of about 2 kpc and its serves as a laboratory to study particle acceleration processes in such high- energy environments.

The structure can be described by a few basic components which are the pulsar in the center, a synchrotron region or 'bubble', and a bright expanding shell of gas that makes up the well-known 'wisps' or 'filaments'. Near the pulsar there are polar jets as well as a torus that have been resolved. The size of the nebula has been seen to decrease with increasing photon energy (Buehler & Blandford (2014)). This is likely the result of high-energy electrons cooling as they diffuse and are advected outward. In the optical band the nebula is elongated along the southeast-northwest direction and is about 4.6 arcminutes by 7 arcminutes which corresponds to about 2.7 by 4.1 parsecs (pc) in physical size.

The central pulsar is known to rotate with a period of 33.6 milliseconds and is slowing down by 4.2×10^{-13} (Buehler & Blandford (2014)). The loss of rotational energy is estimated to be $\dot{E} = 5 \times 10^{38}$ergs s^{-1}, however only about 1% of this energy goes into the observed electromagnetic radiation. The spectral energy distribution (SED), shown in the figure below, shows radio emission, X-rays, and very high energy γ-rays from 100 MeV out to several TeV. The SED shows a strong peak in the UV band around a few electronvolts. A notable feature is the lower luminosity second peak at very high energy (VHE) γ-rays near a TeV which is due to inverse-Compton scattering of synchrotron emission (the so-called synchrotron self-Compton or SSC). Polarization measurements (Hester 2008) show that the observed radiation is due to synchrotron emission of high-energy electrons cooling in an

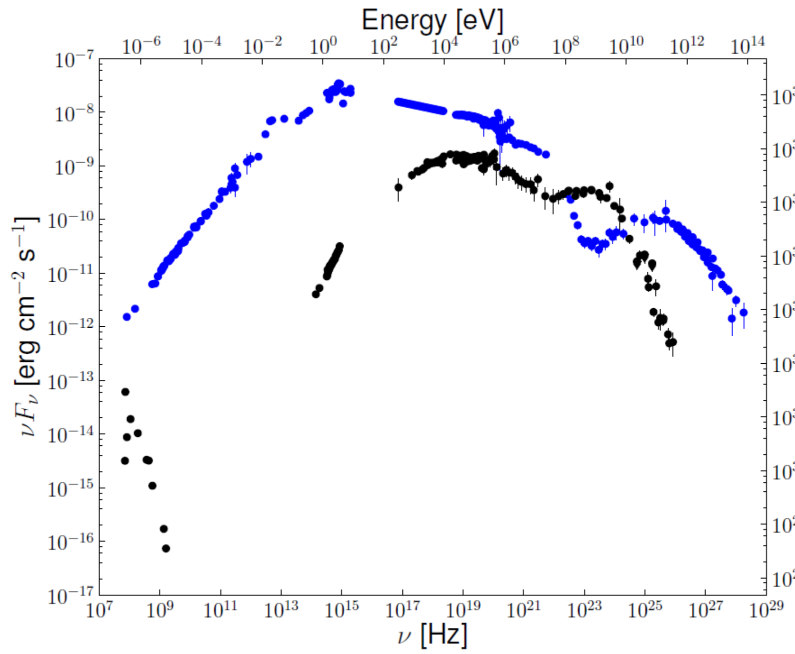

Figure 1.2: The SED of the Crab nebula found in Buehler & Blandford (2014). The black data is phase averaged emission of the pulsar and the blue is the average emission of the Crab nebula. A distance of 2 kpc is used to compute the luminosity.

ambient magnetic field.

The Crab nebula is in contrast to “shell-like” supernova remnants (SNRs) which have an obvious expanding shell whose kinetic energy is the energy source for the observed emission. The Crab, on the other hand, is powered by a “cold” (radiationless) wind of magnetized electrons and positrons generated by the pulsar. For this reason, the Crab nebula is known as a Pulsar Wind Nebula (PWN). This wind propagates outward until it interacts with the ambient medium which will create a standing shock. The torus or “inner ring” is thought to be a likely site for the production of some of the observed X-ray emission (Weisskopf et al. 2000). There are thin arcs or “wisps” past the inner ring which move outwards into the expanding nebula with speeds around half the speed of light which produce radio, optical, and X-ray emission (Buehler& Blandford 2014). These outflows are only mildly relativistic and so no significant boosting is thought to occur.

Three regions of interest are the magnetosphere extending out to the light cylinder radius ($\sim 10^8$ cm), the cold pulsar wind which extends out to the termination shock ($\sim 10^{17}$ cm), and the synchrotron bubble which extends far out into the expanding nebula. The pulsar itself is not directly observable, being only about 12 km in diameter. Its spin axis and magnetic field polar axis are not aligned which is a general feature of pulsars. The magnetic field near the surface of the neutron star is thought to be on the order $B \approx 10^{12}$ G which induces a large electric potential between the equator and the poles of about $\Delta V \approx 10^{16}$ V. The precise nature of the magnetosphere is, at this time, unknown due in part to the complicated and non-linear nature of the electrodynamic equations.

Due to the misaligned spin axis and magnetic pole axis (the “oblique” rotator) the pulsar produces alternating current sheets known as a “striped wind” that propagate outward until interacting with the ambient medium where a termination shock forms. This cold wind is described by the magnetization parameter σ which is the ratio of the magnetic energy to the kinetic energy and is thought to be much larger than unity. However, spectral modeling of the synchrotron emission produced at or near the termination shock implies a magnetization parameter much less than unity. An unsolved problem known as the “σ-problem” is how to reconcile these vast differences in the inferred value of σ.

The synchrotron bubble which starts downstream from the termination shock and extends out into the nebula is predominantly composed of radio emission. The morphology of this radio bubble is complex due in part to the large size and randomized filaments. A population of cooling electrons radiate in an ambient magnetic field of average strength $100-300$ μG. Rigorous multiwavelength studies have constrained this value to about 160 μG (Aharonian et al. 2004). They included seed photons from a variety of sources including CMB photons, infrared emission from dust and gas, as well as inverse-Compton from synchrotron. They varied the magnetic field as a free parameter until a best fit with the data was obtained, including normalization and break energies.

Usually, the Crab nebula has been a very constant source of X-rays, so stable in fact that instruments are often calibrated using certain wavebands emitted by the nebula. However, in recent years the Crab has produced extraordinary transients that have challenged our understanding of particle acceleration mechanisms. These transients take place very rapidly, showing variability on day and sub-day timescales (Abdo et al. 2011) and have spectral peaks around 400 MeV and emission as high as several GeV. Spectral analysis of the flare suggests the γ-rays are produced by synchrotron emission of a population of PeV electrons. The problem is how to explain the very short timescales in which these very high-energy electrons are accelerated. Classical shock acceleration models such as diffusive shock acceleration operate on much longer timescales. It appears the Crab has much to teach us regarding non-thermal acceleration mechanisms hitherto unconsidered.

The GeV photon energies observed are difficult to explain on energetic grounds if synchrotron losses are the mechanism for the emissivity of the electrons. The Larmor timescale represents the minimum timescale for acceleration. If one equates the Larmor timescale with synchrotron loss timescale one can obtain the theoretical maximum (peak) synchrotron energy which is about 158 MeV. Obviously this is far below what is observed. If standard MHD conditions apply, then it is difficult to explain the ample radiation above this synchrotron "burn-off" limit. More troublesome these flares become when considering the very rapid variability at these excessive γ-ray energies.

Some simple ideas have been invoked to study mechanisms that are likely the cause for these γ-ray flares. Simulation studies such as the particle-in-cell (PIC) simulations conducted by a variety of groups, such as Cerutti & Begelman, have analyzed the effects of electrostatic acceleration on the injected electrons. Disordered magnetic fields from the striped wind can be compressed at the termination shock leading to magnetic reconnection zones where an electrostatic field is induced. Electrons can be efficiently accelerated in these reconnection zones where synchrotron losses are minimal due to the vanishing magnetic field deep in the reconnection zone (Cerutti & Begelman 2011, 2012a, 2012b, 2013, 2014a, 2014b). Their focus is on the magnetic reconnection mechanism itself and the momentum distribution of electrons resulting from this acceleration paradigm. Thus, they do not reproduce the observed flare spectrum, however a solid basis for the mechanism was established.

It is unlikely that magnetic reconnection is the sole mechanism driving these flares. However, as more physics is included in a model the more complex it would become. Theoretical models could easily include a variety of physics whose analytic solutions (if they exist) can be applied to the γ-ray flare spectra. Interactions with MHD waves provide a likely acceleration component to include in an analytic study. Additionally, the resulting electron distribution would need to be computed self-consistently, taking into account synchrotron losses and particle escape from the acceleration site. In this dissertation, I present a first self-consistent and fully analytic model to explain the temporal and energetic parameters surrounding these bright γ-ray flares from the Crab nebula. The model will implement physical parameters such as the magnetic field strength that are in agreement with values obtained from rigorous observational campaigns.

1.5 Research Plan

It can be seen from this brief review of spectral and timing observations over the past several decades of X-ray astronomy that despite the complicated nature of accretion dynamics in these high-energy environments, significant progress has been made. Although where there is a plethora of observational campaigns on a variety of XRBs and AGNs, the phenomenological and numerical studies have been straining to keep up with the increasingly complex picture of accretion dynamics. It is often more insightful to apply a theoretical model to a class of observations in order to have explicit control over the physical parameters. In this fashion, it is easy to discern the significance and role that a particular quantity plays in the phenomenon under study. Throughout this dissertation, I will develop and present fully analytic solutions to a variety of observable phenomena and test the models against data.

The data with which I test my models are borrowed from previous authors' publications. Of interest here is the spectral properties of Cyg X-1 and GX 339-4 in their hard state as well as the time lags in the soft and hard energy channels. The appeal of the Comptonization model developed here is 1) an *integrated* model is derived in which the same set of cloud parameters are used to compute both the quiescent X-ray spectrum and the time lags which allows for a self-consistent model that explains the time-dependent and time-independent phenomena simultaneously 2) the models are fully analytic which makes for intimate analysis of the relevant physical parameters effortless and unambiguous 3) the technique for solving the time-dependent Compton scattering process is novel in the sense that the Fourier transformed solution does not need to be inverted before the time lags are computed, because time lag data are often presented in the Fourier frequency domain.

The rest of this document is organized as follows. First, in Chapter 2, we present a derivation of the time-dependent and time-independent photon distribution function produced from diffusion and Comptonization of seed photons in a homogeneous and inhomogeneous irrotational corona. In Chapter 3, we present the homogeneous rotating corona model. And lastly, in Chapter 4 we present an additional study of the γ-ray transients observed from the Crab nebula and develop an analytic model describing the acceleration and synchrotron losses of electrons near the termination shock of the pulsar wind nebula.

Chapter 2: X-Ray Time Lags in Accreting Galactic Black Hole Binaries

Many accretion-powered X-ray sources display rapid variability, coupled with a time-averaged spectrum consisting of a power law terminating in an exponential cutoff at high energies. The ubiquitous nature of the observations suggests a common mechanism for the spectral formation process, regardless of the type of central object (e.g. black hole, neutron star, AGNs, etc.). Over the past few decades, the interpretation of the spectral data using steady-state models has demonstrated that the power-law component is most likely due to the thermal Comptonization of soft seed photons in a hot ($\sim 10^8$ K) coronal cloud (Sunyaev & Titarchuk 1980). While the spectral models yield estimates for the coronal temperature and optical depth, they do not provide much detailed information about the geometry and morphology of the plasma. On the other hand, observations of variability, characterized by time lags and power spectral densities (PSDs), can supplement the spectral analysis, yielding crucial additional information about the structure of the inner region in the accretion flow, where the most rapid variability is generated.

In particular, the study of X-ray time lags, in which the hard photons associated with a given Fourier component arrive at the detector before or after the soft photons, provides a unique glimpse into the nature of the high-frequency variability in the inner region. Fourier time lags offer an ideal tool for studying rapid variability because, unlike short-timescale spectral snapshots, which become noisy due to the shortage of photons in small time bins, the Fourier technique utilizes all of the data in the entire observational time window, which could extend over hundreds or thousands of seconds. Hence the resulting time lag information usually has much higher significance than can be achieved using conventional spectral analysis.

2.0.1 Fourier Time Lags

The Fourier method for computing time lags from observational data streams in two energy channels was pioneered by van der Klis et al. (1987), who proposed a novel mathematical technique for extracting time lags by creating a suitable combination of the hard and soft Fourier transforms for a given value of the circular Fourier frequency, ω. The method utilizes the Complex Cross-Spectrum, denoted by $C(\omega)$, defined by

$$C(\omega) \equiv S^*(\omega)\, H(\omega) \ , \tag{2.1}$$

where S and H are the Fourier transforms of the soft and hard channel time series, $s(t)$ and $h(t)$, respectively, and S^* denotes the complex conjugate. The Fourier transforms are calculated using

$$S(\omega) = \int_{-\infty}^{\infty} e^{i\omega t} s(t) dt \ , \tag{2.2}$$

and likewise for the hard channel,

$$H(\omega) = \int_{-\infty}^{\infty} e^{i\omega t} h(t) dt \ . \tag{2.3}$$

The phase lag between the two data streams is computed by taking the argument of $C(\omega)$, which is the argument angle in the complex plane, and the associated time lag, δt, is obtained by dividing the phase lag by the Fourier frequency. Hence we have the relations

$$\delta t = \frac{\arg(C)}{2\pi\nu_f} = \frac{\arg(S^* H)}{2\pi\nu_f} \ , \tag{2.4}$$

where the Fourier frequency, ν_f, is related to the circular frequency ω via

$$\nu_f = \frac{\omega}{2\pi} \ . \tag{2.5}$$

As a simple demonstration of the time lag concept, it is instructive to consider the case where the hard and soft channels, $h(t)$ and $s(t)$, are shifted in time by a precise interval Δt, so that the two signals are related to each via

$$h(t) = s(t - \Delta t) \ , \tag{2.6}$$

where $\Delta t > 0$ would indicate a hard time lag. Next we take the Fourier transform of the hard channel time series to obtain

$$H(\omega) = \int_{-\infty}^{\infty} e^{i\omega t} h(t) dt = \int_{-\infty}^{\infty} e^{i\omega t} s(t - \Delta t) dt \ . \tag{2.7}$$

Introducing a new time variable, $t' = t - \Delta t$ with $dt' = dt$, allows us to transform the integral in Equation (2.7) to obtain

$$H(\omega) = \int_{-\infty}^{\infty} e^{i\omega(t'+\Delta t)} s(t') dt' = e^{i\omega\Delta t} S(\omega) \ . \tag{2.8}$$

It follows from Equation (2.1) that the resulting complex cross-spectrum is given by

$$C(\omega) = S^*(\omega) e^{i\omega\Delta t} S(\omega) = e^{i\omega\Delta t} |S(\omega)|^2 \ , \tag{2.9}$$

and hence the resulting time lag is (cf. Equation (2.4))

$$\delta t = \frac{\omega \Delta t}{\omega} = \Delta t \ . \tag{2.10}$$

This simple calculation confirms that the time lag computed using the Fourier method gives the correct answer when a perfect delay is introduced between the two channels, as expected. It is also important to note that time lags are only produced during a transient. We can see this by setting the hard and soft signals equal to the constants h_0 and s_0, respectively, so that $h(t) = h_0$ and $s(t) = s_0$. In this case, the resulting Fourier transforms H and S have the same phase, and consequently there is no phase lag or time lag. Hence observations of time lags necessarily imply the presence of variability in the observed signal.

2.0.2 X-Ray Time Lag Phenomenology

The fundamental physical mechanism underlying the X-ray time lag phenomenon has been debated for decades, but it is generally accepted that the time lags reflect the time-dependent scattering of a population of seed photons that are impulsively injected into an extended corona of hot electrons (e.g., van der Klis et al. 1987; Miyamoto et al. 1988). This initial population of photons gain energy as they Comptonize in the cloud, and the hard time lags are a natural consequence of the extra time that the hard photons spend in the cloud gaining energy via electron scattering before escaping. In contrast with the time lags, the time-averaged (quiescent) spectra are thought to be created as a result of the Compton scattering of *continually* injected seed photons. The time-dependent upscattering of soft input photons is discussed in detail by Payne (1980) and Sunyaev & Titarchuk (1980), who present fundamental formulas for the resulting X-ray spectrum. Since that time, many detailed models have been proposed, most of which focus on a single aspect of radiative transfer, usually by making assumptions about the physical conditions in the disk/corona system regarding the electron temperature, the input photon spectrum, and the size and optical depth of the scattering corona.

The Fourier time lags observed from accreting black-hole sources generally decrease with increasing Fourier frequency, ν_f. In the case of Cyg X-1, for example, the time lags decrease from $\sim 0.1 - 10^{-3}$ sec as ν_f increases from $\sim 0.1\,\mathrm{Hz}$ - $10^2\,\mathrm{Hz}$. Early attempts to interpret this data using simple Compton scattering models resulted in very large, hot scattering clouds, which required very efficient heating at large distances ($\sim 10^{5-6}\ GM/c^2$) from the central mass (Poutanen & Fabian 1999, Hua et al. 1999, hereafter HKC). Furthermore, the observed dependence of the time lags on the Fourier frequency was difficult to explain using a homogeneous Compton scattering model. For example, van der Klis et al. (1987) and

Miyamoto et al. (1988) found that a homogeneous corona combined with monochromatic soft photon injection resulted in time lags that are *independent* of the Fourier frequency, ν_f, in contradiction to the observations. This led Miyamoto et al. (1988) to conclude, somewhat prematurely, that thermal Comptonization could not be producing the lags. However, in the next decade, HKC and Nowak et al. (1999) developed more robust Compton simulations that successfully reproduced the observed time lags, although the large coronal radii $\sim 10^{4.5-5.5}\ GM/c^2$ continued to raise concerns regarding energy conservation and heating.

HKC computed the time lags and the time-averaged spectra for a variety of electron number density profiles, based on the injection of low-temperature blackbody seed photons at the center of the coronal cloud. They employed a two-region structure, comprising a central homogeneous zone, connected to a homogeneous or inhomogeneous outer region that extends out to several light-seconds from the central mass. In the inhomogeneous case, the electron number density, $n_e(r)$, in the outer region varied as $n_e(r) \propto r^{-1}$ or $n_e(r) \propto r^{-3/2}$. In the HKC model, the injection spectrum and the injection location were both held constant, and a zero-flux boundary condition was adopted at the center of the cloud. HKC found that only the model with $n_e(r) \propto r^{-1}$ in the outer region was able to successfully reproduce the observed dependence of the time lags on the Fourier frequency. On the other hand, in the homogeneous case, HKC confirmed the Miyamoto et al. (1988) result that the time lags are independent of the Fourier frequency, in contradiction to the observational data. This result was also verified later by Kroon & Becker (2014, hereafter KB) for the case of monochromatic photon injection into a homogenous corona.

2.0.3 Dependence on Injection Model

Despite the progress made by HKC and other authors, no successful first-principles theoretical model for the production of the observed X-ray time lags has yet emerged. In the absence of such a model, one is completely dependent on Monte Carlo simulations, which are somewhat inconvenient since the resulting time lags are not analytically connected with the parameters describing the scattering cloud. Monte Carlo simulations are also noisy at high Fourier frequency, which is the main region of interest in many applications, although this can be dealt with by adding more test particles. Compared with an analytical calculation, the utilization of Monte Carlo simulations makes it more challenging to explore different injection scenarios, such as the variation of the injection location and the seed photon spectrum.

The situation changed recently with the work of KB, who presented a detailed analytical solution to the problem of time-dependent thermal Comptonization in spherical, homogeneous scattering clouds. By obtaining the fundamental *photon Green's function* solution to the problem, they were able to explore a wide variety of injection scenarios, leading to a better understanding of the relationship between the observed time lags and the underlying physical parameters. KB verified the Miyamoto result, namely that monochromatic injection in a homogeneous cloud produces time lags that are independent of Fourier period. The magnitude of this (constant) lag depends primarily on the radius of the cloud, R, its optical thickness, τ_*, and the electron temperature, T_e. Following HKC, they employed a zero-net flux boundary condition at the center of the corona (essentially a mirror condition), so that injection could occur at any radius inside the cloud. The photon transport at the outer edge of the cloud was treated using a free-streaming boundary condition in order to properly account for photon escape. KB demonstrated that the injection radius and the shape of the injected photon spectrum play a crucial role in determining the dependence of the resulting time lags on the Fourier frequency. In particular, they established for the first time that the reprocessing of a broadband injection spectrum (e.g., thermal bremsstrahlung) can successfully reproduce most of the time lag data for Cyg X-1 and other sources.

In the study presented here, we expand on the work of KB to obtain the radiation Green's function for *inhomogeneous* scattering clouds. We also present a more detailed derivation of the *homogeneous* Green's function discussed by KB. The analytical solutions for the Fourier transform of the time-dependent Green's function in the homogeneous and inhomogeneous cases are then used to treat localized bremsstrahlung injection via integral convolution, as an alternative to the essentially monochromatic injection scenario studied by HKC. In addition to modeling the transient time lags as a result of *impulsive* soft photon injection, we also compute the time-independent X-ray spectrum radiated form the surface of the cloud as a result of *continual* soft photon injection. We show that acceptable fits to both the time-lag data and the X-ray spectral data can be obtained using a single set of cloud parameters (temperature, density, cloud radius) via application of our integrated model.

The remainder of the paper is organized as follows. In Section 2.1 we introduce the time-dependent and steady-state transport equations in spherical geometry, and we map out the general solution methods to be applied in the subsequent sections. In Section 2.2 we obtain the solution for the Fourier transform of the time-dependent photon Green's function and also the solution for the time-averaged Green's function in a homogeneous corona. In Section 2.3, we repeat the same steps for the case of an inhomogeneous corona with electron number density profile $n_e(r) \propto 1/r$. We discuss the reprocessing of thermal bremsstrahlung radiation in Section 2.4, and we apply the integrated model to Cyg X-1 and GX 339-04 in Section 2.5. Our main conclusions are reviewed and further discussed in Section 2.6 as well as Section 5.1.

2.1 Fundamental Equations

Our focus here is on understanding how time-dependent Compton scattering affects a population of seed photons as they propagate through a spherical corona of hot electrons overlying a geometrically thin, standard accretion disk. This problem was first explored using an exact mathematical approach by KB, who studied the radiative transfer occurring in a homogeneous corona. We provide further details of that work here, and we also extend the model to treat inhomogeneous spherical scattering clouds.

2.1.1 Time-Dependent Transport Equation

The time-dependent transport equation describing the diffusion and Comptonization of an instantaneous flash of N_0 monochromatic seed photons injected with energy ϵ_0 at radius r_0 and at time t_0 as they propagate through a spherical scattering corona is given by (e.g., Becker 2003),

$$\frac{\partial f_{\rm G}}{\partial t} = \frac{1}{r^2}\frac{\partial}{\partial r}\left[\kappa(r)\, r^2 \frac{\partial f_{\rm G}}{\partial r}\right] + \frac{n_e(r)\sigma_{\rm T} c}{m_e c^2}\frac{1}{\epsilon^2}\frac{\partial}{\partial \epsilon}\left[\epsilon^4\left(f_{\rm G} + kT_e \frac{\partial f_{\rm G}}{\partial \epsilon}\right)\right]$$
$$+ \frac{N_0 \delta(t-t_0)\delta(r-r_0)\delta(\epsilon-\epsilon_0)}{4\pi r_0^2 \epsilon_0^2} \ , \quad (2.11)$$

where m_e, n_e, T_e, k, $\sigma_{\rm T}$, c, and κ denote the electron mass, the electron number density, the electron temperature, Boltzmann's constant, the Thomson cross section, the speed of light, and the spatial diffusion coefficient, respectively, and $f_{\rm G}(\epsilon, r, t)$ is the radiation Green's function, describing the distribution of photons inside the cloud. The first term on the right-hand side of Equation (2.11) represents the spatial diffusion of photons through the corona, and the second term describes the redistribution in energy due to Compton scattering. The Green's function is related to the photon number density, n_r, via

$$n_r(r,t) = \int_0^\infty \epsilon^2\, f_{\rm G}(\epsilon, r, t)\, d\epsilon \ , \quad (2.12)$$

and the spatial diffusion coefficient $\kappa(r)$ is related to the electron number density $n_e(r)$ and the scattering mean free path $\ell(r)$ via

$$\kappa(r) = \frac{c}{3 n_e(r) \sigma_{\rm T}} = \frac{c\,\ell(r)}{3} \ . \quad (2.13)$$

Klein-Nishina corrections are important when the incident photon energy in the electron's rest frame approaches $\sim 500\,$keV. In our model, the electrons are essentially non-relativistic, with temperature $T_e \sim 4-7\times 10^8\,$K, and therefore the $0.1-10\,$keV photons of interest here will not be boosted into the Klein-Nishina energy range in the typical electron's rest frame. We will therefore treat the electron scattering process using the Thomson cross section throughout this study. However, we revisit this issue is Section 2.6.1 where we compare our results with previous studies that utilized the full Klein-Nishina cross section to treat the electron scattering.

2.1.2 Density Variation

In many cases of interest, the electron number density $n_e(r)$ has a power-law dependence on the radius r, which can be written as

$$n_e(r) = n_* \left(\frac{r}{R}\right)^{-\alpha} \ , \tag{2.14}$$

where R is the outer radius of the cloud, α is a constant, and $n_* \equiv n_e(R)$ is the number density at the outer edge of the cloud. The two cases we focus on here are

$$\alpha = \begin{cases} 0, & \text{homogeneous} \ , \\ 1, & \text{inhomogeneous} \ . \end{cases} \tag{2.15}$$

The homogeneous case was treated by Miyamoto (1988) and the inhomogeneous case by HKC. By combining Equations (2.13) and (2.14), we can rewrite the electron number density and the spatial diffusion coefficient as

$$n_e(r) = \frac{1}{\sigma_{\rm T}\ell_*} \left(\frac{r}{R}\right)^{-\alpha} \ , \qquad \kappa(r) = \frac{c\,\ell_*}{3} \left(\frac{r}{R}\right)^{\alpha} \ , \tag{2.16}$$

where

$$\ell_* \equiv \ell(R) = \frac{1}{n_e(R)\sigma_{\rm T}} \tag{2.17}$$

denotes the scattering mean free path at the outer edge of the corona. Substituting Equations (2.16) into Equation (2.11) yields

$$\frac{\partial f_{\rm G}}{\partial t} = \frac{c\ell_*}{3r^2}\frac{\partial}{\partial r}\left[\left(\frac{r}{R}\right)^{\alpha} r^2 \frac{\partial f_{\rm G}}{\partial r}\right] + \frac{1}{\ell_* m_e c}\left(\frac{r}{R}\right)^{-\alpha}\frac{1}{\epsilon^2}\frac{\partial}{\partial \epsilon}\left[\epsilon^4\left(f_{\rm G} + kT_e\frac{\partial f_{\rm G}}{\partial \epsilon}\right)\right]$$
$$+ \frac{N_0\delta(t-t_0)\delta(r-r_0)\delta(\epsilon-\epsilon_0)}{4\pi r_0^2\epsilon_0^2} \ . \quad (2.18)$$

The electron temperature T_e is determined by a balance between gravitational heating and Compton cooling, and one typically finds that T_e does not vary significantly in the region where most of the X-rays are produced (You et al. 2012; Schnittman et al. 2013). We therefore assume that the cloud is isothermal with T_e = constant. In this case, it is convenient to rewrite the transport equation in terms of the dimensionless energy

$$x \equiv \frac{\epsilon}{kT_e} \ . \quad (2.19)$$

We also introduce the dimensionless radius z, time p, and temperature Θ, defined, respectively, by

$$z \equiv \frac{r}{R} \ , \qquad p \equiv \frac{c\,t}{\ell_*} \ , \qquad \Theta \equiv \frac{kT_e}{m_e c^2} \ . \quad (2.20)$$

The various functions involved in the derivation can be written in terms of either the dimensional energy and radius, (ϵ, r), or the corresponding dimensionless variables (x, z), and therefore we will use these two notations interchangeably throughout the remainder of the paper. Incorporating Equations (2.19) and (2.20) into the transport equation (2.18) yields, after some algebra,

$$\frac{\partial f_{\rm G}}{\partial p} = \frac{1}{3\eta^2 z^2}\frac{\partial}{\partial z}\left(z^{2+\alpha}\frac{\partial f_{\rm G}}{\partial z}\right) + \frac{\Theta}{z^\alpha x^2}\frac{\partial}{\partial x}\left[x^4\left(f_{\rm G} + \frac{\partial f_{\rm G}}{\partial x}\right)\right]$$
$$+ \frac{N_0 \delta(x-x_0)\delta(p-p_0)\delta(z-z_0)}{4\pi z_0^2 R^3 x_0^2 \Theta^3 (m_e c^2)^3} \ , \quad (2.21)$$

where we have introduced the dimensionless "scattering parameter,"

$$\eta \equiv \frac{R}{\ell_*} = n_e(R)\sigma_{\rm T} R \ . \quad (2.22)$$

Equation (2.21) is the fundamental partial differential equation that we will use to treat time-dependent scattering in a homogeneous spherical corona with $\alpha = 0$ in Section 2.2, and time-dependent scattering in an inhomogeneous spherical corona with $\alpha = 1$ in Section 2.3.

2.1.3 Optical Depth

The scattering optical depth τ measured from the inner edge of the coronal cloud at radius $r = r_{\rm in}$ out to some arbitrary local radius r is computed using

$$\tau(r) = \int_{r_{\rm in}}^{r} n_e(r')\sigma_{\rm T} dr' = \int_{r_{\rm in}}^{r} \frac{dr'}{\ell(r')} \ , \quad (2.23)$$

where the variation of the mean-free path is given by (see Equations (2.13) and (2.14))

$$\ell(r) = \ell_* \left(\frac{r}{R}\right)^\alpha \ . \quad (2.24)$$

Combining relations, and transforming the variable of integration from r to $z = r/R$, we obtain

$$\tau(z) = \eta \int_{z_{\rm in}}^{z} \frac{dz'}{z'^\alpha} \ , \quad (2.25)$$

where

$$z_{\rm in} \equiv \frac{r_{\rm in}}{R} \tag{2.26}$$

denotes the dimensionless inner radius of the cloud.

There are three cases of interest here,

$$\tau(z) = \begin{cases} \eta\,(z^{1-\alpha} - z_{\rm in}^{1-\alpha})/(1-\alpha) \ , & \alpha \neq 1 \ , \\ \eta\,(z - z_{\rm in}) \ , & \alpha = 0 \ , \\ \eta \, \ln(z/z_{\rm in}) \ , & \alpha = 1 \ . \end{cases} \tag{2.27}$$

The overall optical thickness of the scattering cloud, denoted by τ_*, as measured from the inner radius $r = r_{\rm in}$ ($z = z_{\rm in}$) to the outer radius $r = R$ ($z = 1$), is therefore given by

$$\tau_* = \begin{cases} \eta\,(1 - z_{\rm in}^{1-\alpha})/(1-\alpha) \ , & \alpha \neq 1 \ , \\ \eta\,(1 - z_{\rm in}) \ , & \alpha = 0 \ , \\ \eta \, \ln(1/z_{\rm in}) \ , & \alpha = 1 \ . \end{cases} \tag{2.28}$$

2.1.4 Steady-State Transport Equation

The time-averaged (quiescent) X-ray spectra produced in accretion flows around black holes are generally interpreted as the result of the thermal Comptonization of soft seed photons continually injected into a hot electron corona from a cool underlying disk (see e.g. Sunyaev & Titarchuk 1980 for a review). In our interpretation, the associated X-ray time lags are the result of the time-dependent Comptonization of seed photons impulsively injected during a brief transient. Our goal in this paper is to develop an integrated model that accounts for the formation of both the time-averaged spectrum and the time lags using a single set of cloud parameters (temperature, density, radius). In our calculation of the time-averaged spectrum, we assume that $\dot{N}_0$ seed photons with energy ϵ_0 are injected per unit time into the hot corona between the inner cloud radius $r_{\rm in}$ and the outer cloud radius $r = R$ with a rate that is proportional to the local electron number density $n_e(r)$. The radial variation of the number density depends on whether the cloud is homogeneous, with n_e =constant, or inhomogeneous, with $n_e(r) \propto r^{-1}$.

In this scenario, the fundamental time-independent transport equation can be written as

$$\frac{\partial f_{\rm G}^{\rm S}}{\partial t} = 0 = \frac{1}{r^2}\frac{\partial}{\partial r}\left[\kappa(r) r^2 \frac{\partial f_{\rm G}^{\rm S}}{\partial r}\right] + \frac{n_e(r)\sigma_{\rm T} c}{m_e c^2}\frac{1}{\epsilon^2}\frac{\partial}{\partial \epsilon}\left[\epsilon^4\left(f_{\rm G}^{\rm S} + kT_e \frac{\partial f_{\rm G}^{\rm S}}{\partial \epsilon}\right)\right] + \frac{\dot{N}_0\,\delta(\epsilon-\epsilon_0) n_e(r)}{\epsilon_0^2 N_e}\,, \tag{2.29}$$

where $f_{\rm G}^{\rm S}(\epsilon, r)$ denotes the steady-state (quiescent) photon Green's function, and

$$N_e = \int_{r_{\rm in}}^{R} 4\pi r^2 n_e(r)\, dr \tag{2.30}$$

represents the total number of electrons in the region $r_{\rm in} \le r \le R$. Substituting for $n_e(r)$ and $\kappa(r)$ in Equation (2.29) using Equations (2.16) yields

$$0 = \frac{c\ell_*}{3r^2}\frac{\partial}{\partial r}\left[\left(\frac{r}{R}\right)^{\alpha} r^2 \frac{\partial f_{\rm G}^{\rm S}}{\partial r}\right] + \frac{1}{\ell_* m_e c}\left(\frac{r}{R}\right)^{-\alpha}\frac{1}{\epsilon^2}\frac{\partial}{\partial \epsilon}\left[\epsilon^4\left(f_{\rm G}^{\rm S} + kT_e\frac{\partial f_{\rm G}^{\rm S}}{\partial \epsilon}\right)\right]$$
$$+ \frac{\dot{N}_0\,\delta(\epsilon-\epsilon_0)(r/R)^{-\alpha}}{\sigma_{\rm T}\ell_*\epsilon_0^2 N_e}\,. \tag{2.31}$$

This expression can be rewritten in terms of the dimensionless parameters x, z, Θ, and η to obtain

$$0 = \frac{1}{3\eta^2 z^{2-\alpha}}\frac{\partial}{\partial z}\left(z^{2+\alpha}\frac{\partial f_{\rm G}^{\rm S}}{\partial z}\right) + \frac{\Theta}{x^2}\frac{\partial}{\partial x}\left[x^4\left(f_{\rm G}^{\rm S} + \frac{\partial f_{\rm G}^{\rm S}}{\partial x}\right)\right] + \frac{\dot{N}_0\,\delta(x-x_0)(3-\alpha)}{4\pi R^2 \eta c\,\Theta^3 (m_e c)^3 x_0^2 (1 - z_{\rm in}^{3-\alpha})}\,, \tag{2.32}$$

where we have also substituted for N_e using

$$N_e = \frac{4\pi R^3}{\sigma_{\rm T} \ell_*} \, \frac{1 - z_{\rm in}^{3-\alpha}}{3-\alpha} \ , \tag{2.33}$$

which follows from Equations (2.16) and (2.30). We assume here that $\alpha = 0$ or $\alpha = 1$.

The derivative $\partial f_{\rm G}^{\rm S}/\partial x$ exhibits a step-function discontinuity at the injection energy, $x = x_0$, due to the appearance of the function $\delta(x - x_0)$ in Equation (2.32). By integrating Equation (2.32) with respect to x over a small region surrounding the injection energy, we conclude that the derivative jump is given by

$$\lim_{\delta \to 0} \left[\frac{df_{\rm G}^{\rm S}}{dx} \right] \Bigg|_{x_0 - \delta}^{x_0 + \delta} = - \frac{\dot{N}_0 (3 - \alpha)}{4\pi R^2 \eta c \, \Theta^4 (m_e c)^3 x_0^4 (1 - z_{\rm in}^{3-\alpha})} \ . \tag{2.34}$$

We will utilize Equations (2.32) and (2.34) in Sections 2.2.1 and 2.3.1 when we compute the time-averaged X-ray spectra produced via electron scattering in homogeneous and inhomogeneous scattering coronae, respectively.

2.1.5 Fourier Transformation

In principle, all of the detailed spectral variability due to time-dependent Comptonization in the scattering corona can be computed by solving the fundamental transport equation (2.21) for a given initial photon energy/space distribution (Becker 2003). However, complete information about the variability of the spectrum is not required, or even desired, if the goal it to compare the theoretically predicted time lags δt with the observational data. Computation of the predicted time lags using Equation (2.4) requires as input the Fourier transforms of the soft and hard data streams. It is therefore convenient to analyze the time-dependent transport Equation (2.21) *directly in the Fourier domain*, rather than in the time domain. Hence one of our goals is to derive the exact solution for the Fourier transform, $F_{\rm G}$, of the time-dependent radiation Green's function, $f_{\rm G}$. We define the Fourier transform pair, $(f_{\rm G}, F_{\rm G})$, using

$$F_{\rm G}(x, z, \tilde{\omega}) \equiv \int_{-\infty}^{\infty} e^{i\tilde{\omega}p} f_{\rm G}(x, z, p)\, dp \ , \tag{2.35}$$

$$f_{\rm G}(x, z, p) \equiv \frac{1}{2\pi} \int_{-\infty}^{\infty} e^{-i\tilde{\omega}p} F_{\rm G}(x, z, \tilde{\omega})\, d\tilde{\omega} \ , \tag{2.36}$$

where the dimensionless Fourier frequency is defined by

$$\tilde{\omega} = \omega \left(\frac{\ell_*}{c} \right) = \omega t_* \ . \tag{2.37}$$

Here, $t_* = \ell_*/c$ is the "scattering time," which equals the mean-free time at the outer edge of the corona, at radius $r = R$.

We can obtain an ordinary differential equation satisfied by the Fourier transform, $F_{\rm G}$, by operating on Equation (2.21) with $\int_{-\infty}^{\infty} e^{i\tilde{\omega}p} dp$, to obtain

$$\begin{aligned} - i\tilde{\omega} z^{\alpha} F_{\rm G} = \frac{1}{3\eta^2 z^{2-\alpha}} \frac{\partial}{\partial z} \left(z^{2+\alpha} \frac{\partial F_{\rm G}}{\partial z} \right) + \frac{\Theta}{x^2} \frac{\partial}{\partial x} \left[x^4 \left(F_{\rm G} + \frac{\partial F_{\rm G}}{\partial x} \right) \right] \\ + \frac{N_0 \delta(x - x_0) \delta(z - z_0) e^{i\tilde{\omega}p_0}}{4\pi x_0^2 z_0^2 z^{-\alpha} \Theta^3 (m_e c^2)^3 R^3} \ , \end{aligned} \tag{2.38}$$

where $i^2 = -1$. Further progress can be made by noting that Equation (2.38) is separable in the energy and spatial coordinates (x, z). The technical details depend on the value of α, which determines the spatial variation of the electron number density $n_e(r)$. We therefore treat the homogeneous and inhomogeneous cases separately in Sections 2.2.2 and 2.3.2, respectively.

Due to the function $\delta(x - x_0)$ appearing in the source term in Equation (2.38), the energy derivative $\partial F_{\rm G}/\partial x$ displays a jump at the injection energy $x = x_0$, with a magnitude determined by integrating Equation (2.38) with respect to x in a small region around the injection energy. The result obtained is

$$\lim_{\delta \to 0} \left[\frac{dF_{\rm G}}{dx} \right] \Bigg|_{x_0-\delta}^{x_0+\delta} = - \frac{N_0 \, \delta(z - z_0) e^{i\tilde{\omega} p_0}}{4\pi x_0^4 \, z_0^2 z^{-\alpha} \, \Theta^4 (m_e c^2)^3 R^3} \ . \tag{2.39}$$

This expression will be used later in the computation of the expansion coefficients for the Fourier transform of the radiation Green's function resulting from time-dependent Comptonization in Sections 2.2 and 2.3.

2.1.6 Boundary Conditions

In order to obtain solutions for $f_{\rm G}^{\rm S}(\epsilon, r)$ and $F_{\rm G}(\epsilon, r, \tilde{\omega})$, we must impose suitable spatial boundary conditions at the inner edge of the cloud, $r = r_{\rm in}$, and at the outer edge, $r = R$, which correspond to the dimensionless radii $z = z_{\rm in}$ and $z = 1$, respectively. The boundary conditions we discuss below are stated in terms of the fundamental time-dependent photon Green's function, $f_{\rm G}(\epsilon, r, t)$, but they also apply to the time-averaged spectrum $f_{\rm G}^{\rm S}(\epsilon, r)$. Furthermore, we can show via Fourier transformation that the same boundary conditions also apply to the Fourier transform $F_{\rm G}(\epsilon, r, \tilde{\omega})$. Note that we can write the time-averaged X-ray spectrum $f_{\rm G}^{\rm S}$ and the Fourier transform $F_{\rm G}$ as functions of either the dimensional energy and radius, (ϵ, r), or in terms of the dimensionless variables (x, z), and therefore we will use the appropriate set of variables depending on the context.

In the Monte Carlo simulations performed by HKC, the time lags result from the reprocessing of blackbody seed photons impulsively injected at the center of the Comptonizing corona. In order to avoid unphysical sources or sinks of radiation at the center of the cloud, $r = 0$, they employed a zero-flux "mirror" inner boundary condition, which can be expressed as

$$\lim_{r \to 0} \ -4\pi r^2 \kappa(r) \frac{\partial f_{\rm G}(\epsilon, r, t)}{\partial r} = 0 \ . \tag{2.40}$$

This condition simply reflects the fact that no photons are created or destroyed at the center of the cloud after the initial flash. Following HKC, we will employ the mirror boundary condition at the center of the corona ($r = 0$) in our calculations involving a homogeneous cloud.

The scattering corona has a finite extent, and therefore we must impose a free-streaming boundary condition at the outer surface ($r = R$). Hence the distribution function $f_{\rm G}$ must satisfy the outer boundary condition

$$-\kappa(r) \frac{\partial f_{\rm G}(\epsilon, r, t)}{\partial r}\bigg|_{r=R} = c\, f_{\rm G}(\epsilon, r, t)\bigg|_{r=R} , \tag{2.41}$$

which implies that the diffusion flux at the surface is equivalent to the outward propagation of radiation at the speed of light.

When the electron distribution is inhomogeneous ($n_e(r) \propto r^{-1}$), the mirror condition cannot be applied at the center of the cloud due to the divergence of the electron number density $n_e(r)$ as $r \to 0$. In this case, we must truncate the scattering corona at a non-zero inner radius, $r = r_{\rm in}$, where we impose a free-streaming boundary condition. Physically, the inner edge of the cloud may correspond to the edge of a centrifugal funnel, or the cusp of a thermal condensation feature (Meyer & Meyer-Hofmeister 2007). The inner free-streaming boundary condition can be written as

$$-\kappa(r) \frac{\partial f_{\rm G}(\epsilon, r, t)}{\partial r}\bigg|_{r=r_{\rm in}} = -c\, f_{\rm G}(\epsilon, r, t)\bigg|_{r=r_{\rm in}} , \tag{2.42}$$

which is only applied in the inhomogeneous case. All of the boundary conditions considered here are satisfied by the fundamental time-dependent photon Green's function $f_{\rm G}(\epsilon, r, t)$, and also by the time-averaged spectrum $f_{\rm G}^{\rm S}(\epsilon, r)$, and the Fourier transform $F_{\rm G}(\epsilon, r, \tilde{\omega})$. We will apply these results in Sections 2.2 and 2.3 where we consider homogeneous and inhomogeneous cloud configurations, respectively.

2.2 Homogeneous Model

The simplest electron number density distribution of interest here is n_e =constant ($\alpha = 0$), which was first studied by Miyamoto et al. (1988). In this case we apply the mirror inner boundary condition at the center of the cloud, and hence we set $z_{\rm in} = 0$. We consider the homogeneous case in detail in this section, and obtain the exact solutions for the Fourier transform of the time-dependent photon Green's function, $F_{\rm G}(\epsilon, r, \tilde{\omega})$, and also for the associated time-averaged radiation spectrum, $f_{\rm G}^{\rm S}(\epsilon, r)$. These results were originally presented by KB in an abbreviated form. Note that KB utilized the scattering optical depth τ measured from the center of the cloud as the fundamental spatial variable, whereas we use the dimensionless radius z. However, the two quantities are simply related via Equations (2.27) and (2.28), which yield, for $\alpha = 0$ and $z_{\rm in} = 0$,

$$\tau(z) = \eta\, z \ , \qquad \tau_* = \eta \ , \tag{2.43}$$

where τ_* is the optical thickness measured from the center of the cloud to the outer edge at $z = 1$.

2.2.1 Quiescent Spectrum for $\alpha = 0$

In the homogeneous case ($\alpha = 0$), the time-independent transport equation (2.32) representing the thermal Comptonization of seed photons continually injected throughout the scattering corona can be simplified by substituting the separation functions

$$f_\lambda = K(\lambda, x)\ Y(\lambda, z) \ , \tag{2.44}$$

which yields, for $x \ne x_0$,

$$\frac{-1}{Y \eta^2 z^2} \frac{d}{dz} \left(z^2 \frac{dY}{dz} \right) = \frac{3\,\Theta}{K\, x^2} \frac{d}{dx} \left[x^4 \left(K + \frac{dK}{dx} \right) \right] = \lambda \ , \tag{2.45}$$

where λ is the separation constant. The corresponding ordinary differential equations satisfied by the spatial and energy functions Y and K are, respectively,

$$\frac{1}{z^2}\frac{d}{dz}\left(z^2\frac{dY}{dz}\right)+\lambda\,\eta^2 Y=0\ , \tag{2.46}$$

$$\frac{1}{x^2}\frac{d}{dx}\left[x^4\left(K+\frac{dK}{dx}\right)\right]-\frac{\lambda}{3\Theta}K=0\ , \tag{2.47}$$

which has been considered previously by such authors as Payne (1980), Shapiro, Lightman, and Eardley (1976), Sunyaev & Titarchuk (1980), etc.

The fundamental solution for the energy function K is given by (see Becker 2003)

$$K(\lambda,x)=(xx_0)^{-2}e^{-(x+x_0)/2}M_{2,\sigma}(x_{\rm min})W_{2,\sigma}(x_{\rm max})\ , \tag{2.48}$$

where $M_{2,\sigma}$ and $W_{2,\sigma}$ are Whittaker functions,

$$x_{\rm max}\equiv\max(x,x_0)\ ,\qquad x_{\rm min}\equiv\min(x,x_0)\ , \tag{2.49}$$

and

$$\sigma\equiv\sqrt{\frac{9}{4}+\frac{\lambda}{3\Theta}}\ . \tag{2.50}$$

The specific form in Equation (2.48) represents the solution satisfying appropriate boundary conditions at high and low energies, and it is also continuous at the injection energy, $x=x_0$, as required.

In the homogeneous configuration under consideration here, the spatial function Y must satisfy the inner "mirror" boundary condition at the origin (cf. Equation (2.40)), which can be written in terms of z as

$$\lim_{z\to 0}\ z^2\,\frac{dY(\lambda,z)}{dz}=0\ . \tag{2.51}$$

The fundamental solution for Y satisfying this condition is given by

$$Y(\lambda, z) = \frac{\sin(\eta z \sqrt{\lambda})}{\eta z} \ . \tag{2.52}$$

By virtue of Equation (2.41), the spatial function Y must also satisfy the outer free-streaming boundary condition, written in terms of the z coordinate as

$$\lim_{z \to 1} \left[\frac{1}{3\eta} \frac{dY(\lambda, z)}{dz} + Y(\lambda, z) \right] = 0 \ . \tag{2.53}$$

Substituting the form for Y given by Equation (2.52) into Equation (2.53) yields a transcendental equation for the eigenvalues λ_n that can be solved using a numerical root-finding procedure. The resulting eigenvalues λ_n are all real and positive, and the corresponding values of σ are computed by setting $\lambda = \lambda_n$ in Equation (2.50). The associated eigenfunctions, Y_n and K_n, are defined by

$$Y_n(z) \equiv Y(\lambda_n, z) \ , \quad K_n(x) \equiv K(\lambda_n, x) \ . \tag{2.54}$$

According to the Sturm-Liouville theorem, the eigenfunctions Y_n form an orthogonal basis with respect to the weight function z^2, so that (see Appendix A)

$$\int_0^1 z^2 \, Y_n(z) \, Y_m(z) \, dz = 0 \ , \qquad n \neq m \ . \tag{2.55}$$

The related quadratic normalization integrals, $\mathscr{I}_n$, are defined by

$$\mathscr{I}_n \equiv \eta^3 \int_0^1 z^2 Y_n^2(z) dz = \frac{\eta}{2} - \frac{\sin(2\eta\sqrt{\lambda_n})}{4\sqrt{\lambda_n}} \ , \tag{2.56}$$

where the final result follows from Equation (2.52).

Based on the orthogonality of the Y_n functions, we can express the time-averaged photon Green's function using the expansion

$$f_{\rm G}^{\rm S}(x, x_0, z) = \sum_{n=0}^{\infty} b_n \, K_n(x) \, Y_n(z) \ , \tag{2.57}$$

where the expansion coefficients b_n are computed using the derivative jump condition in Equation (2.34). In the case of interest here, we set $\alpha = 0$ and $z_{\rm in} = 0$ to obtain

$$\lim_{\delta \to 0} \left[\frac{df_{\rm G}^{\rm S}}{dx} \right] \Bigg|_{x_0 - \delta}^{x_0 + \delta} = - \frac{3\dot{N}_0}{4\pi R^2 \eta c \, \Theta^4 (m_e c)^3 x_0^4} \ . \tag{2.58}$$

Substituting the series expansion for the steady-state Green's function (Equation (2.57)) into Equation (2.58) yields

$$\lim_{\delta \to 0} \sum_{n=0}^{\infty} b_n Y_n(z) [K_n'(x_0 + \delta) - K_n'(x_0 - \delta)] = - \frac{3\dot{N}_0}{4\pi R^2 \eta c \, \Theta^4 (m_e c)^3 x_0^4} \ . \tag{2.59}$$

We can make further progress by eliminating K using Equation (2.48) to obtain, after some algebra,

$$\sum_{n=0}^{\infty} b_n \, Y_n(z) \, \mathscr{W}_{2,\sigma}(x_0) = - \frac{3\dot{N}_0 e^{x_0}}{4\pi R^2 \eta c \, \Theta^4 (m_e c)^3} \ , \tag{2.60}$$

where we have defined the Wronskian of the Whittaker functions using

$$\mathscr{W}_{2,\sigma}(x_0) \equiv M_{2,\sigma}(x_0) W_{2,\sigma}'(x_0) - W_{2,\sigma}(x_0) M_{2,\sigma}'(x_0) \ . \tag{2.61}$$

The Wronskian can be evaluated analytically to obtain (Abramowitz & Stegun 1970)

$$\mathscr{W}_{2,\sigma}(x_0) = -\frac{\Gamma(1+2\sigma)}{\Gamma(\sigma-3/2)} \ . \tag{2.62}$$

Combining Equations (2.60) and (2.62), we obtain

$$\sum_{n=0}^{\infty} b_n Y_n(z) \, \frac{\Gamma(1+2\sigma)}{\Gamma(\sigma-3/2)} = \frac{3\dot{N}_0 e^{x_0}}{4\pi R^2 \eta c \, \Theta^4 (m_e c^2)^3} \ . \tag{2.63}$$

Next we exploit the orthogonality of the Y_n functions with respect to the weight function z^2 by applying the operator $\int_0^1 \eta^3 z^2 Y_m(z) dz$ to both sides of Equation (2.63). According to Equation (2.55), all of the terms on the left-hand side vanish except the term with $m = n$. The result obtained for the expansion coefficient b_n is therefore

$$b_n = \frac{3\dot{N}_0 e^{x_0} \Gamma(\sigma-3/2) \mathscr{P}_n}{4\pi R^2 \eta c \, \Theta^4 (m_e c^2)^3 \Gamma(1+2\sigma) \mathscr{I}_n} \ , \tag{2.64}$$

where the integrals $\mathscr{I}_n$ are computed using Equation (2.56) and the integrals $\mathscr{P}_n$ are defined by

$$\mathscr{P}_n \equiv \int_0^1 \eta^3 z^2 Y_n(z) dz = \frac{3\eta \sin(\eta\sqrt{\lambda_n})}{\lambda_n} \ , \tag{2.65}$$

and the final result follows from application of Equation (2.53).

Combining Equations (2.57) and (2.64) yields the exact analytical solution for the time-independent photon Green's function evaluated at dimensionless energy x and dimensionless radius z resulting from the continual injection of seed photons throughout the cloud. We obtain

$$f_{\rm G}^{\rm S}(x, x_0, z) = \frac{9\dot{N}_0 e^{x_0}}{4\pi R^2 c \, \Theta^4 (m_e c^2)^3} \sum_{n=0}^{\infty} \frac{\Gamma(\sigma-3/2) \sin(\eta\sqrt{\lambda_n})}{\lambda_n \Gamma(1+2\sigma) \mathscr{I}_n} \, K_n(x) \, Y_n(z) \ , \tag{2.66}$$

where σ is computed using Equation (2.50), and Y_n and K_n are defined in Equation (2.54). This is the same result as Equation (27) from KB, once we make the identifications $\tau_* = \eta$ and $G_n(\tau) = Y_n(z)$, which arise due to the change in the spatial variable from the dimensionless radius z used here, to the scattering optical depth $\tau = \eta z$ used by KB. The time-averaged X-ray spectrum computed using Equation (2.66) is compared with the observational data for Cyg X-1 and GX 339-04 in Section 2.5.1. In Section 2.5.1, we also use asymptotic analysis to derive a power-law approximation to the exact radiation distribution given by Equation (2.66), and we show that the resulting approximate X-ray spectrum agrees closely with that obtained using the exact solution.

2.2.2 Fourier Transform for $\alpha = 0$

In the homogeneous case ($\alpha = 0$), we can substitute for the Fourier transform $F_{\rm G}$ in Equation (2.38) using the separation functions

$$F_\lambda \equiv H(\lambda, x)\, Y(\lambda, z) \ , \tag{2.67}$$

to obtain, for $x \neq x_0$,

$$-\frac{1}{Y}\frac{1}{\eta^2 z^2}\frac{d}{dz}\left(z^2 \frac{dY}{dz}\right) = \frac{3\Theta}{H x^2}\frac{d}{dx}\left[x^4\left(H + \frac{dH}{dx}\right)\right] + 3i\tilde{\omega} = \lambda \ , \tag{2.68}$$

where λ =constant. This relation can be broken into two ordinary differential equations satisfied by the spatial and energy functions Y and H. We obtain

$$\frac{1}{z^2}\frac{d}{dz}\left(z^2\frac{dY}{dz}\right) + \lambda\,\eta^2 Y = 0 \ , \tag{2.69}$$

$$\frac{1}{x^2}\frac{d}{dx}\left[x^4\left(H + \frac{dH}{dx}\right)\right] - \frac{s}{3\Theta}\,H = 0 \ , \tag{2.70}$$

where

$$s \equiv \lambda - 3i\tilde{\omega} \ . \tag{2.71}$$

In the Fourier transform case under consideration here, the spatial function Y must satisfy the mirror condition at the origin (cf. Equation (2.51)),

$$\lim_{z \to 0} \ z^2 \, \frac{dY(\lambda, z)}{dz} = 0 \ . \tag{2.72}$$

Since Equation (2.69) is identical to Equation (2.46), which we previously encountered in Section 2.2.1 in our consideration of the time-averaged spectrum produced in a homogeneous spherical corona, we conclude that the fundamental solution for Y is likewise given by (cf. Equation (2.52))

$$Y(\lambda, z) = \frac{\sin(\eta z \sqrt{\lambda})}{\eta z} \ . \tag{2.73}$$

Furthermore, Y must also satisfy the outer free-streaming boundary condition, and therefore the eigenvalues λ_n are the roots of the equation (cf. Equation (2.53))

$$\lim_{z \to 1} \left[\frac{1}{3\eta} \frac{dY(\lambda, z)}{dz} + Y(\lambda, z) \right] = 0 \ . \tag{2.74}$$

It follows that in a homogeneous corona, the Fourier eigenvalues λ_n and spatial eigenfunctions Y_n are exactly the same as those obtained in the treatment of the time-averaged spectrum. Hence we can also conclude that the spatial eigenfunctions Y_n form an orthogonal set, which motivates the development of a series expansion for the Fourier transformed radiation Green's function, $F_{\rm G}$.

Comparison of Equations (2.70) and (2.47) allows us to immediately obtain the solution for the energy function H as (cf. Equation (2.48))

$$H(\lambda, x) = (x x_0)^{-2} e^{-(x+x_0)/2} \, M_{2,\mu}(x_{\rm min}) \, W_{2,\mu}(x_{\rm max}) \ , \tag{2.75}$$

where $x_{\rm max}$ and $x_{\rm min}$ are defined in Equations (2.49), and

$$\mu \equiv \sqrt{\frac{9}{4} + \frac{s}{3\Theta}} = \sqrt{\frac{9}{4} + \frac{\lambda - 3i\tilde{\omega}}{3\Theta}} \ . \tag{2.76}$$

Following the same steps used in Section 2.2.1 for the development of the solution for the time-averaged radiation Green's function $f_{\rm G}^{\rm S}$, we can construct a series representation for the Fourier transform $F_{\rm G}$ by writing

$$F_{\rm G}(x, z, \tilde{\omega}) = \sum_{n=0}^{\infty} a_n \, H_n(x) \, Y_n(z) \ , \tag{2.77}$$

where the eigenfunctions Y_n and H_n are defined by

$$Y_n(z) \equiv Y(\lambda_n, z) \ , \quad H_n(x) \equiv H(\lambda_n, x) \ . \tag{2.78}$$

To solve for the expansion coefficients, a_n, we substitute Equation (2.77) into Equation (2.39) with $\alpha = 0$ to obtain

$$\lim_{\delta \to 0} \sum_{n=0}^{\infty} a_n Y_n(z) [H'(x_0 + \delta) - H'(x_0 - \delta)] = - \frac{N_0 \, \delta(z - z_0) e^{i\tilde{\omega} p_0}}{4\pi z_0^2 x_0^4 \Theta^4 (m_e c^2)^3 R^3} \ , \tag{2.79}$$

or, equivalently,

$$\sum_{n=0}^{\infty} a_n \, Y_n(z) \, \mathscr{W}_{2,\mu}(x_0) = - \frac{N_0 \, \delta(z - z_0) e^{i\tilde{\omega} p_0} e^{x_0}}{4\pi z_0^2 \Theta^4 (m_e c^2)^3 R^3} \ , \tag{2.80}$$

where the Wronskian is given by

$$\mathscr{W}_{2,\mu}(x_0) \equiv M_{2,\mu}(x_0) W'_{2,\mu}(x_0) - W_{2,\mu}(x_0) M'_{2,\mu}(x_0) = - \frac{\Gamma(1 + 2\mu)}{\Gamma(\mu - 3/2)} \ . \tag{2.81}$$

Substituting for the Wronskian in Equation (2.80) using Equation (2.81) and applying the operator $\int_0^1 \eta^3 z^2 Y_m(z) dz$ to both sides of the equation, we can utilize the orthogonality of the spatial eigenfunctions Y_n to obtain for the expansion coefficients a_n the result

$$a_n = \frac{N_0 \, e^{i\tilde{\omega}p_0} e^{x_0} \eta^3 \Gamma(\mu - 3/2) Y_n(z_0)}{4\pi\Theta^4 (m_e c^2)^3 R^3 \Gamma(1 + 2\mu) \mathscr{I}_n} \ , \tag{2.82}$$

where the quadratic normalization integrals $\mathscr{I}_n$ are defined in Equation (2.56).

By combining Equations (2.77) and (2.82), we find that the exact solution for the Fourier transformed radiation Green's function, $F_{\rm G}$, is given by the expansion

$$F_{\rm G}(x, z, \tilde{\omega}) = \frac{N_0 \, e^{i\tilde{\omega}p_0} e^{x_0} \eta^3}{4\pi R^3 \Theta^4 (m_e c^2)^3} \sum_{n=0}^{\infty} \frac{\Gamma(\mu - 3/2)}{\Gamma(1 + 2\mu) \mathscr{I}_n} Y_n(z_0) Y_n(z) H_n(x) \ , \tag{2.83}$$

with μ computed using Equation (2.76), and Y_n and H_n given by Equations (2.78). This result agrees with Equation (16) from KB once we note the change in the spatial variable from z to $\tau = \eta z$, with $G_n(\tau) = Y_n(z)$, $\tau_* = \eta$, and $\ell_0 = R/\eta$. In the case of the exact solution for the time-averaged electron distribution derived in Section 2.2.1, we are able to derive an accurate approximation using asymptotic analysis (see Section 2.5.1). However, due to the complex nature of the series in Equation (2.83), it is not possible to extract useful asymptotic representations for the Fourier transform. Hence Equation (2.83) is the key result that will be utilized to compute the Fourier transform and the associated time lags for a spherical homogeneous cloud in Section 2.5.2.

2.3 Inhomogeneous Model

In the previous section, we have presented detailed solutions for the time-averaged spectrum and for the Fourier transform of the time-dependent photon Green's function describing the diffusion and Comptonization of photons in a spherical, homogeneous scattering cloud. Another interesting possibility is a coronal cloud with an electron number density distribution that varies as $n_e(r) \propto r^{-1}$, which was considered by HKC, and corresponds to $\alpha = 1$ in Equations (2.16). In this case, the dimensionless radius z is related to the scattering optical depth τ via (see Equations (2.27) and (2.28))

$$\tau(z) = \eta \, \ln(z/z_{\rm in}) \ , \qquad \tau_* = \eta \, \ln(1/z_{\rm in}) \ , \tag{2.84}$$

where τ_* is the optical thickness measured from the inner radius $r = r_{\rm in}$ $(z = z_{\rm in})$ to the outer radius $r = R$ $(z = 1)$. In this section, we obtain the analytical solutions for the time-averaged spectrum $f_{\rm G}^{\rm S}$ and for the Fourier transform $F_{\rm G}$ for the case with $n_e(r) \propto r^{-1}$.

2.3.1 Quiescent Spectrum for $\alpha = 1$

The steady-state transport equation (2.32) describes the formation of the time-averaged X-ray spectrum via the thermal Comptonization of seed photons continually injected throughout a scattering corona with an electron number density profile given by $n_e(r) \propto r^{-\alpha}$. In the inhomogeneous case with $\alpha = 1$, this equation can be solved using the separation form

$$f_\lambda = K(\lambda, x) \ y(\lambda, z) \ , \tag{2.85}$$

to obtain, for $x \neq x_0$,

$$\frac{-1}{y\eta^2 z} \frac{d}{dz} \left(z^3 \frac{dy}{dz} \right) = \frac{3\,\Theta}{K\,x^2} \frac{d}{dx} \left[x^4 \left(K + \frac{dK}{dx} \right) \right] = \lambda \ , \tag{2.86}$$

where λ =constant. The associated ordinary differential equations in the spatial and energy coordinates are, respectively,

$$\frac{1}{z} \frac{d}{dz} \left(z^3 \frac{dy}{dz} \right) + \lambda \, \eta^2 y = 0 \ , \tag{2.87}$$

$$\frac{1}{x^2}\frac{d}{dx}\left[x^4\left(K+\frac{dK}{dx}\right)\right]-\frac{\lambda}{3\Theta}\,K=0\ . \tag{2.88}$$

Since Equation (2.88) is identical to Equation (2.47), it follows that the solution for the energy function K is given by (cf. Equation (2.48))

$$K(\lambda,x)=(xx_0)^{-2}e^{-(x+x_0)/2}M_{2,\sigma}(x_{\rm min})W_{2,\sigma}(x_{\rm max})\ , \tag{2.89}$$

where

$$\sigma\equiv\sqrt{\frac{9}{4}+\frac{\lambda}{3\Theta}}\ . \tag{2.90}$$

The fundamental solutions for the spatial functions, y, are given by the power-law forms

$$y(\lambda,z)=C_1 z^{-1-\sqrt{1-\eta^2\lambda}}+z^{-1+\sqrt{1-\eta^2\lambda}}\ , \tag{2.91}$$

where C_1 is a superposition constant determined by applying the outer free-streaming boundary condition given by Equation (2.41). For the inhomogeneous case with $\alpha=1$, the outer boundary condition implies that y must satisfy the equation

$$\lim_{z\to 1}\left[\frac{z}{3\eta}\frac{dy(\lambda,z)}{dz}+y(\lambda,z)\right]=0\ . \tag{2.92}$$

The corresponding result obtained for C_1 is

$$C_1=\frac{3\eta-1+\sqrt{1-\eta^2\lambda}}{1-3\eta+\sqrt{1-\eta^2\lambda}}\ . \tag{2.93}$$

The next step is to apply the *inner* free-streaming boundary condition, given by Equation (2.42). Stated in terms of z, we obtain for $\alpha = 1$ the condition

$$\lim_{z \to z_{\rm in}} \left[\frac{z}{3\eta} \frac{dy(\lambda, z)}{dz} - y(\lambda, z) \right] = 0 \ , \tag{2.94}$$

where $z_{\rm in} = r_{\rm in}/R$ is the dimensionless inner radius of the cloud. Equation (2.94) is satisfied only for certain discrete values of λ, which are the eigenvalues λ_n. The eigenvalues obtained are all positive real numbers. The resulting global functions y therefore satisfy both the inner and outer free-streaming boundary conditions. Once the eigenvalues λ_n are determined, the corresponding spatial and energy eigenfunctions are defined by

$$y_n(z) \equiv y(\lambda_n, z) \ , \quad K_n(x) \equiv K(\lambda_n, x) \ . \tag{2.95}$$

We show in Appendix A that the spatial eigenfunctions y_n form an orthogonal set with respect to the weight function z, so that

$$\int_{z_{\rm in}}^{1} z\, y_n(z)\, y_m(z)\, dz = 0 \ , \qquad n \neq m \ . \tag{2.96}$$

We can therefore express the steady-state photon Green's function $f_{\rm G}^{\rm S}$ using the expansion

$$f_{\rm G}^{\rm S}(x, x_0, z) = \sum_{n=0}^{\infty} c_n\, K_n(x)\, y_n(z) \ . \tag{2.97}$$

To solve for the expansion coefficients, c_n, we substitute Equation (2.97) into Equation (2.34), with $\alpha = 1$, to obtain

$$\lim_{\delta \to 0} \sum_{n=0}^{\infty} c_n y_n(z) [K_n'(x_0 + \delta) - K_n'(x_0 - \delta)] = - \frac{\dot{N}_0}{2\pi R^2 \eta c\, \Theta^4 (m_e c)^3 x_0^4 (1 - z_{\rm in}^2)} \ . \tag{2.98}$$

Eliminating K using Equation (2.48) yields

$$\sum_{n=0}^{\infty} c_n y_n(z)\, \mathscr{W}_{2,\sigma}(x_0) = -\frac{\dot{N}_0 e^{x_0}}{2\pi R^2 \eta c\, \Theta^4 (m_e c)^3 (1 - z_{\rm in}^2)} \ , \tag{2.99}$$

where the Wronskian $\mathscr{W}_{2,\sigma}(x_0)$ is defined in Equation (2.61). By combining Equations (2.99) and (2.62) we obtain

$$\sum_{n=0}^{\infty} c_n y_n(z)\, \frac{\Gamma(1+2\sigma)}{\Gamma(\sigma - 3/2)} = \frac{\dot{N}_0 e^{x_0}}{2\pi R^2 \eta c\, \Theta^4 (m_e c)^3 (1 - z_{\rm in}^2)} \ . \tag{2.100}$$

We can exploit the orthogonality of the spatial basis functions $y_n(z)$ with respect to the weight function z by operating on Equation (2.100) with $\int_{z_{\rm in}}^1 z\, y_m(z) dz$ to obtain

$$c_n = \frac{\dot{N}_0 e^{x_0} \Gamma(\sigma - 3/2) \mathscr{L}_n}{2\pi R^2 \eta c\, \Theta^4 (m_e c^2)^3 \mathscr{I}_n \Gamma(1+2\sigma)(1 - z_{\rm in}^2)} \ , \tag{2.101}$$

where we have made the definitions

$$\mathscr{I}_n \equiv \int_{z_{\rm in}}^1 z\, y_n^2(z) dz \ , \qquad \mathscr{L}_n \equiv \int_{z_{\rm in}}^1 z\, y_n(z) dz \ . \tag{2.102}$$

The final result for the steady-state (quiescent) photon Green's function in the inhomogeneous case with $\alpha = 1$ is obtained by combining Equations (2.97) and (2.101), which yields

$$f_{\rm G}^{\rm S}(x, x_0, z) = \frac{\dot{N}_0 e^{x_0}}{2\pi R^2 \eta c\, \Theta^4 (m_e c^2)^3} \sum_{n=0}^{\infty} \frac{\Gamma(\sigma - 3/2) \mathscr{L}_n}{\mathscr{I}_n \Gamma(1+2\sigma)(1 - z_{\rm in}^2)} K_n(x)\, y_n(z) \ , \tag{2.103}$$

with σ computed using Equation (2.90), and y_n and K_n given by Equations (2.95). The time-averaged X-ray spectrum computed using Equation (2.103) is compared with observational data for two specific sources in Section 2.5.1, and an accurate asymptotic approximation is also derived in that section.

2.3.2 Fourier Transform for $\alpha = 1$

In the inhomogeneous case with $\alpha = 1$, we can substitute for the Fourier transform in Equation (2.38) using the separation functions

$$F_\lambda \equiv K(\lambda, x) \; g(\lambda, z) \; , \tag{2.104}$$

to obtain, for $x \neq x_0$,

$$-\frac{1}{g}\frac{1}{\eta^2 z}\frac{d}{dz}\left(z^3 \frac{dg}{dz}\right) - 3i\tilde{\omega}z = \frac{3\Theta}{Kx^2}\frac{d}{dx}\left[x^4\left(K + \frac{dK}{dx}\right)\right] = \lambda \; , \tag{2.105}$$

where λ is the separation constant. This relation yields two ordinary differential equations satisfied by the spatial and energy functions g and K, given by

$$\frac{1}{z}\frac{d}{dz}\left(z^3 \frac{dg}{dz}\right) + \eta^2\Big(\lambda + 3i\tilde{\omega}z\Big)g = 0 \; , \tag{2.106}$$

$$\frac{1}{x^2}\frac{d}{dx}\left[x^4\left(K + \frac{dK}{dx}\right)\right] - \frac{\lambda}{3\Theta}K = 0 \; . \tag{2.107}$$

Equation (2.107) is identical to Equation (2.47), and therefore we can immediately conclude that the solution for the energy function K is given by

$$K(\lambda, x) = (x x_0)^{-2} e^{-(x+x_0)/2} M_{2,\sigma}(x_{\rm min}) W_{2,\sigma}(x_{\rm max}) \; , \tag{2.108}$$

where

$$\sigma \equiv \sqrt{\frac{9}{4} + \frac{\lambda}{3\Theta}} \ . \tag{2.109}$$

One significant new feature in the inhomogeneous case with $\alpha = 1$ under consideration here is that the eigenvalues λ_n are now functions of the Fourier frequency $\tilde{\omega}$, which stems from the appearance of $\tilde{\omega}$ in Equation (2.106). It follows that σ is also a function of $\tilde{\omega}$ through its dependence on λ (see Equation (2.50)). This inconvenient mixing of variables forces us to generate a separate list of eigenvalues for each sampled frequency. The fundamental solution for the spatial function g is given by the superposition

$$g(\lambda, z) = \frac{1}{z}\left[C_2 J_{-\nu}(2\eta\sqrt{3i\tilde{\omega}z}) + J_{\nu}(2\eta\sqrt{3i\tilde{\omega}z})\right] \ , \tag{2.110}$$

where $J_\nu(z)$ denotes the Bessel function of the first kind, and we have made the definition

$$\nu \equiv 2\sqrt{1 - \eta^2\lambda} \ . \tag{2.111}$$

The superposition constant C_2 is computed by applying the outer free-streaming boundary condition, which can be written as (cf. Equation (2.92))

$$\lim_{z \to 1}\left[\frac{z}{3\eta}\frac{dg(\lambda, z)}{dz} + g(\lambda, z)\right] = 0 \ . \tag{2.112}$$

The result obtained for C_2 is

$$C_2 = \frac{(2 - 6\eta + \nu)J_\nu(2\eta\sqrt{3i\tilde{\omega}}) - 2\eta\sqrt{3i\tilde{\omega}}J_{\nu-1}(2\eta\sqrt{3i\tilde{\omega}})}{(6\eta - 2 + \nu)J_{-\nu}(2\eta\sqrt{3i\tilde{\omega}}) + 2\eta\sqrt{3i\tilde{\omega}}J_{-\nu-1}(2\eta\sqrt{3i\tilde{\omega}})} \ . \tag{2.113}$$

Next we must apply the inner free-streaming boundary condition given by (cf. Equation (2.94))

$$\lim_{z \to z_{\rm in}} \left[\frac{z}{3\eta} \frac{dg(\lambda, z)}{dz} - g(\lambda, z) \right] = 0 \ , \tag{2.114}$$

where $z_{\rm in} = r_{\rm in}/R$. The roots of Equation (2.114) are the eigenvalues λ_n, and the associated global functions g satisfy both the inner and outer free-streaming boundary conditions. The corresponding spatial and energy eigenfunctions are given by

$$g_n(z) \equiv g(\lambda_n, z) \ , \quad K_n(x) \equiv K(\lambda_n, x) \ . \tag{2.115}$$

As demonstrated in Appendix A, the spatial eigenfunctions g_n are orthogonal with respect to the weight function z, and therefore

$$\int_{z_{\rm in}}^{1} z \, g_n(z) \, g_m(z) \, dz = 0 \ , \qquad n \neq m \ . \tag{2.116}$$

It follows that we can express the Fourier transformed radiation Green's function, $F_{\rm G}$, using the expansion (cf. Equation (2.77))

$$F_{\rm G}(x, z, \omega) = \sum_{n=0}^{\infty} d_n \, K_n(x) \, g_n(z) \ . \tag{2.117}$$

The expansion coefficients d_n can be computed by applying the derivative jump condition given by Equation (2.39), which yields for $\alpha = 1$

$$\lim_{\delta \to 0} \left[\frac{dF_{\rm G}}{dx} \right] \Bigg|_{x_0 - \delta}^{x_0 + \delta} = - \frac{N_0 \, \delta(z - z_0) e^{i \tilde{\omega} p_0}}{4 \pi x_0^4 \, z_0^2 z^{-1} \, \Theta^4 (m_e c^2)^3 R^3} \ . \tag{2.118}$$

Combining Equations (2.117) and (2.118) gives the result

$$\lim_{\delta \to 0} \sum_{n=0}^{\infty} d_n g_n(z)[K'(x_0+\delta) - K'(x_0-\delta)] = -\frac{N_0\,\delta(z-z_0)e^{i\tilde{\omega}p_0}}{4\pi x_0^4\, z_0^2 z^{-1}\,\Theta^4(m_e c^2)^3 R^3}\ , \tag{2.119}$$

or, equivalently,

$$\sum_{n=0}^{\infty} d_n g_n(z)\,\mathscr{W}_{2,\sigma}(x_0) = \sum_{n=0}^{\infty} -d_n g_n(z)\,\frac{\Gamma(1+2\sigma)}{\Gamma(\sigma-3/2)} = -\frac{N_0\,\delta(z-z_0)e^{i\tilde{\omega}p_0}e^{x_0}}{4\pi z_0^2 z^{-1}\,\Theta^4(m_e c^2)^3 R^3}\ , \tag{2.120}$$

where we have utilized Equations (2.61) and (2.62) for the Wronskian $\mathscr{W}_{2,\sigma}(x_0)$.

We can solve for the expansion coefficients d_n by utilizing the orthogonality of the spatial eigenfunctions g_n with respect to the weight function z. Applying $\int_{z_{\rm in}}^1 z g_m(z) dz$ to both sides of Equation (2.120), we obtain, after some algebra,

$$d_n = \frac{N_0 e^{i\tilde{\omega}p_0}e^{x_0}\Gamma(\sigma-3/2)g_n(z_0)}{4\pi\Theta^4(m_e c^2)^3 R^3\Gamma(1+2\sigma)\mathscr{K}_n}\ , \tag{2.121}$$

where the quadratic normalization integrals, $\mathscr{K}_n$, are defined by

$$\mathscr{K}_n \equiv \int_{z_{\rm in}}^1 z g_n^2(z) dz\ . \tag{2.122}$$

The final result for the Fourier transform $F_{\rm G}$ of the photon Green's function $f_{\rm G}$ obtained by combining Equations (2.117) and (2.121) is

$$F_{\rm G}(x,z,\tilde{\omega}) = \frac{N_0\,e^{i\tilde{\omega}p_0}e^{x_0}}{4\pi R^3\Theta^4(m_e c^2)^3}\sum_{n=0}^{\infty}\frac{\Gamma(\sigma-3/2)}{\Gamma(1+2\sigma)\mathscr{K}_n}\,g_n(z_0)\,g_n(z)\,K_n(x)\ , \tag{2.123}$$

with σ evaluated using Equation (2.109), and g_n and K_n given by Equations (2.115). This exact analytical solution can be used to generate theoretical predictions of the Fourier transformed data streams in two different energy channels in order to simulate the time lags created in a spherical scattering corona with an electron number density profile that varies as $n_e(r) \propto r^{-1}$. As in the case of the homogeneous Fourier transform discussed in Section 2.2.2, it is not possible to extract useful asymptotic representations for the inhomogeneous Fourier transform due to the complex nature of the sum appearing in Equation (2.123).

2.4 Bremsstrahlung Injection

The investigations carried out by Miyamoto (1988), HKC, and KB show that the impulsive injection of monochromatic seed photons into a homogeneous Comptonizing corona cannot produce the observed dependence of the X-ray time lags on the Fourier frequency. A major advantage of the analytical method we employ here is that *the radiation Green's function we obtain can be convolved with any desired seed photon distribution as a function of radius r, energy ϵ, and time t.* This flexibility stems from the fact that the transport equation is a linear partial differential equation. A source spectrum of particular interest is a flash of bremsstrahlung seed photons injected on a spherical shell at radius $r = r_0$. We may expect the observed variability in this case to be qualitatively different from the behavior associated with a monochromatic flash of seed photons, because the bremsstrahlung flash represents *broadband* radiation. We anticipate that the prompt escape of high-energy photons from the bremsstrahlung seed distribution may cause a profound shift in the dependence of the observed X-ray time lags on the Fourier period.

Since the fundamental transport equation governing the radiation field is linear, it follows that we can compute the time-dependent spectrum f resulting from any seed photon distribution Q that is an arbitrary function of time, energy, and radius using the integral convolution

$$f(\epsilon, r, t) = \int_0^\infty \int_{r_{\rm in}}^R \int_0^\infty 4\pi r_0^2 \epsilon_0^2 f_{\rm G}(\epsilon, \epsilon_0, r, r_0, t, t_0)\, Q(\epsilon_0, r_0, t_0) N_0^{-1} \, d\epsilon_0 \, dr_0 \, dt_0 \ , \qquad (2.124)$$

where $4\pi r_0^2 \epsilon_0^2 Q(\epsilon_0, r_0, t_0)\, dr_0\, dt_0\, d\epsilon_0$ gives the number of photons injected in the energy range $d\epsilon_0$, radius range dr_0, and time range dt_0 around the coordinates (ϵ_0, r_0, t_0). In the case of optically thin bremsstrahlung injection, the seed photons are created as a result of a local instability in the coronal plasma, due to, for example, a magnetic reconnection event, or the passage of a shock. It follows that the photon distribution resulting from localized, impulsive injection of bremsstrahlung radiation at radius $r = r_0$ can be written as

$$f_{\rm brem}(\epsilon, r, t) = \int_{\epsilon_{\rm abs}}^{\infty} f_{\rm G}(\epsilon, \epsilon_0, r, r_0, t, t_0)\, Q_{\rm brem}(\epsilon_0) N_0^{-1}\, d\epsilon_0 \ , \tag{2.125}$$

where $\epsilon_{\rm abs}$ denotes the low-energy cutoff due to free-free self-absorption in the source plasma, and the bremsstrahlung source function, $Q_{\rm brem}$, for fully-ionized hydrogen is given by (Rybicki & Lightman 1979)

$$Q_{\rm brem}(\epsilon_0) = \frac{A_0}{\epsilon_0}\, e^{-\epsilon_0/kT_e} \ , \tag{2.126}$$

where

$$A_0 = \frac{2^5 \pi q^6}{3 h m_e c^3} \left(\frac{2\pi}{3 k m_e}\right)^{1/2} V_0\, t_{\rm rad}\, T_e^{-1/2} n_e^2(r_0) \ . \tag{2.127}$$

Here, V_0 denotes the radiating volume, $t_{\rm rad}$ is the radiating time interval, and q is the electron charge. The bremsstrahlung source function is normalized so that $Q_{\rm brem}(\epsilon_0)\, d\epsilon_0$ gives the number of photons injected in the energy range between ϵ_0 and $\epsilon_0 + d\epsilon_0$.

The low-energy self-absorption cutoff, $\epsilon_{\rm abs}$, appearing in Equation (2.125), depends on the temperature and density of the plasma experiencing the transient that produces the flash of bremsstrahlung seed photons. The density of the unstable plasma is expected to be higher than that in the surrounding corona, due to either shock compression or a thermal instability. We do not analyze this physical process in detail here, and instead we treat $\epsilon_{\rm abs}$ as a free parameter in our model, although a more detailed physical picture could be developed in future work.

Changing variables from (ϵ, r, t) to (x, z, p) and applying Fourier transformation to both sides of Equation (2.125), we obtain

$$F_{\rm brem}(x, z, z_0, \tilde{\omega}) = A_0\, N_0^{-1} \int_{x_{\rm abs}}^{\infty} F_{\rm G}(x, x_0, z, z_0, \tilde{\omega})\, x_0^{-1} e^{-x_0}\, dx_0 \ , \tag{2.128}$$

where $x_{\rm abs} = \epsilon_{\rm abs}/(kT_e)$ is the dimensionless self-absorption energy. The function $F_{\rm G}$ in Equation (2.128) represents the Fourier transformation of the time-dependent photon Green's function for either the homogeneous or inhomogeneous cases, given by either Equation (2.83) or Equation (2.123), respectively. The integral with respect to x_0 can be carried out analytically, and the exact solutions are given by

$$F_{\rm brem}(x, z, z_0, \tilde{\omega}) = \frac{e^{i\tilde{\omega}p_0}\eta^3 A_0\, e^{-x/2}}{4\pi R^3 \Theta^4 (m_e c^2)^3 x^2} \sum_{n=0}^{\infty} \begin{cases} \dfrac{\Gamma(\mu - 3/2) Y_n(z_0) Y_n(z)}{\Gamma(1+2\mu)\mathscr{I}_n}\, B(\mu, x), & \alpha = 0, \\ \dfrac{\Gamma(\sigma - 3/2) g_n(z_0) g_n(z)}{\Gamma(1+2\sigma)\, \eta^3 \mathscr{K}_n}\, B(\sigma, x), & \alpha = 1, \end{cases} \tag{2.129}$$

where σ and μ are given by Equations (2.50) and (2.76), respectively, and the integral function $B(\lambda, x)$ is defined by

$$B(\lambda, x) \equiv \int_{x_{\rm abs}}^{\infty} e^{-x_0/2} x_0^{-3} M_{2,\lambda}(x_{\rm min}) W_{2,\lambda}(x_{\rm max})\, dx_0 \ . \tag{2.130}$$

We show in Appendix B that $B(\lambda, x)$ can be evaluated analytically to obtain the closed-form result

$$B(\lambda, x) = \begin{cases} W_{2,\lambda}(x)[I_M(\lambda, x) - I_M(\lambda, x_{\rm abs})] - M_{2,\lambda}(x) I_W(\lambda, x)\,, & x \ge x_{\rm abs}\,, \\ -M_{2,\lambda}(x) I_W(\lambda, x_{\rm abs})\,, & x \le x_{\rm abs}\,, \end{cases} \tag{2.131}$$

where the functions I_M and I_W are defined by

$$I_M(\lambda, x) \equiv \frac{x^{-2}e^{-x/2}}{\lambda + \frac{3}{2}} \left(M_{1,\lambda}(x) + \frac{3}{\lambda + \frac{1}{2}} \left\{ M_{0,\lambda}(x) + \frac{2}{\lambda - \frac{1}{2}} \left[M_{-1,\lambda}(x) + \frac{1}{\lambda - \frac{3}{2}} M_{-2,\lambda}(x) \right] \right\} \right) , \tag{2.132}$$

and

$$I_W(\lambda, x) \equiv x^{-2}e^{-x/2} \Bigg[- W_{1,\lambda}(x) + 3W_{0,\lambda}(x) - 6W_{-1,\lambda}(x) + 6W_{-2,\lambda}(x) \Bigg] . \tag{2.133}$$

Section 2.5.2, we will use this result to study the implications of broadband (bremsstrahlung) seed photon injection as an alternative to monochromatic injection for the production of the observed X-ray time lags in homogeneous and inhomogeneous scattering coronae.

2.5 Astrophysical Applications

In the previous sections, we have obtained the exact mathematical solution for the steady-state photon Green's function, $f_{\rm G}^{\rm S}$, describing the X-ray emission emerging from a scattering corona as a result of the *continual distributed* injection of monochromatic seed photons. We have also obtained the exact solution for the Green's function, $F_{\rm G}$, describing the Fourier transform of the X-ray spectrum resulting from the *impulsive localized* injection of monochromatic seed photons into the corona. By convolving the solution for $F_{\rm G}$ with the bremsstrahlung source term, we were also able to derive the exact solution for the bremsstrahlung Fourier transform, $F_{\rm brem}$.

The availability of these various solutions for the steady-state X-ray spectrum and for the Fourier transform resulting from impulsive injection allows us to explore a wide variety of injection scenarios, while maintaining explicit control over the physical parameters describing the astrophysical objects of interest, such as the temperature, the electron number density, and the cloud radius. Our goal here is to develop "integrated models," in which the coupled calculations of the time-averaged X-ray spectrum and the transient Fourier X-ray time lags are based on the *same set* of physical parameters (temperature, density, radius) for the scattering corona. We believe that this integrated approach represents a significant step forward by facilitating the study of a broad range of parameter space using an analytical model.

2.5.1 Comparison with Observed Time-Averaged Spectra

The time-averaged X-ray spectrum emanating from the outer surface of the cloud results from the continual distributed injection of soft photons from a source with a rate that is proportional to the local electron number density. Thus, there is no specific injection radius for the time-averaged model. The detailed solutions we have obtained describe the radiative transfer occurring in either a homogeneous cloud, or in an inhomogeneous cloud in which the electron number density varies with radius as $n_e(r) \propto r^{-1}$.

Application of the integrated model begins with a comparison of the observed time-averaged X-ray spectrum with the theoretical steady-state photon flux measured at the detector, $\mathcal{F}_\epsilon(\epsilon)$, computed using the relation

$$\mathcal{F}_\epsilon(\epsilon) = \left(\frac{R}{D}\right)^2 c\, \epsilon^2 f_{\rm G}^{\rm S}\left(\frac{\epsilon}{kT_e}, x_0, z\right)\bigg|_{z=1} , \tag{2.134}$$

where D is the distance to the source, R is the radius of the corona, c is the speed of light, and the solution for the steady-state spectrum, $f_{\rm G}^{\rm S}(x, x_0, 1)$, at the surface of the cloud is evaluated using either Equation (2.66) for the homogeneous case or Equation (2.103) for the inhomogeneous case. In our computations of the time-averaged X-ray spectra, the seed photon energy is frozen at $\epsilon_0 = 0.1$ keV in order to approximate the effect of the continual injection of blackbody photons from a "cool" accretion disk with temperature $T \sim 10^6$ K.

The temperature parameter $\Theta = kT_e/m_e c^2$ (Equation (2.20)) and the scattering parameter $\eta = R/\ell_*$ (Equation (2.22)) determine the slope of the power-law component of the time-averaged spectrum, and also the frequency of the high-energy exponential cutoff created by recoil losses. In the inhomogeneous case, the shape of the time-averaged spectrum also depends on the dimensionless inner radius, $z_{\rm in} = r_{\rm in}/R$, at which the inner free-streaming boundary condition is imposed. We vary the values of Θ, η, and $z_{\rm in}$ until good qualitative agreement with the shape of the observed steady-state X-ray spectrum is achieved. Once the values of Θ, η, and $z_{\rm in}$ are determined, the photon injection rate, $\dot{N}_0$, is then computed by matching the theoretical flux level with the observed time-averaged spectrum.

Exact Time-Averaged X-ray Spectra

In Figure 2.1, we plot the theoretical time-averaged (quiescent) X-ray spectra measured at the detector, $\mathcal{F}_\epsilon(\epsilon)$, computed using the *homogenous* corona model, with distributed seed photon injection, evaluated by combining Equations (2.66) and (2.134). The plots also include a comparison with the observed X-ray spectra for Cyg X-1 and GX 339-04. The data for Cyg X-1 were reported by Cadolle Bel et al. (2006) and cover the observation period MJD 52617-52620, and the data for GX 339-04 were reported by Cadolle Bel et al. (2011) and cover the observation period MJD 55259.9-55261.1. Both sources were observed by INTEGRAL in the low/hard state. The model parameters are summarized in Table 2.1, and the corresponding homogeneous eigenvalues are plotted in Figure 2.3. The time-averaged X-ray spectra obtained for the *inhomogeneous* corona model, computed by combining Equations (2.103) and (2.134), are plotted and compared with the observational data in Figure 2.2, and the corresponding inhomogeneous eigenvalues are depicted in Figure 2.7.

We find that the observed time-averaged spectra can be fit equally well using either the homogeneous or inhomogeneous cloud models. Furthermore, the homogeneous and inhomogeneous models have similar temperatures and cloud radii. This behavior illustrates the fact that the time-averaged spectrum mainly depends on the cloud temperature and the Compton y-parameter, and is not directly dependent on the accretion geometry, as discussed in detail by Sunyaev & Titarchuk (1980).

It is interesting to compare our model parameters with those used by HKC, who computed the time-averaged spectra of Cyg X-1 for a variety of electron density profiles, similar

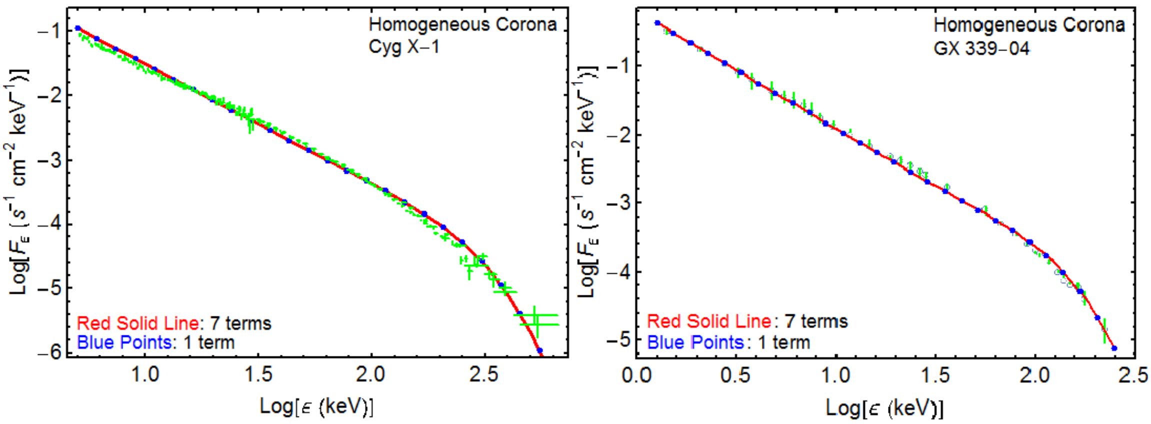

Figure 2.1: Theoretical quiescent X-ray spectra observed at the detector, for a homogeneous corona, with constant electron number density, n_e, computed by combining Equations (2.66) and (2.134). Results are presented for Cyg X-1 (left panel) and GX 339-04 (right panel), along with observational data taken from Cadolle Bel et al. (2006) and Cadolle Bel et al. (2011), respectively. Both sources were observed in the low/hard state using INTEGRAL. To analyze the convergence of the series, we plot the results obtained using only the first term in the series, or using the first 7 terms. The convergence is extremely rapid for both sources.

to the homogeneous and inhomogeneous cloud configurations studied here. They employed a scattering cloud with a homogeneous central region, coupled with either a homogeneous or inhomogeneous outer region. The HKC cloud has a scattering optical thickness $\tau_* = 1$ and an electron temperature of $kT_e = 100\,\mathrm{keV}$, whereas we obtain $\tau_* \sim 2 - 3$ and $kT_e \sim 60\,\mathrm{keV}$ (see Table 2.1). The differences between our model parameters and theirs could be due to the fact that the observational data analyzed here corresponds to the low/hard state of Cyg X-1, whereas HKC compared their model with spectral data from Ling et al. (1997), acquired while Cyg X-1 was in its high/soft state, when the source is known to have a lower optical depth (e.g., Frontera et al. 2001; Malzac 2012; Del Santo et al. 2013). Furthermore, the values of τ_* and T_e that we obtain are very close to those found by Malzac et al. (2008), who also considered the low/hard state of Cyg X-1.

In Tables 2.2 and 2.3 we compare the energy injection rate for the seed photons in our model, L_{inj}, with the time-averaged X-ray luminosity, L_{X}, observed in the low/hard state

Table 2.1: Input Model Parameters

Source	Model	η	Θ	kT_e(keV)	$\epsilon_{\rm abs}$(keV)	$z_{\rm in}$	z_0	t_*(s)
Cyg X1	Homogeneous	2.50	0.120	61.3	1.60	0.00	1.00	0.04
Cyg X1	Inhomogeneous	1.40	0.122	62.4	1.60	0.12	0.91	0.065
GX 339	Homogeneous	4.00	0.064	32.7	0.01	0.00	0.78	0.038
GX 339	Inhomogeneous	2.20	0.064	32.7	0.01	0.10	0.60	0.090

Table 2.2: Auxillary Model Parameters

Source	Model	$\dot{N}_0\,(\mathrm{s}^{-1})$	$y_{\rm eff}$	$\tau_{\rm eff}$	τ_*	λ_0	$R\,(\mathrm{cm})$	$D\,(\mathrm{kpc})$
Cyg X1	Homogeneous	2.00×10^{46}	1.20	1.58	2.50	1.20	3.00×10^9	2.4
Cyg X1	Inhomogeneous	2.70×10^{46}	1.17	1.55	2.97	1.25	2.73×10^9	2.4
GX 339	Homogeneous	5.75×10^{46}	1.48	2.40	4.00	0.52	4.56×10^9	8.0
GX 339	Inhomogeneous	7.00×10^{46}	1.51	2.43	5.07	0.51	5.94×10^9	8.0

Table 2.3: Luminosity Values

Source	Model	$L_{\rm inj}\,(\mathrm{ergs\,s^{-1}})$	$L_{\rm X}\,(\mathrm{ergs\,s^{-1}})$
Cyg X1	Homogeneous	3.20×10^{36}	2.20×10^{37}
Cyg X1	Inhomogeneous	4.33×10^{36}	2.20×10^{37}
GX 339	Homogeneous	9.21×10^{36}	6.28×10^{37}
GX 339	Inhomogeneous	1.12×10^{37}	6.28×10^{37}

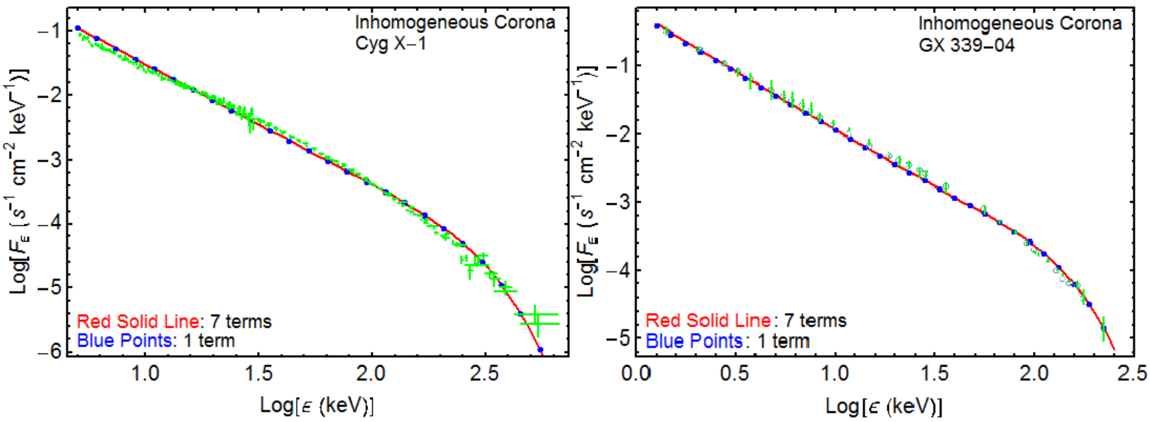

Figure 2.2: Same as Figure 2.1, except we plot the quiescent X-ray spectra emanating from an inhomogeneous corona, with electron density profile $n_e(r) \propto r^{-1}$. The results were obtained by combining Equations (2.103) and (2.134). The convergence is very rapid.

for the two sources studied here, Cyg X-1 and GX 339-04. The injection luminosity is computed using $L_{\rm inj} = \epsilon_0 \dot{N}_0$, where $\dot{N}_0$ is the photon injection rate and the seed photon energy is $\epsilon_0 = 0.1\,$keV. The values for $L_{\rm X}$ were taken from Cadolle Bel et al. (2006) for Cyg X-1, and from Cadolle Bel et al. (2011) for GX 339-04. We see that the injection luminosity is $\sim 10\%$ of the observed X-ray luminosity, which is consistent with the values we have obtained for the effective Compton y-parameter.

Approximate Power-Law X-ray Spectra

The X-ray spectra plotted in Figures 2.1 and 2.2 have a power-law form that extends up to the exponential cutoff, where electron recoil losses become significant. This suggests the existence of an approximate, asymptotic power-law solution, valid in the domain $x \lesssim 1$ (Rybicki & Lightman 1979). Figures 2.1 and 2.2 also include a convergence study, where we compare the results obtained for the steady-state spectra, $f_{\rm G}^{\rm S}$, using only the first $(n = 0)$ term in the series with the fully-converged result obtained using the first 7 terms in the series. The results are essentially indistinguishable, which establishes that the convergence of the series is extremely rapid. The power-law shape observed for $x \lesssim 1$, combined with the rapid

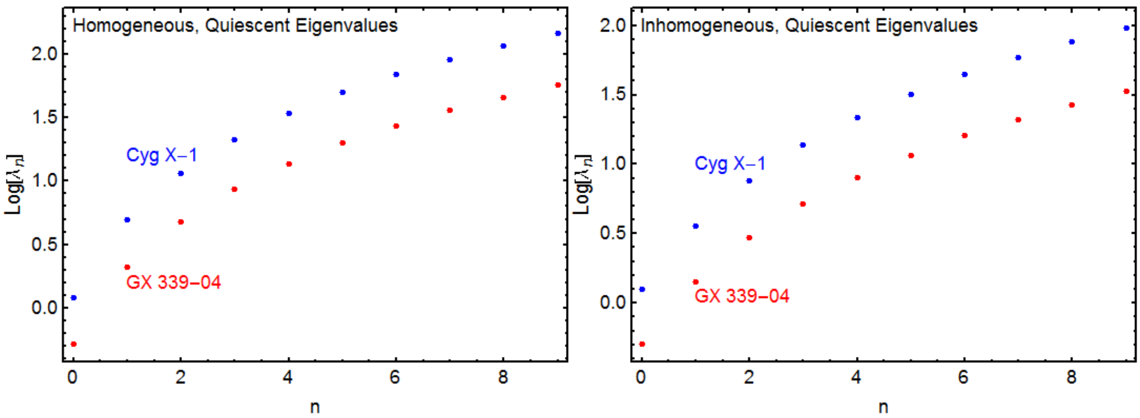

Figure 2.3: Real eigenvalues, λ_n, for the quiescent spectrum radiated by a homogeneous corona (left panel), and an inhomogeneous corona (right panel). All of the eigenvalues are positive.

convergence, suggest that we can derive an asymptotic power-law solution by analyzing the first term in the expansion for the observed flux. By analogy with previous work on thermal Comptonization, we expect that the properties of the approximate analytical solution will shed light on the relationship between the first eigenvalue, λ_0, which determines the spectral slope, and the effective Compton y-parameter for the model. We derive the approximate asymptotic power-law solution below, for both the homogeneous and inhomogeneous cloud configurations.

We are interested in photon energies well above the injection energy, $\epsilon_0 = 0.1\,\text{keV}$, and therefore it follows that $x > x_0$. In this case, we can combine Equations (2.48) and (2.66) to express the time-averaged X-ray spectrum in the homogeneous corona as

$$f_{\rm G}^{\rm S}(x, x_0, z) = \frac{9\dot{N}_0 e^{(x_0-x)/2}(xx_0)^{-2}}{4\pi R^2 c\,\Theta^4(m_e c^2)^3} \sum_{n=0}^{\infty} \frac{\Gamma(\sigma - 3/2)\sin(\eta\sqrt{\lambda_n})}{\lambda_n \Gamma(1+2\sigma)\mathscr{I}_n}\, Y_n(z) M_{2,\sigma}(x_0) W_{2,\sigma}(x)\ . \tag{2.135}$$

The corresponding result obtained by combining Equations (2.89) and (2.103) in the inhomogenous case is

$$f_{\rm G}^{\rm S}(x,x_0,z)=\frac{\dot{N}_0 e^{(x_0-x)/2}(xx_0)^{-2}}{2\pi R^2\eta c\,\Theta^4(m_e c^2)^3}\sum_{n=0}^{\infty}\frac{\Gamma(\sigma-3/2)\mathscr{L}_n}{\mathscr{I}_n\Gamma(1+2\sigma)(1-z_{\rm in}^2)}\,y_n(z)M_{2,\sigma}(x_0)W_{2,\sigma}(x)\ . \tag{2.136}$$

Based on Figure 2.2, we observe that the domain of the power-law shape is $x_0 < x \lesssim 1$. This suggests that we can employ Equations (13.1.32), (13.1.33), (13.5.5), and (13.5.6) from Abramowitz & Stegun (1970) to implement the small-argument asymptotic form for the Whittaker functions M and W.

We will only evaluate the $n=0$ term in the sum, since it represents a converged result, according to the results plotted in Figure 2.1. After some algebra, the approximate solution obtained in the homogeneous case is

$$f_{\rm G}^{\rm S}(x,x_0,z)\approx\frac{9\dot{N}_0\,x_0^{\sigma_0-3/2}}{8\pi R^2 c\,\Theta^4(m_e c^2)^3}\,\frac{\sin(\eta\sqrt{\lambda_0})}{\lambda_0\sigma_0\mathscr{I}_0}\,\frac{\sin(\eta z\sqrt{\lambda_0})}{\eta z}\,x^{-\sigma_0-3/2}\ , \tag{2.137}$$

where (see Equation (2.50))

$$\sigma_0\equiv\sqrt{\frac{9}{4}+\frac{\lambda_0}{3\Theta}}\ . \tag{2.138}$$

Likewise, in the inhomogeneous case, we obtain

$$f_{\rm G}^{\rm S}(x,x_0,z)\approx\frac{\dot{N}_0\,x_0^{\sigma_0-3/2}}{4\pi R^2\eta c\,\Theta^4(m_e c^2)^3}\,\frac{\mathscr{L}_0\,y_0(z)}{\mathscr{I}_0\sigma_0(1-z_{\rm in}^2)}\,x^{-\sigma_0-3/2}\ . \tag{2.139}$$

By substituting either Equation (2.137) or (2.139) into Equation (2.134), and setting $z=1$, we can compute the corresponding approximate X-ray spectrum, $\mathcal{F}_\epsilon(\epsilon)$, observed at the detector. These results are plotted and compared with the exact solutions in Figure 2.4, and it is clear that the power-law approximation is extremely accurate below the exponential cutoff energy, as expected.

We can obtain further insight into the physical significance of our approximate power-law solutions by comparing our work with previous results. First, we note that within the regime of interest here, $x \lesssim 1$, and therefore electron recoil losses are negligible. This suggests that we can define an effective y-parameter by comparing our work with the corresponding analytical solutions that neglect recoil losses. This situation was treated by Rybicki & Lightman (1979), who obtained power-law solutions to the Kompaneets equation by utilizing an escape-probability formalism for the spatial photon transport, as an alternative to the spatial diffusion operator employed here. In our solutions, given by Equations (2.137) and (2.139), the power-law index is equal to $-\sigma_0 - 3/2$. Setting our result equal to the index m given by Equation (7.76) from Rybicki & Lightman (1979) yields

$$-\sigma_0 - \frac{3}{2} = -\frac{3}{2} - \sqrt{\frac{9}{4} + \frac{4}{y_{\rm eff}}} \ , \tag{2.140}$$

where $y_{\rm eff}$ is the effective Compton y-parameter and Θ is the dimensionless temperature ratio. Using Equation (2.138) to substitute for σ_0 and solving for $y_{\rm eff}$, we find that

$$y_{\rm eff} = \frac{12\,\Theta}{\lambda_0} \ . \tag{2.141}$$

The values obtained for $y_{\rm eff}$ and λ_0 in our calculations of the time-averaged X-ray spectra resulting from distributed (density-weighted) seed photon injection are reported in Table 2.2. We generally find that $y_{\rm eff} \sim 1$, corresponding to unsaturated Comptonization, which is consistent with the power-law spectra plotted in Figures 2.1 and 2.2 (e.g., Sunyaev & Titarchuk 1980).

It is also interesting to relate the first eigenvalue, λ_0, to the effective optical depth, $\tau_{\rm eff}$, traversed by the photons as they propagate through the scattering corona, and ultimately escape. Referring to the simplified escape-probability model analyzed by Rybicki & Lightman

(1979), we can apply their Equation (7.41a) to write, in the optically thick case,

$$y = 4\,\Theta\,\tau_{\rm eff}^2 \ . \tag{2.142}$$

Setting $y = y_{\rm eff}$ and combining Equations (2.141) and (2.142), we find that $\tau_{\rm eff}$ and λ_0 are related via

$$\tau_{\rm eff} = \sqrt{\frac{3}{\lambda_0}} \ . \tag{2.143}$$

The results obtained for $\tau_{\rm eff}$ are listed in Table 2.2. Comparing the values of $\tau_{\rm eff}$ with the values for τ_* in Table 2.1, we conclude that $\tau_{\rm eff} \sim 0.5\,\tau_*$, which reflects the fact that the seed photon injection is density weighted, rather than being localized at the center of the cloud. Hence, on average, photons traverse less optical depth than is given by τ_*, which is measured from the cloud center.

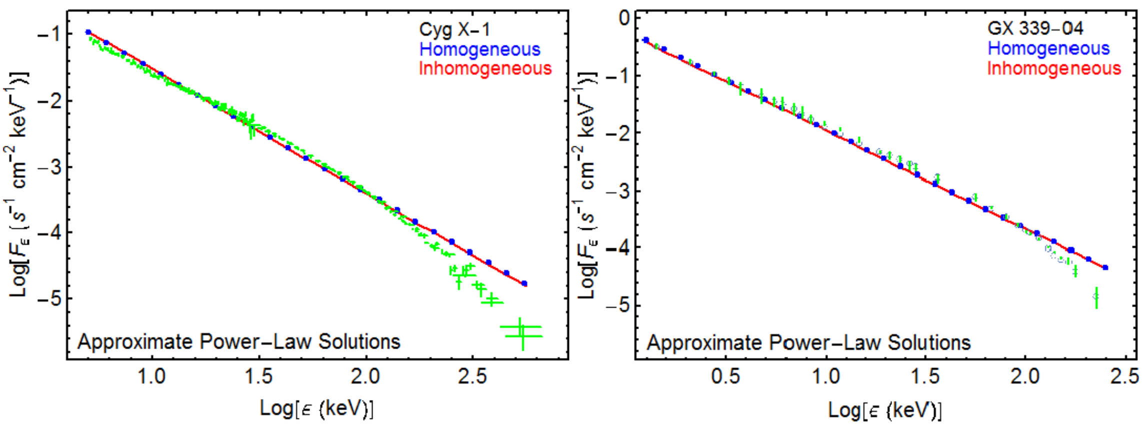

Figure 2.4: Approximate power-law X-ray spectra computed using Equation (2.134) combined with Equation (2.137) for the homogeneous corona (blue filled circles) or Equation (2.139) for the inhomogeneous corona (red solid lines). The results are compared with the observational data for Cyg X-1 (left panel) and GX 339-04 (right panel). See the discussion in the text.

2.5.2 Comparison with Time Lag Data

In the time-dependent case, the time lags are computed using the Fourier transforms evaluated at the surface of the cloud, after an impulsive localized transient injects seed photons with a specified spectrum at a specific radius. This represents a sudden, low-luminosity flash of radiation that subsequently scatters and Comptonizes throughout the cloud before the final signal escapes to the observer. In Appendix C, we present a proof showing that the time lags are the same as computed in either the source frame or observer's frame for a non-rotating cloud as is considered in this chapter. The Fourier-transformed signal emanating from the surface of the cloud can be transformed into the observer's frame to compute the time lags. When this is done one finds that there is no energy-dependent phase that is introduced through this transformation. Therefore, for simplicity, we compute the time lags in the source frame.

The theoretical prediction for the time lag observed between hard channel energy $\epsilon_{\rm hard}$ and soft channel energy $\epsilon_{\rm soft}$ at Fourier frequency ν_f is computed using the van der Klis et al. (1987) formula (cf. Equation (2.4)),

$$\delta t = \frac{\arg[S^*(x_{\rm soft}, \tilde{\omega}) H(x_{\rm hard}, \tilde{\omega})]}{2\pi\nu_f} \ , \tag{2.144}$$

where the dimensionless energies $x_{\rm soft}$ and $x_{\rm hard}$ are defined by

$$x_{\rm soft} \equiv \frac{\epsilon_{\rm soft}}{kT_e} \ , \qquad x_{\rm hard} \equiv \frac{\epsilon_{\rm hard}}{kT_e} \ . \tag{2.145}$$

The Fourier transforms of the soft and hard channel time series are computed using

$$S(x_{\rm soft}, \tilde{\omega}) = F(x_{\rm soft}, \tilde{\omega}) \ , \qquad H(x_{\rm hard}, \tilde{\omega}) = F(x_{\rm hard}, \tilde{\omega}) \ , \tag{2.146}$$

where F represents the Fourier transform radiated at the surface of the coronal cloud, at radius $r = R$ ($z = 1$). We assume that the observed time lags are the result of the time-dependent Comptonization of seed photons injected with either a monochromatic or bremsstrahlung initial energy distribution. Our results for the homogeneous and inhomogeneous Fourier transforms in the case of monochromatic photon injection are given by Equations (2.83) and (2.123), respectively, and our results for the homogeneous and inhomogeneous Fourier transforms in the case of bremsstrahlung injection are both covered by Equation (2.129). In the case of bremsstrahlung injection, we must also impose a low-energy self-absorption cutoff at energy $\epsilon = \epsilon_{\rm abs}$ in order to avoid producing an infinite number of seed photons.

All of our analytical formulas for the Fourier transform are expressed in terms of the dimensionless Fourier frequency, $\tilde{\omega}$, which is related to the dimensional Fourier frequency, ν_f, measured in Hz, via (see Equation (2.37))

$$\tilde{\omega} = 2\pi\nu_f t_* \ , \tag{2.147}$$

where the scattering time, $t_* = \ell_*/c$, is equal to the mean-free time at the outer edge of the cloud. The value of t_* is related to the cloud radius R and the value of η via (see Equation (2.22))

$$t_* = \frac{\ell_*}{c} = \frac{R}{\eta\, c} \ . \tag{2.148}$$

Once the values for the temperature parameter Θ, the scattering parameter η, and the inner radius $z_{\rm in}$ have been tied down via comparison of the observed time-averaged spectrum with the theoretical steady-state spectrum for a given source, the next step is to vary the values of the cloud radius, R, and the bremsstrahlung self-absorption energy, $\epsilon_{\rm abs}$, until we achieve reasonable qualitative agreement between the theoretical time lags and the observed time lags. This allows us to translate between the dimensionless Fourier frequency $\tilde{\omega}$ and the dimensional frequency ν_f using Equation (2.147), with the scattering time t_* computed using Equation (2.148). We consider several different scenarios for the calculation of the X-ray time lags below and compare the results with the observational data for Cyg X-1 and

GX 339-04.

Monochromatic Injection in Inhomogeneous Corona

When the injected spectrum is monochromatic, or nearly so, and the injection takes place in a homogeneous cloud, all of the authors who have examined the problem agree that the resulting time lags are independent of Fourier frequency, in contradiction to the observations (e.g. Miyamoto 1988, HKC, KB). Hence it is interesting to explore the consequences of altering the cloud configuration in our model to treat monochromatic seed photon injection in an *inhomogeneous* corona, with electron number density distribution $n_e(r) \propto r^{-1}$, which was also considered by HKC. Since the injected seed photons are monochromatic, with energy $\epsilon_0 = 0.1\,\mathrm{keV}$, we must use the Fourier transform Green's function, F_{G}, to compute the time lags by combining Equations (2.123), (2.144), and (2.146). The time lags resulting from monochromatic injection in an inhomogeneous cloud are plotted as a function of the Fourier frequency ν_f and compared with the Cyg X-1 data from Nowak et al. (1999) in Figure 2.5 for both large and small cloud radii. The channel energy values used are $\epsilon_{\mathrm{soft}} = 2\,\mathrm{keV}$ and $\epsilon_{\mathrm{hard}} = 11\,\mathrm{keV}$, which correspond to the channel-center energies used in the analysis of the observational data. It is clear that the model results do not fit the data very well for either value of the cloud radius. Note that the shape of the time lag curves exhibits the same trend as the data, but the magnitude is too large. This is a result of the long upscattering time required for the soft disk seed photons to reach the soft and hard channel energies.

HKC also computed time lags for monochromatic injection in an inhomogeneous cloud, but they were able to fit the observational data, in contrast to our results. However, in order to qualitatively match the observed time lags, HKC had to adopt an outer cloud radius of ~ 1 light-second ($3 \times 10^{10}\,\mathrm{cm}$), which is an order of magnitude larger than the cloud radii implied by our model. The discrepancy between the model results may be due to the fact that their cloud is optically thin, whereas our cloud is optically thick. The values for the optical depth derived here are consistent with those obtained during the low/hard state of Cyg X-1 by Malzac et al. (2008), Malzac (2012), Del Santo et al. (2013), and Frontera et al. (2001). Unfortunately, we can't use our model to explore the region of parameter space studied by HKC because the corona must be optically thick in order to justify the diffusion approximation employed in our approach.

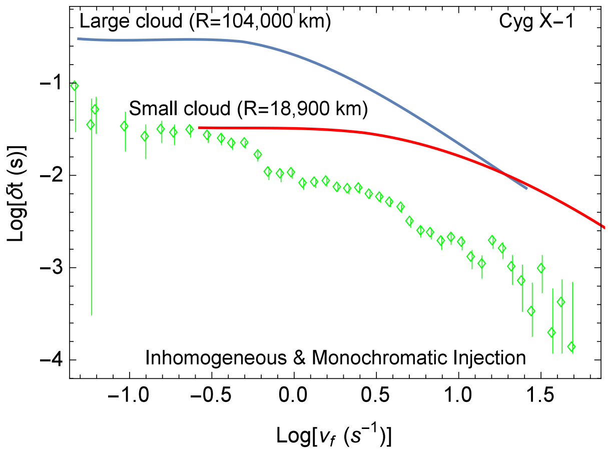

Figure 2.5: Theoretical time lag profiles resulting from monochromatic injection in an inhomogeneous cloud, with electron number density profile $n_e(r) \propto r^{-1}$, compared with the Cyg X-1 time lag data from Nowak et al. (1999). The time lags are computed by combining Equations (2.123), (2.144), and (2.146), and the channel energies used in the theoretical calculations are $\epsilon_{\rm soft} = 2\,{\rm keV}$ and $\epsilon_{\rm hard} = 11\,{\rm keV}$.

Variation of Seed Photon Distribution

It is apparent from Figure 2.5 that monochromatic injection into an inhomogeneous corona is unable to generate good agreement with the time lag data. Furthermore, it has been previously established by Miyamoto (1988), HKC, and KB that monochromatic injection into a homogeneous cloud also fails to agree with the data. Hence, it is interesting to use our new formalism to explore the alternative hypothesis of broadband (bremsstrahlung) seed photon injection, rather than monochromatic injection.

The bremsstrahlung-injection time lags are computed by combining Equations (2.129), (2.144), and (2.146), and the model parameters are varied until reasonable qualitative agreement with the observational data is achieved. We plot the theoretical bremsstrahlung-injection time lags as a function of the Fourier frequency ν_f in Figure 2.6, using both the homogeneous and inhomogeneous coronal cloud models. The results are compared with the observational data for Cyg X-1 and GX 339-04 taken from Nowak et al. (1999) and Cassatella et al. (2012), respectively. The corresponding physical parameters are listed in Table 1, and the channel energies used in the theoretical calculations are $\epsilon_{\rm soft} = 2\,{\rm keV}$ and $\epsilon_{\rm hard} = 11\,{\rm keV}$ for Cyg X-1, and $\epsilon_{\rm soft} = 2\,{\rm keV}$ and $\epsilon_{\rm hard} = 10\,{\rm keV}$ for GX 339-04, which correspond to the channel-center energies used in the observational calculations of the time lags. The low-energy self-absorption cutoff is set at $\epsilon_{\rm abs} = 1.6\,{\rm keV}$ for Cyg X-1 and at $\epsilon_{\rm abs} = 0.01\,{\rm keV}$ for GX 339-04. In the case of the homogeneous corona, the eigenvalues λ_n for the Fourier transform solution are the same real values obtained in the analysis of the time-averaged (quiescent) spectrum, which are plotted in the left-hand panel in Figure 2.3. In the case of the inhomogeneous corona, the eigenvalues λ_n are complex, and are plotted in Figure 2.7.

We find that in order to match the observational time lag data, the impulsive injection of the bremsstrahlung photons must occur near the outer edge of the cloud, with $z_0 \lesssim 1$. The transient that produces the soft seed photons is not treated in detail here, but we note that the outer edge of the corona is a region which the disk suddenly expands in the vertical direction, possibly leading to various types of plasma instabilities. In particular, the abrupt change in magnetic topology may generate rapid reconnection events that can result in the injection of a significant population of soft seed photons via bremsstrahlung emission (e.g., Poutanen & Fabian 1999).

In contrast with the behavior of the monochromatic injection scenario studied by Miyamoto et al. (1988), the results depicted in Figure 2.6 show that in the case of broadband (bremsstrahlung) seed photon injection into either a homogeneous or inhomogeneous cloud, Comptonization can produce Fourier frequency-dependent time lags that agree with the observational data for both Cyg X-1 and GX 339-04. The diminishing time lags at high

Fourier frequency are explained as a natural results of the prompt escape of broadband seed photons, combined with the delayed escape of upscattered Comptonized photons over longer timescales.

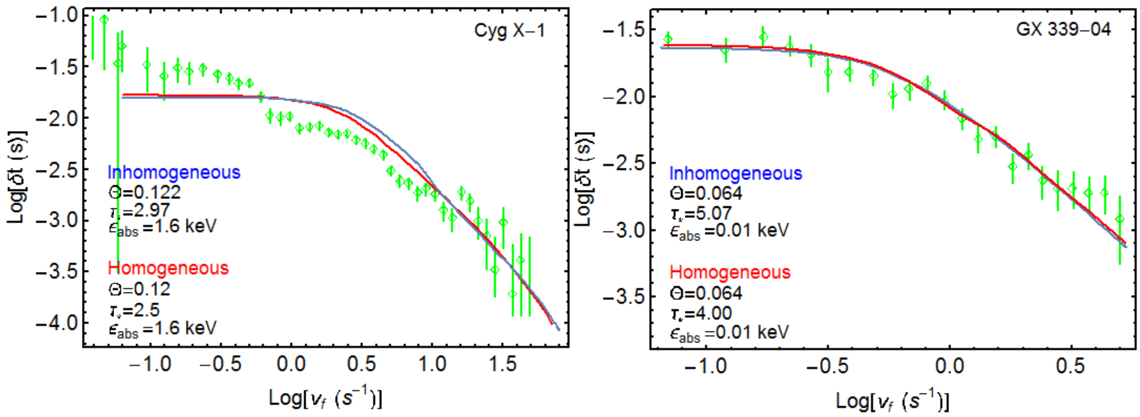

Figure 2.6: Theoretical time lag profiles for bremsstrahlung seed photon injection in a homogeneous corona (red) and an inhomogeneous corona (blue), compared with the data for Cyg X-1 (left panel) from Nowak et al. (1999), and the data for GX 339-04 (right panel) from Cassatella et al. (2012). See Section 6.2.3 and Figure 2.8 for a discussion of the convergence properties.

This indicates that the critical quantities for determining the shape of the time-lag profile are the overall optical thickness of the cloud and its temperature, which have nearly the same values in the homogeneous and inhomogeneous corona models. We therefore conclude that the actual configuration of the cloud (i.e. the detailed radial variation of the electron number density) is not well constrained by either the observations of the time lags or the observations of the time-averaged X-ray spectrum, and indeed, either cloud configuration works equally well, although there is a slight difference in the resulting cloud radius R, as indicated in Table 2.2.

Convergence of Time Lags

In our model, the time lags are computed based on analytical expressions for the Fourier transform of the emitted radiation spectrum. Since these expressions are stated in terms

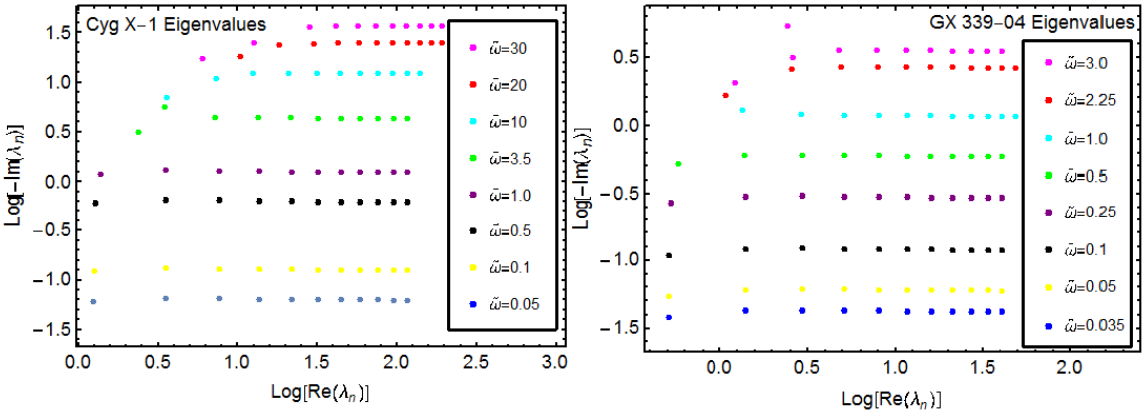

Figure 2.7: Complex eigenvalues, λ_n, for the Fourier transform in the inhomogeneous case. Left panel is for Cyg X-1 and right panel is for GX 339-04. Note that the imaginary part of λ_n is always negative, and therefore we change the sign before taking the log. The colors refer to the indicated values of the dimensionless Fourier frequency $\tilde{\omega}$, and the sequences running from left to right represent the values of λ_0 through λ_{10}.

of series expansions, it is important to examine the convergence of the results obtained for the time lags as one increases the truncation level of the series. Obviously, rapid smooth convergence is desirable.

In Figure 2.8, we present a convergence study of the theoretical time lags computed using the models for Cyg X-1 and GX 339-04, based on both the homogeneous and inhomogeneous cloud configurations. In each panel, the black curves represent the time lags evaluated using only the first term in the expansions, and the red and blue curves represent fully converged results, where no significant change will occur upon the addition of another term. The red and blue curves are the same as the final results for the time lags plotted in Figure 2.6. The time lags generally require about 20 terms to fully converge, whereas the expansions for the time-averaged spectra converge immediately (see Figures 2.1 and 2.2).

2.6 Discussion and Conclusion

We have obtained the exact analytical solution for the problem of time-dependent thermal Comptonization in a spherical scattering corona, based on two different electron density

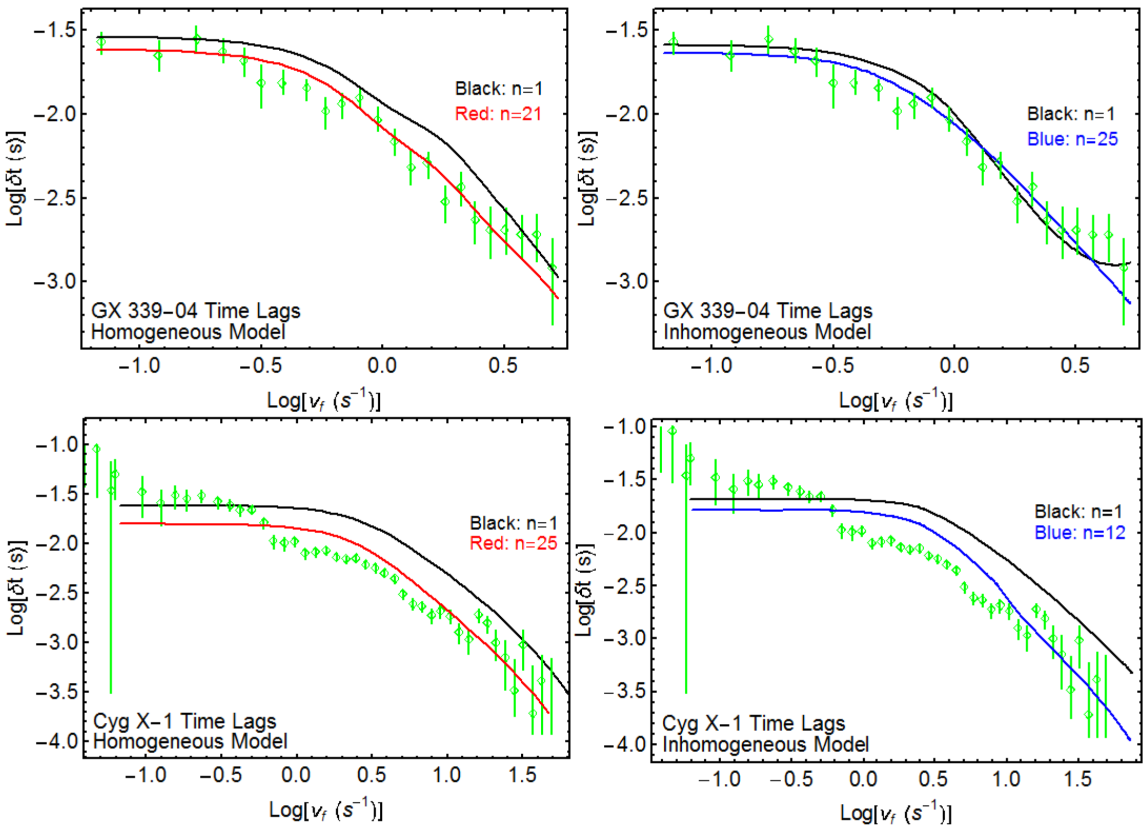

Figure 2.8: Convergence study of the theoretical time lags for Cyg X-1 and GX 339-04 computed using either the homogeneous or the inhomogeneous cloud model. The number of terms used in the series expansions for the Fourier transforms is indicated for each curve. The red and blue curves correspond to the final results plotted in Figure 2.6.

profiles. By working in the Fourier domain, we have obtained a closed-form expression for the Green's function corresponding to the injection of monochromatic seed photons into a cloud at a single radius and time. The radiated Fourier transform, evaluated at the surface of the cloud, can be directly substituted into the time lag formula introduced by van der Klis et al. (1987) in order to compute the predicted dependence of the lags on the Fourier frequency for any selected X-ray channel energies. In our approach, the time-averaged X-ray spectrum and the time lags are both computed using the same set of physical parameters to describe the properties of the scattering cloud, and therefore our formalism represents an integrated model that fully describes the high-energy spectral and timing properties of the source.

2.6.1 Relation to Previous Work

The study presented by HKC is similar to ours, although their methodology and input assumptions are somewhat different. HKC focused exclusively on a single injection scenario, namely the injection of essentially monoenergetic, low-temperature blackbody seed photons at the center of the scattering cloud. Based on this injection spectrum, they concluded that the observed time lag behavior in Cyg X-1 could not be reproduced unless the electron number density profile was inhomogeneous, with $n_e(r) \propto r^{-1}$ for example. In this case, although the predicted time lags fit the observed dependence on the Fourier period, the resulting dimensions of the cloud are so large that the requisite heating is difficult to accomplish based on any of the standard dissipation models.

Another notable difference between the work of HKC and the results developed here is that we have obtained a set of exact mathematical solutions, whereas HKC utilized a numerical Monte Carlo simulation method. This distinction is important, because by exploiting the exact solution for the Fourier transform of the Green's function, we are able to explore a much wider range of injection scenarios, in which we can vary both the location of the initial flash of seed photons, and its spectral distribution. Based on our analytical formalism, we are able to confirm the results of HKC regarding monochromatic injection, but we have also generalized those results by exploring the implications of varying the seed photon injection radius and spectrum. We find that the injection of *broadband* (bremsstrahlung) seed photons relatively close to the surface of a homogeneous or inhomogeneous cloud can fit the observed time lag profiles at least as well as the HKC model does, but with a cloud size an order of magnitude smaller. In Section 2.6.2 we discuss the physical reasons underlying the success of the bremsstrahlung injection scenario.

The treatment of electron scattering in our work differs from that utilized by HKC, since we have adopted the Thomson cross section, whereas HKC implemented the full expression for the Klein-Nishina cross section. In principle, utilization of the Klein-Nishina cross section would be expected to affect the hard time lags, due to the quantum reduction in the scattering probability at high energies. However, for the photon energy range of interest here, $\sim 0.1 - 10\,\mathrm{keV}$, combined with our maximum electron temperature, $kT_e = 62.4\,\mathrm{keV}$, not many photons are likely to sample the reduced cross section, which requires an incident photon energy exceeding $500\,\mathrm{keV}$ as seen in the rest frame of the electron. Hence it seems surprising that HKC observed a significant change in the normalization of their computed time lags when they adopted the Klein-Nishina cross section instead of the Thomson value. We suspect that this may be due to the somewhat higher electron temperature they used, $kT_e = 100\,\mathrm{keV}$.

To explore this question quantitatively, we can compute the fraction of electrons such that an incident photon of a given energy in the lab frame exceeds $500\,\mathrm{keV}$ in the electron's rest frame. The relevant thermal distribution function for the calculation is the relativistic Maxwell-Jüttner distribution, given by (e.g., Ter Haar & Wergeland 1971; Hua 1997)

$$f_{\mathrm{MJ}}(\gamma) \equiv \frac{\gamma\sqrt{\gamma^2 - 1}}{\Theta K_2(1/\Theta)} \exp\left(-\frac{\gamma}{\Theta}\right) \tag{2.149}$$

where $\Theta \equiv kT_e/(m_e c^2)$ and K_2 denotes the modified Bessel function of the second kind. The probability that a randomly-selected electron has a Lorentz factor in the range between γ and $\gamma + d\gamma$ is equal to $f_{\mathrm{MJ}}(\gamma)d\gamma$.

In order to compute an upper bound on the probability of generating a scattering in the Klein-Nishina regime, we shall focus on the most energetic possible collision scenario, which is a head-on collision between the electron and the photon. In this case, the incident photon energy in the electron's rest frame, E_0', is given by

$$E_0' = E_0 \left(\frac{1+\beta}{1-\beta}\right)^{1/2} \ , \qquad \beta^2 = 1 - \frac{1}{\gamma^2} \ , \tag{2.150}$$

where E_0 is the incident photon energy in the lab frame. By integrating the Maxwell-Jüttner distribution, we can compute the probability, P, that a randomly-selected electron has sufficient energy to create the required incident photon energy of at least 500 keV in the rest frame. The probability is given by

$$P = \int_{\gamma_0}^{\infty} f_{\rm MJ}(\gamma)\, d\gamma \ , \tag{2.151}$$

where the lower bound γ_0 is the root of the equation

$$500\,{\rm keV} = E_0 \left(2\gamma_0^2 - 1 + 2\gamma_0 \sqrt{\gamma_0^2 - 1} \right)^{1/2} \ . \tag{2.152}$$

Setting the incident photon energy $E_0 = 100\,$keV as an extreme example, we find that the lower bound is $\gamma_0 = 2.6$. Adopting the HKC temperature value, $kT_e = 100\,$keV, we obtain $\Theta = 0.2$, in which case the probability given by Equation (2.151) is $P = 3.1 \times 10^{-3}$. This probability may be large enough to explain the variation of the HKC time lag results observed when they switched between the Thomson cross section and the Klein-Nishina cross section, if some of the photons inverse-Compton scatter up to high enough energies to sample the Klein-Nishina regime, before returning to lower energies via Compton scattering. We can also compute the scattering probability P based on the maximum electron temperature that we have adopted in our applications, $kT_e = 62.4\,$keV, which yields $\Theta = 0.122$. In this case, one finds that the Maxwell-Jüttner integration gives $P = 2.6 \times 10^{-5}$, which is much smaller than the HKC result. Hence we conclude that utilization of the Klein-Nishina cross section would probably not make a significant difference in our applications. However, we can't reach any definitive conclusions about this question using the model developed here since it is based on the assumption of Thomson scattering in the electron's rest frame.

2.6.2 Formation of the Light Curves

The somewhat surprising difference between the time lag profiles produced when the injection spectrum has a monoenergetic shape versus a broadband shape can be explored by using the inverse Fourier transform to compute the time-dependent light curves for the hard and soft energy channels in the two cases. To accomplish this, we must make use of the inversion integral (cf. Equation (2.36))

$$f(x, z, p) = \frac{1}{2\pi} \int_{-\infty}^{\infty} e^{-i\tilde{\omega}p} F(x, z, \tilde{\omega})\, d\tilde{\omega} \ , \tag{2.153}$$

where F is the Fourier transform computed using either the monochromatic injection Green's function solution (Equation (2.83) for the homogeneous cloud, or Equation (2.123) for the inhomogeneous cloud), or the bremsstrahlung injection solution (the homogeneous and inhomogeneous cases are both computed using Equation (2.129)). Evaluation of Equation (2.153) requires numerical integration since the inversion integral cannot be performed analytically. We therefore focus on a few simple examples in order to illustrate the dependence of the light curves on the injection model.

In Figure 2.9, we plot the hard and soft channel light curves computed using Equation (2.153) for the case of a homogeneous cloud experiencing impulsive injection of either low-energy monochromatic seed photons or broadband (bremsstrahlung) seed photons. The parameters describing the monochromatic injection scenario are temperature $\Theta = 0.12$, injection location $z_0 = 1$, injection energy $\epsilon_0 = 0.1\,\mathrm{keV}$, soft channel energy $\epsilon_{\rm soft} = 2\,\mathrm{keV}$, and hard channel energy $\epsilon_{\rm hard} = 10\,\mathrm{keV}$. In the case of bremsstrahlung injection, we set $\Theta = 0.12$, $z_0 = 1$, $\epsilon_{\rm abs} = 0.1\,\mathrm{keV}$, $\epsilon_{\rm soft} = 2\,\mathrm{keV}$, and $\epsilon_{\rm soft} = 10\,\mathrm{keV}$. One can immediately identify the characteristic Fast Rise Exponential Decay (FRED) shape (e.g., Sunyaev & Titarchuk 1980) for each channel signal. As expected, the hard channel curve is delayed in time relative to the soft channel curve due to upscattering, but the detailed relationship between the two light curves depends qualitatively on whether the injection spectrum is monochromatic or

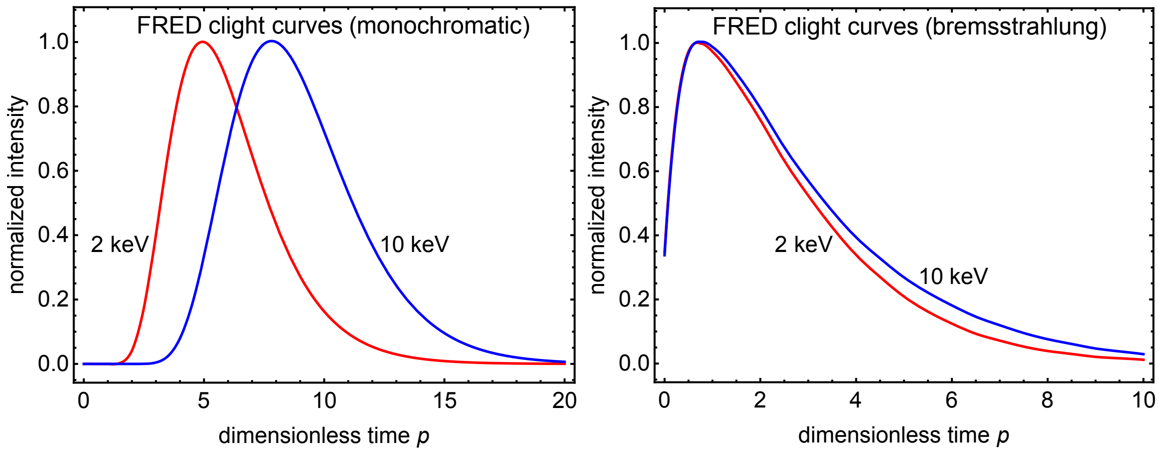

Figure 2.9: FRED curves from monochromatic and bremsstrahlung injection in a homogeneous cloud. In each case, the red curve represents the soft energy channel, set at 2 keV, and the blue curve denotes the hard channel, set at 10 keV. The normalized intensity in each channel shows the relative lag.

broadband.

One clearly observes that the two FRED curves resulting from monochromatic injection in a homogeneous cloud are of the same shape, and are simply shifted by a perfect delay with respect to one another on all timescales (see Figure 2.9). This yields a constant time lag across all Fourier frequencies (or periods), in agreement with the Miyamoto result that HKC and KB have confirmed. Our physical understanding of this behavior is as follows. Since all of the initial photons start with the same energy in the monochromatic case, the time lag is purely a result of Compton reverberation, where the upscattering timescale is proportional to the logarithm of the ratio of the hard to soft energies (Payne 1980). Based on this simple example, we conclude that monochromatic injection anywhere in a homogeneous cloud cannot produce Fourier frequency-dependent time lags, in contradiction with the observational data.

The relationship between the two FRED light curves plotted in Figure 2.9 for the case of bremsstrahlung injection is qualitatively different from the monochromatic example. In this case, the initial fast rise in both channels is coherent, meaning that the hard and soft channel signals track each other relatively closely. This results in a small time lag at high Fourier frequencies, because the fast rise portion of each curve represents the most rapid variation in the system. Physically, this part of the process corresponds to the prompt escape of "pristine" bremsstrahlung seed photons that are almost unaffected by scattering. Because bremsstrahlung is a broadband emission mechanism, both hard and soft photons exist in the initial distribution, and the prompt escape is therefore coherent across the energy channels. This is, of course, *not* true in the case of low-energy monochromatic injection, because in that scenario, photons require sufficient time to upscatter into both the soft and hard energy channels.

At longer timescales (smaller Fourier frequencies) in the bremsstrahlung case, the hard light curve approaches a delayed version of the soft light curve, reflecting the time it takes for the photons to Compton upscatter to the hard channel energy. This part of the process is similar to the monochromatic case, and indeed, we see that the time lags level off to a plateau at small Fourier frequencies, just as in the monochromatic example. To summarize, the overall behavior of the bremsstrahlung injection model matches the observational data much more closely then does the monochromatic injection scenario because of the combination of prompt escape (the fast rise part of the light curves) along with Compton reverberation (exponential decay) on longer timescales. This explains the origin of the qualitative difference in the behavior of the time lags at high Fourier frequencies exhibited in the monochromatic and bremsstrahlung injection scenarios, depicted in Figures 2.5 and 2.6, respectively.

2.6.3 Coronal Temperature

Both our model and that analyzed by HKC require the presence of hot electrons with temperature $T_e \sim 10^8\,\mathrm{K}$ at distances $r \sim 10^3\,GM/c^2$ from the black hole. This temperature distribution is consistent with a substantial number of studies that focus on energy transport in inefficient accretion flows, with accretion rates that are significantly sub-Eddington, as first established by Nayaran & Yi (1995) in the context of the original, self-similar Advection

Dominated Accretion Flow (ADAF) model. Similar results for the temperature distribution were later obtained using more complex numerical simulations by Oda et al. (2012), Rajesh & Mukhopadhyay (2010), Yuan et al. (2006), Mandal & Chakrabarti (2005), Liu et al. (2002), Różańska & Czerny (2000), and You et al. (2012). In these hot ADAF flows, the density in the outer region is so low that bremsstrahlung and inverse-Compton cooling are very inefficient. The lack of efficient cooling drives the electron temperature in the corona close to the virial value, out to distances of hundreds or thousands of gravitational radii from the black hole, in agreement with the temperature profiles assumed here.

In the study presented here, we have assumed that the electron scattering corona is isothermal in order to accomplish the separation of variables that is required to obtain analytical solutions to the radiation transport equation. The resulting analytical solutions allow us to determine the physical properties of the scattering corona in a given source by computing the time-averaged X-ray spectrum and the time-lag profile and comparing the theoretical results with the observational data. The assumption of an isothermal corona is roughly justified by studies indicating that the temperature does not vary by more than a factor of a few across the corona (e.g., You et al. 2012; Schnittman et al. 2013). Nonetheless, it is worth asking whether our results would be significantly modified in the presence of a coronal temperature gradient.

If the electron temperature varied across the corona, then in general one would expect the plasma to be hotter in the inner region, where the density is likely to be higher as well. In this scenario, the photons in the hot inner region would Compton upscatter faster than those in the cooler outer region, but they would spend more time (on average) scattering through the cloud before escaping due to the greater optical depth in the inner region. We estimate that these two effects would roughly offset each other, leaving the time lag profile close to the isothermal result derived here, if the temperature were set equal to the average value in the corona. Hence we predict that the results obtained for the time lags in the presence of a temperature gradient would be qualitatively similar to those obtained here using the isothermal assumption. Moreover, while the electrons may approach the virial temperature in the outer region, it is likely that in the inner region, the electron temperature is thermostatically controlled by Compton scattering (e.g., Sunyaev & Titarchuk 1980; Shapiro, Lightman & Eardley 1976). The combination of these two effects will tend to produce a relatively high, but uniform, electron temperature distribution, as we have assumed here.

2.6.4 Time Varying Coronal Parameters

If the transients responsible for producing the observed X-ray time lags in accreting black hole sources are driven by the deposition of a large amount of energy, then the properties of the corona (temperature, density) would be expected to respond. If this response occurs on time scales comparable to the diffusion time for photons to escape from the corona, then the resulting time lag profiles would be modified compared with the results obtained here, since we assume that the properties of the corona remain constant. Malzac & Jourdain (2000) have considered the possible variation of the coronal properties during X-ray flares using a non-linear Monte Carlo simulation to study the flare evolution as a function of time, along with the associated variation of the temperature and optical depth in the corona. They do not compute Fourier time lags, but they do present simulated light curves in the soft and hard energy channels. In their model, the flares are driven by a sudden increase in the disk's internal dissipation, which produces a large quantity of soft photons. The temperature and optical depth of the corona change self-consistently during the transient, and then return to the equilibrium state. They find that hard time lags are produced during the flare if the energy deposition is substantial.

The approach taken by Malzac & Jourdain (2000) is based on the pulse-avalanche model of Poutanen & Fabian (1999). The model does not explicitly include Compton upscattering as a contributor to the time-lag phenomenon, nor was the significance of the injection spectrum considered. The simulated light curves generated by Malzac & Jourdain (2000) sometimes display temporal dips, but the time dependence doesn't seem to resemble that observed during the transients in Cyg X-1. Since these authors do not compute Fourier time lags, it is difficult to directly compare their results with ours. However, we note that the transients under study here represent relatively small variations in the X-ray luminosity, which suggests that the energy deposition may not be large enough to significantly alter the large-scale properties of the scattering corona during the time it takes the photons to diffuse out of the cloud (Nowak et a. 1999; Cassatella et al. 2012). This supports our assumption that the temperature and density of the corona remain essentially constant during the formation of the observed time lags.

Chapter 3: Rotating Homogeneous Corona Model

3.1 Model Set-up

In the preceding chapter, we presented an integrated model for the production of X-ray time lags in a spherical hot accretion corona around a black hole. The model assumed an isothermal spherical corona which is irrotational. The static cloud model was able to reproduce the observed quiescent X-ray spectrum as well as the Fourier frequency dependent time lags. Additionally, the electron number density as a function of radius was studied in both the homogeneous and inhomogeneous models. These models were applied to observational data for two accreting sources (Cyg X-1 and GX 339).

In this chapter, we wish to study the effects of uniform rotation of the corona, but restrict our attention to the homogeneous model. This study will be applied to Cyg X-1 without loss of generality since we have seen that the resulting time lags are the same in each of the static homogeneous and static inhomogeneous clouds. The simpler homogeneous model will provide a clear framework within which to test any effects that a rotating cloud may have on the resulting time lags. In Appendix C, we show that for a static (irrotational) cloud, the time lags can be computed in any reference frame. However, in this chapter we find that the time lags must be computed in the cloud frame.

We define the geometry of the system in the figure below. The spherical cloud is set to rotate at a constant rate given by Ω_0. The vertical axis is set to be coincident with the rotation axis. We place the observer at some distance D from the black hole and in the equatorial plane of the accreting system. The inclination angle is defined as the angle between the rotation axis and the line of sight to the observer which in this case is set at $\pi/2$ radians and is given by Ψ. The angular velocity at a point on the surface of the cloud will be a function of latitude, given by the polar angle θ which is measured from the north

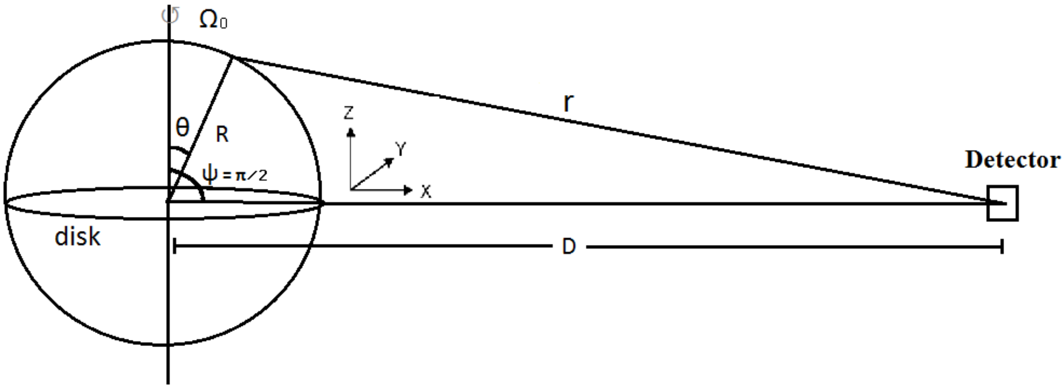

Figure 3.1: Diagram where the azimuthal angle ϕ is not able to be shown. The angle Ψ is the angle between the polar axis and the line of sight. In this example, $\Psi = \pi/2$.

pole. In the frame of the observer radiation emanating from the surface of the cloud will be Doppler shifted either blue or red depending on which part of the surface it came from. The radial Doppler shift will have a magnitude that depends on both θ and ϕ. Maximual blue shifting will be seen at the coordinates $(\theta, \phi) = (\pi/2, -\pi/2)$ if we take the plane of the page to be the $x - z$ plane as shown in the figure.

The distance between any point on the cloud surface and the observer is given by r as shown in the figure. We can write this in terms of the radius of the cloud, R, distance from the observer to the black hole, D, and the spherical angle coordinates, (θ, ϕ), as

$$r = \sqrt{R^2 + D^2 - 2DR\left(\cos\psi\cos\theta + \sin\psi\sin\theta\cos\phi\right)}\ . \tag{3.1}$$

This can be simplified by setting $\Psi = \pi/2$ giving

$$r = \sqrt{R^2 + D^2 - 2DR\sin\theta\cos\phi}\ . \tag{3.2}$$

In order to perform transformations between frames of reference, we first present a diagram showing the relative layout between the possible frames.

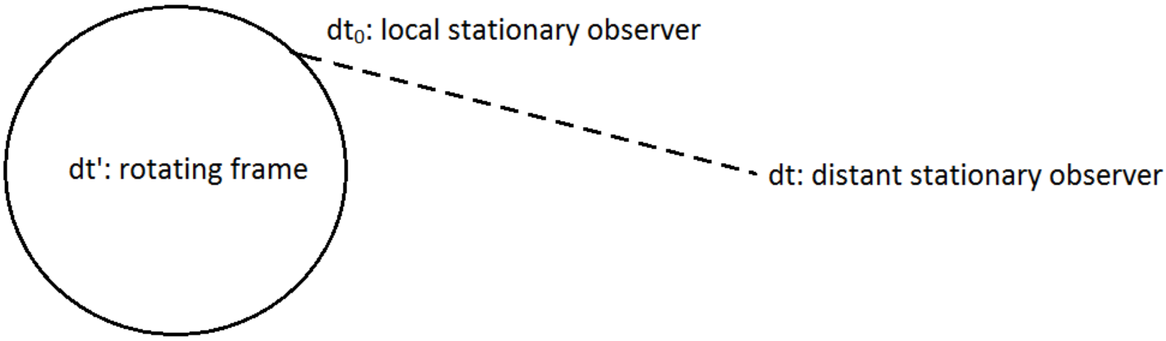

Figure 3.2: The local and distant observers have synchronized clocks and so only a propagation delay transforms between those frames. However, the moving frame of the source will have a Lorentz trasformation to go into either of the other two frames.

The two stationary observers are situation nearby and far from the rotating frame. Their clocks tick at the same rate, but are separated in time by the propagation delay, r/c. The differential time relationship between these two frames is given by

$$dt = dt_0 \tag{3.3}$$

Integrating this gives

$$t = t_0 + \frac{r}{c} \tag{3.4}$$

The transformation from the rotating frame to the local stationary observer is only a Lorentz transformation which is expressed as

$$dt' = \frac{dt_0}{\gamma} \rightarrow \gamma t' = t_0 \ , \tag{3.5}$$

where the final expression results from integration and γ is the Lorentz factor and is given by

$$\gamma = \frac{1}{\sqrt{1 - \left(\frac{R\Omega_0 \sin\theta}{c}\right)^2}} \ . \tag{3.6}$$

We can substitute Equation (3.5) into Equation (3.4) which results in

$$t = \gamma t' + \frac{r}{c} \ . \tag{3.7}$$

The energy transforms according to

$$\epsilon' = \epsilon \sqrt{\frac{c - R\Omega_0 \sin\theta \sin\phi}{c + R\Omega_0 \sin\theta \sin\phi}} \ , \tag{3.8}$$

and we note a Lorentz invariant in terms of the intensity in either frame as

$$\frac{I'}{\epsilon'^3} = \frac{I}{\epsilon^3} \ , \tag{3.9}$$

where I' is the intensity in the source frame and is related to the occupation number, f, via

$$I' = \frac{\epsilon'^3 c f}{4\pi} \ . \tag{3.10}$$

We can write the flux in terms of the intensity from Rybicki & Lightman, however, for an observer located at infinity, there will be a reduction in apparent flux from the differential solid angle $d\Omega$. We have in the source frame

$$g = \int I d\Omega = \int I \frac{dA_{\text{band}}}{D^2} \ , \tag{3.11}$$

where

$$dA_{\text{band}} = R^2 \sin\theta d\theta d\phi \ . \tag{3.12}$$

The differential area given in Equation (3.12) is exact, provided it is computed in the source frame. Additional observational effects are introduced when viewing the emitting band from an arbitrary angle. To get the flux in the direction of the observer subtended by differential solid angle $d\Omega$ we take the dot product of the radial unit vector, $(\hat{r})$, in the source frame and the direction to the observer $(\hat{x})$. From standard spherical coordinates we have the following modified solid angle,

$$d\Omega\ (\hat{r}\cdot\hat{x}) = \frac{dA_{\rm band}}{D^2}\sin\theta\cos\phi\ . \tag{3.13}$$

To obtain the observed flux from the differential flux, we must integrate over this modified solid angle in order to include the effects of apparent reduced differential area at the edges of the spherical cloud according to the observer. By substituting Equations (3.9), (3.10), (3.12), and (3.13) into Equation (3.11) we obtain

$$g_{\rm obs}(\epsilon,t) = \Big(\frac{R^2}{4\pi D^2}\Big)\int_{-\pi/2}^{\pi/2}\int_0^{\pi}\epsilon^3 c f_{\rm source}(\epsilon',t')\sin^2\theta\cos\phi d\theta d\phi\ . \tag{3.14}$$

The standard Fourier transform in the observer frame is defined as,

$$\mathscr{G}_{\rm obs}(\epsilon,\omega) \equiv \int_{-\infty}^{\infty} e^{i\omega t} g_{\rm obs}(\epsilon,t)dt\ . \tag{3.15}$$

By applying (3.15) to (3.14) yields,

$$\mathscr{G}_{\rm obs}(\epsilon,\omega) = \frac{R^2}{4\pi D^2}\int_0^{\pi}\int_{-\pi/2}^{\pi/2}\int_{-\infty}^{\infty}\sin^2\theta\cos\phi e^{i\omega t}\epsilon^3 c f_{\rm source}(\epsilon',t')dt d\phi d\theta\ . \tag{3.16}$$

Since frequency and time transform inversely we can write

$$\omega' t' = \omega t_0 = \omega(t - \frac{r}{c})\ , \tag{3.17}$$

then Equation (3.16) becomes

$$\mathscr{G}_{\rm obs}(\epsilon,\omega) = \frac{R^2\epsilon^3 c}{4\pi D^2}\int_0^{\pi}\int_{-\pi/2}^{\pi/2}\int_{-\infty}^{\infty} e^{i\omega r/c}\sin^2\theta\cos\phi e^{i\omega' t'} f_{\rm source}(\epsilon',t')dtd\phi d\theta \ . \tag{3.18}$$

We substitute $dt = \gamma dt'$ which gives

$$\mathscr{G}_{\rm obs}(\epsilon,\omega) = \frac{R^2\epsilon^3 c}{4\pi D^2}\int_0^{\pi}\int_{-\pi/2}^{\pi/2}\gamma e^{i\omega r/c}\sin^2\theta\cos\phi d\phi d\theta\int_{-\infty}^{\infty} e^{i\omega' t'} f_{\rm source}(\epsilon',t')dt' \ . \tag{3.19}$$

The definition of the Fourier transform in the source frame can be substituted into Equation (3.19) which gives

$$\mathscr{G}_{\rm obs}(\epsilon,\omega) = \frac{R^2\epsilon^3 c}{4\pi D^2}\int_0^{\pi}\int_{-\pi/2}^{\pi/2}\gamma e^{i\omega r/c}\sin^2\theta\cos\phi\mathscr{F}_{\rm source}(\epsilon',\omega')d\phi d\theta \ , \tag{3.20}$$

and γ depends only on θ as seen in Equation (3.6) and ϵ' is given by Equation (3.9). The transformation of frequencies is given by

$$\omega' = \gamma\omega \ . \tag{3.21}$$

3.2 Application and Results

In this section we will apply the time lag theory to observations from Cyg X-1 as a test of the rotating homogeneous corona model. The quiescent X-ray spectra would also be tested here, but we have seen in the previous chapter that the spectra are trivial to reproduce and have been studied in the past by numerous groups who found that the slope of the quiescent spectrum is determined by the Compton y-parameter and so is insensitive to dynamic properties of the cloud. This chapter will focus on the time-dependent X-ray time lag phenomenon for the rotating cloud model.

In Chapter 2 we presented the homogeneous model with a static corona based off the time-dependent transport equation describing the spatial diffusion and inverse Comptonization of a population of injected seed photons. The transport equation was Fourier transformed and the resulting analytic solution was obtained in the Fourier domain. This Fourier transformed Green's function represented the resulting transformed signal emanating from the surface of the cloud after a transient process injected a monochromatic population of seed photons. The Green's function allows for a wide variety of injection scenarios. We found that a monochromatic injection spectrum anywhere in a homogeneous optically thick cloud cannot reproduce the observed time lags as a function of Fourier frequency.

Instead, a broadband injection paradigm was implemented to model a thermal bremsstrahlung flash due to a plasma instability in the ADAF. The benefit of the Green's function allows for a variety of injection scenarios such as the bremsstrahlung paradigm employed here. The Green's function can be convolved with a bremsstrahlung source term (see Appendix B) to produce the particular solution for bremsstrahlung injection. The notation used in the previous section describes the Fourier transformed flux in either of two reference frames, but without regard to the injection spectrum that produced it. Based off of the results in Chapter 2, namely the monochromatic injection paradigm being rejected, we can interpret the generalized transformed flux in each frame presented in the previous section as being due to the preferred bremsstrahlung injection paradigm. Specifically, $\mathscr{G}_{\rm obs}$ and $\mathscr{G}_{\rm source}$ represent the Fourier transformed flux in each reference frame (observer and source, respectively) due to a bremsstrahlung transient. Since the source-frame solutions have been derived analytically, we will simply substitute the source-frame Fourier transform, $F_{\rm brem}$, given by the first case seen in Equation (2.129), directly into Equation (3.20) we can compute the time lags for this rotating corona model using Equation (2.4). However, in the case of the static cloud the solution was frame-independent, we must be sure to substitute $F_{\rm brem}$ into the RHS of Equation (3.20) in order to compute the observed time lags.

3.2.1 Results

The time lags computed from the rotating cloud model depend on the rotation rate, Ω_0. The non-rotating homogeneous model will be recovered in the limit of vanishing rotation rate. In order to study the effects that rotation has on the resulting time lags, we set all model parameters equal to those used in the non-rotating homogeneous model. As we vary the rotation rate the resulting time lags show noticeable features that differ from the non-rotating cloud. For comparison purposes we plot the Cyg X-1 data along with each of the homogeneous models.

The Compton reverberation idea can be clearly seen in the long timescales (low frequency) portion of the time lag plots shown in Figure 3.3 where the theory curves are the same from the plateau and past the break frequency where the curve becomes a power-law. This suggests that the dynamical properties of the cloud are not directly dependent upon coronal rotation. The long time-scales are set by the upscattering time from the soft to hard channels and represent the Compton reverberation idea. The time lag spectrum has a break where it turns over from the plateau to a power-law with a roughly constant slope of about negative 1.27 which agrees with the trend in the observational data.

We treat the rotation rate as a free parameter since there is no way to directly or even indirectly measure coronal rotation rates. However, by varying the rotation rate as a model parameter we can study the effects on the resulting time lags for Cyg X-1 and GX 339. It is important to use the Keplerian angular velocity, $\Omega_{\rm Kep}$, as a starting point of this study. We assume that the corona rotates uniformly and compute the Keplerian velocity at the equator given mass estimates for the central mass and the radius of the cloud computed in each model. We apply this model only to the homogeneous corona, because we found that the time lags are the same in the homogeneous and inhomogeneous corona models.

Figure 3.3 shows a comparison of two models with the Cyg X-1 time lag data. The red dashed curve corresponds to the non-rotating homogeneou corona presented in Chapter 2 while the blue dashed curve represents the maximally rotating cloud where the angular velocity is set to the Keplerian velocity. The same convergence level was applied to each model and they agree exactly. There is no difference in the time lag at any Fourier frequency implying that a Keplerian rotation rate does not change the time lags. At the equator of a maximally rotating cloud, the linear velocity is $\beta_{\mathrm{eq}} = 0.022$ which is hardly relativistic. We list the equatorial β-factors for each source and each value of Ω_0 in Tables 3.1. Note that although the same rotation rates are used in each source, the cloud radii are different with that of GX 339 being slightly larger than Cyg X-1. The Lorentz transformations performed on the Fourier frequency and energy are not significantly altered from the rest frame values which leads to the same result as the non-rotating cloud.

Although it would be unphysical to simulate a super-Keplerian rotation rate, it is interesting to perform a parameter-space study of Ω_0 for values significantly above Ω_{Kep}. In order to see any deviations from the "standard" (i.e. baseline time lags seen in the non-rotating homogeneous model) we must set $\Omega_0 \gg \Omega_{\mathrm{Kep}}$. In this computational regime we do not provide a physical mechanism for the super-Keplerian rate since those results are not subsumed by the primary focus of this model. In Figure 3.4 we present four plots that show the modifications to the time lags as the rotation rate is steadily and significantly increased past the Keplerian rate.

The low Fourier frequency portion of the plot and up to intermediate values show excellent agreement between the rotating and non-rotating cloud models. This is interesting, because the Fourier frequency corresponds to long timescales in which the injected population of seed photons from a bremsstrahlung flash upscatter to the hard energy channel. This is the Compton reverberation idea and is set by the plateau feature on the plots where the time lags level off to a constant value below a certain Fourier frequency.

Deviations from the standard time lag profile for Cyg X-1 can be seen at high Fourier frequencies where the lags are increased relative to the non-rotating model. As the rotation frequency is increased, this feature becomes more pronounced. The effects of Lorentz boosting become important as the rotation rate increases beyond the Keplerian rate. The blue-shifted photons on the leading hemisphere increase the energy of any photon, but the amount of blue-shift is dependent on the location of the cloud surface. Maximum blue-shifting will occur on the equator for $\phi \approx -\pi/2$. Correspondingly, there will be maximum red-shifting on the opposite hemisphere (western hemisphere is red-shifted, eastern hemisphere is blue-shifted) at $\phi \approx \pi/2$. The red and blue-shifts decrease as one looks closer to the poles where the linear velocity diminishes. In Figure 3.4 we plot the super-Keplerian

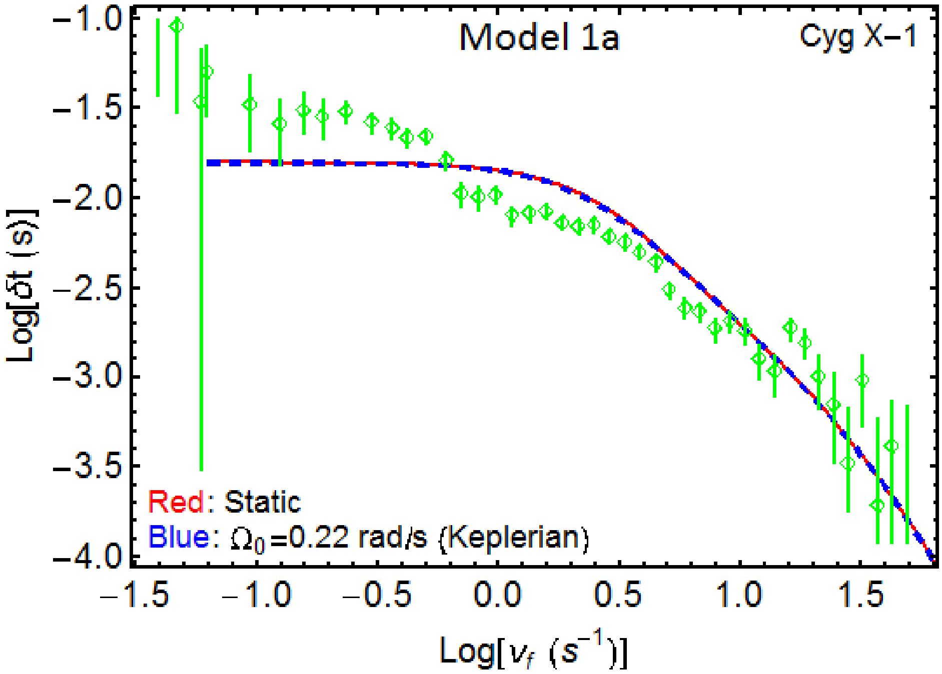

Figure 3.3: The spinning homogeneous model (blue) compared with the static homogeneous model (red) for Cyg X-1 time lag data from Nowak et al. (1999), for the Keplerian angular velocity $\Omega_0 = \Omega_{\rm Kep}$.

rotation time lags in order to study the effects of rotation on the resulting time lags for Cyg X-1. Next, we will apply this model to GX 339.

Rotating Cloud Model Applied to GX 339

The time lag data for GX 339 seems to have better data characterized by a clear trend and small error bars at high and low Fourier frequencies. It is interesting to plot theoretical time

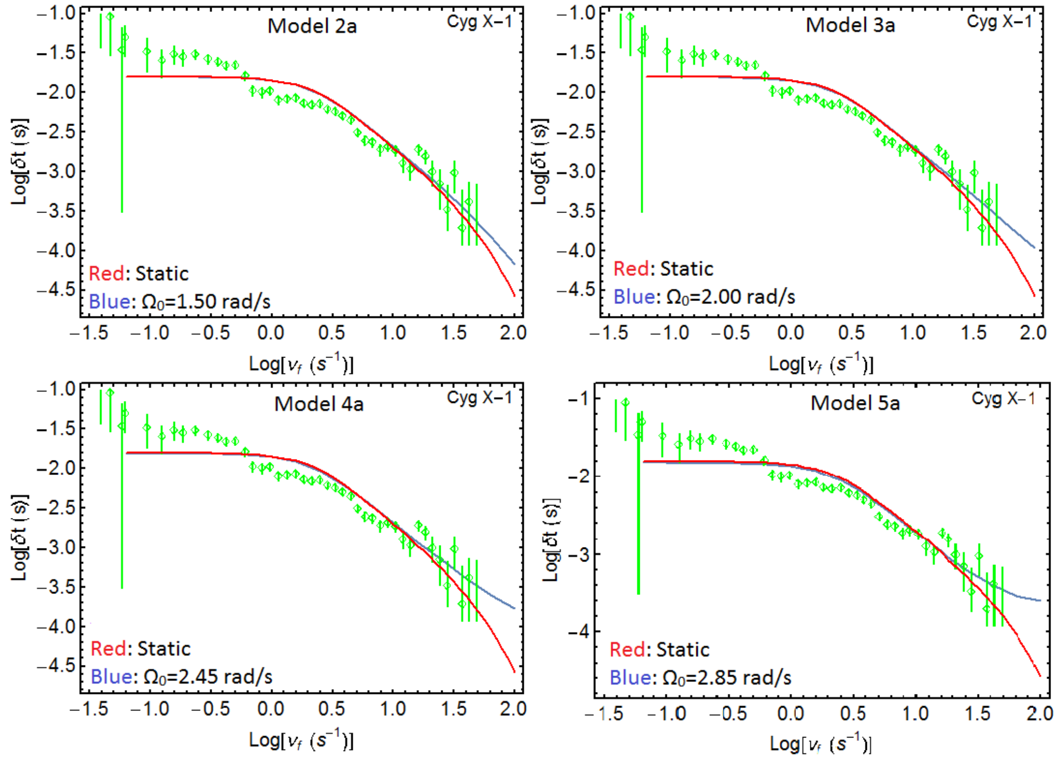

Figure 3.4: The spinning homogeneous model (blue) compared with the static homogeneous model (red) for Cyg X-1 time lag data from Nowak et al. (1999), for various values of angular velocity Ω_0.

lag curves using the rotating cloud model and compare it against the observational data. In Figure 3.5 we plot the time lags for a corona rotating at the Keplerian rate. The value for the Keplerian angular velocity can be found in Table 3.1 along with various super-Keplerian rotation rates. The super-Keplerian rotation rate scenarios are plotted in Figure 3.6 for GX 339 and one can see the different behavior than was seen in the case of Cyg X-1.

Using the homogeneous model parameters found in Chapter 2 (see Tables 2.1 and 2.2), we apply the rotating cloud model to GX 339. The Keplerian rotation rate is plotted first and then a panel of super-Keplerian rotation modes are also shown and compared with the observational data for this source as well as the non-rotating cloud case. As we saw with Cyg X-1, the Keplerian rotation rate is slow and there is no significant boosting between frames

Table 3.1: Input Model Parameters: Cyg X-1 and GX 339

Model #	Source	Θ	R (cm)	z_0	$\beta_{\rm eq}$	$\Omega_{\rm Kep}$ (rad/s)	Ω_0 (rad/s)
1a	Cyg X-1	0.120	3.00×10^9	1.00	0.022	0.22	0.22
2a	Cyg X-1	0.120	3.00×10^9	1.00	0.150	0.22	1.50
3a	Cyg X-1	0.120	3.00×10^9	1.00	0.200	0.22	2.00
4a	Cyg X-1	0.120	3.00×10^9	1.00	0.245	0.22	2.45
5a	Cyg X-1	0.120	3.00×10^9	1.00	0.285	0.22	2.85
1b	GX 339	0.064	4.56×10^9	0.78	0.018	0.12	0.12
2b	GX 339	0.064	4.56×10^9	0.78	0.228	0.12	1.50
3b	GX 339	0.064	4.56×10^9	0.78	0.304	0.12	2.00
4b	GX 339	0.064	4.56×10^9	0.78	0.372	0.12	2.45
5b	GX 339	0.064	4.56×10^9	0.78	0.433	0.12	2.85

and so the time lags agree exactly with the non-rotating model. The Keplerian rotation is the only case that is physically valid. However, we also wish to study the resulting theoretical time lags in the super-Keplerian rotation regime without regard to the mechanism that would produce such extraordinarily high rotation speeds. In Figure 3.6 we plot the a series time lags with ever increasing super-Keplerian rotation rates. What is interesting in the this case for GX 339 is there is a noticeable qualitative difference than is seen in the Cyg X-1 study for super-Keplerian rotation. There was an excess of time lag above the non-rotating cloud at the highest Fourier frequencies. However, for GX 339 we notice that the time lags for the rapidly rotating cloud fall below the time lag curve corresponding to the non-rotating cloud. What is more is that the divergence between the two models in Figure 3.6 occurs at lower Fourier frequencies and have the same power-law slow as the non-rotating time lag curve (they are parallel).

The time lags are identical to those of the non-rotating case if the cloud is rotating at or below the Keplerian velocity (sub-Keplerian rotation rates are not presented) for either source. This must imply that the radiated flux at the surface of the cloud is not significantly boosted to higher or lower energies and so no deviation from the static case are discernible. The Comptonized signal is essentially unaffected by the Keplerian rotation rate of the cloud

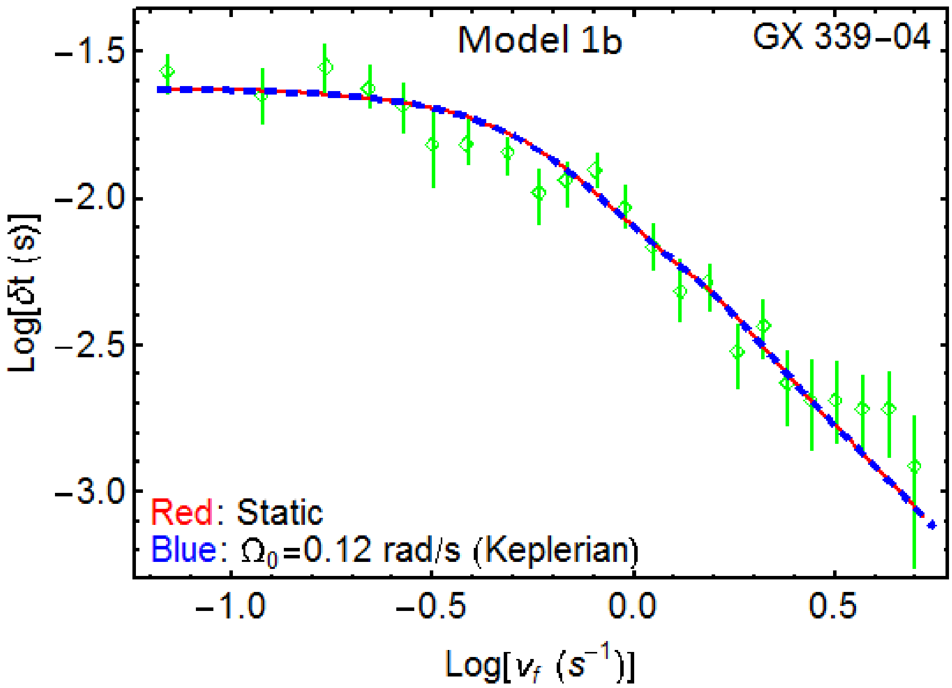

Figure 3.5: The spinning homogeneous model (blue) compared with the static homogeneous model (red) for GX 339 time lag data from Nowak et al. (1999), for the Keplerian angular velocity $\Omega_0 = \Omega_{\rm Kep}$.

in each source and hence we recover the results from the static cloud.

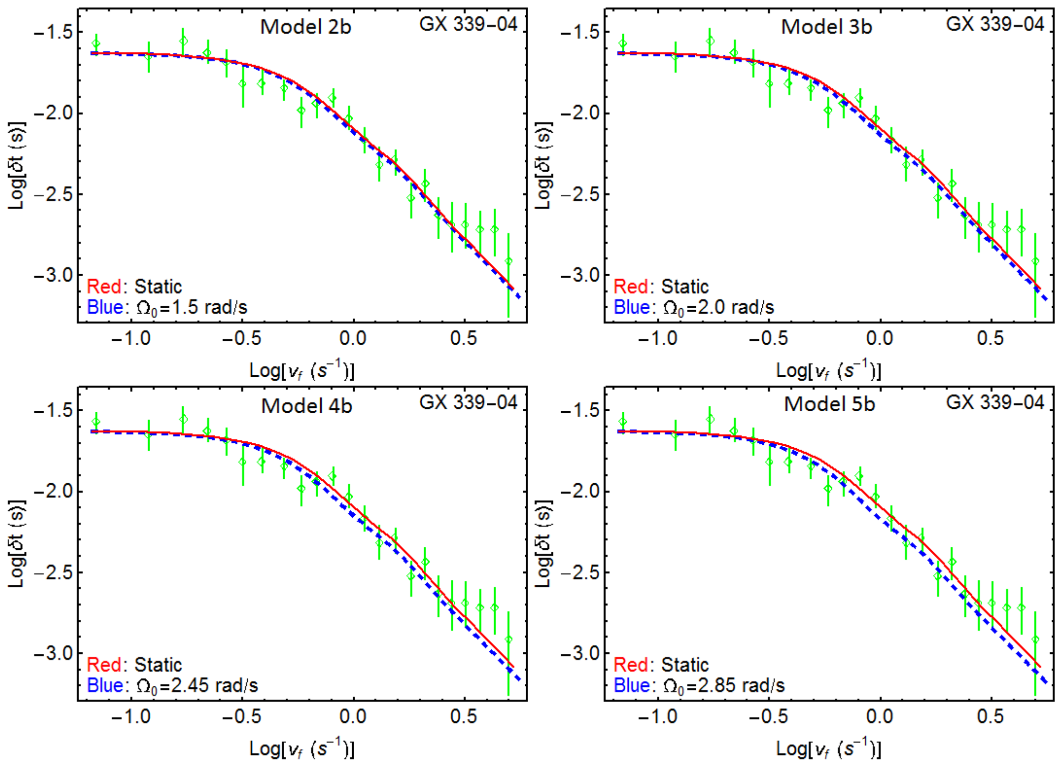

Figure 3.6: The spinning homogeneous model (blue) compared with the static homogeneous model (red) for GX 339 time lag data from Nowak et al. (1999), for various values of angular velocity Ω_0.

Chapter 4: Crab Nebula Gamma-Ray Flares

From 2010 September through 2013 March, the Crab nebula displayed a remarkable series of six short-duration flares in the $\sim 100 - 500\,\mathrm{GeV}$ energy range. During the peak of the "super flare" of 2011 April, the Crab nebula was the brightest γ-ray source in the sky, with an observed flux exceeding that of the Vela pulsar or any of the γ-ray emitting active galaxies. The spectral shape of the transient emission is a broad hump in the energy range from 0.1-1 GeV, and the flare showed a rapid increase over a few days, from April 13-15, with a total duration of about 9 days (Buehler at al. 2012). At its brightest, the flare luminosity reached about 30 times the average value, corresponding to $\sim 1\,\%$ of the spin-down luminosity of the rotating neutron star. The second-brightest flare was observed in 2013 March (Buehler & Blandford 2014), and the statistics were similar to the 2011 flare, except that in this case, some evidence was found for sub-day variability (Striani et al. 2013). These observation of γ-rays from the Crab nebula with energies at least an order of magnitude above the radiation reaction limit, $\sim 200\,\mathrm{MeV}$, presents serious challenges to the standard astrophysical particle acceleration mechanisms.

The observation of transient GeV emission from the Crab nebula implies the presence of intense particle acceleration in the vicinity of the pulsar wind termination shock, which is a standing shock generated where the wind encounters dense material in the outer region of the nebula (Montani & Bernadini 2014). The pulsar wind termination shock is located at radius $r \sim 10^{17}\,\mathrm{cm}$, which is about an order of magnitude less than the size of the nebula itself (Rees & Gunn 1974). On the upstream side of the termination shock, the wind is ultrarelativistic, with bulk Lorentz factor $\Gamma_u \gtrsim 10^3 - 10^6$ (Lyubarsky 2003; Aharonian et al. 2004). Conversely, the flow exiting the shock on the downstream side is only mildly relativistic, with speed $c/3$ and bulk Lorentz factor $\Gamma_d \sim 1.1$ (Achterberg et al. 2001). The very large value of the upstream Lorentz factor Γ_u implies that relativistic shock acceleration may play an important role in the formation of the high-energy γ-rays observed by *Fermi*-LAT and *AGILE* (Buehler & Blandford 2014). Diffusive acceleration of electrons at a standing shock, whether relativistic or non-relativistic, is mediated by MHD waves, and therefore the maximum acceleration rate is limited to the Bohm rate (Lemoine & Waxman 2009). Relativistic shocks can be less efficient accelerators than non-relativistic shocks, once the increase in the scattering time in the relativistic case is included (Sironi et al. 2015).

Hence, one finds that the particle acceleration rate is limited to the Bohm rate whether the acceleration occurs via the first-order Fermi process operating at a shock, or via the second-order Fermi process due to stochastic wave-particles interactions. In either case, the maximum particle energy that can be achieved is ultimately limited by synchrotron losses, and the value of the maximum energy is obtained by equating the Bohm acceleration rate with the synchrotron loss rate. This yields the radiation-reaction, or "synchrotron burnoff," limit for the electron energy (see Section 4.1). In the end, the limited efficiency of shock acceleration and stochastic wave-particle acceleration leads to the conclusion that these processes are unable to explain the observed high-energy transient emission from the Crab nebula, even when one includes the mild Doppler boost that occurs on the downstream side of the shock (e.g., Komissarov & Lyutikov 2011).

A number of authors have attempted to explain the observed GeV transients from the Crab nebula by circumventing the synchrotron burnoff limit using a variety of physical mechanisms. This limit can be violated (1) for emission regions with bulk relativistic motion, (2) by acceleration in a low magnetic-field region and radiation in a high-field region, and (3) if an accelerating electric field is present, as produced, for example, by magnetic reconnection. We consider possibility (3) by examining the particle diffusion equation with an accelerating electric field, stochastic and shock acceleration, shock-regulated escape (SRE), and escape from the nebula via Bohm diffusion. An exact solution is obtained for the resulting electron distribution.

Significant progress has been made on this problem using particle-in-cell (PIC) simulations (Cerutti et al. 2013a, 2014), but a complete understanding of the particle acceleration phenomenon occurring in the Crab nebula pulsar wind is still lacking. In particular, it is not clear whether the level of magnetic suppression required in the reconnection models can be achieved. We review some of the key observational diagnostics below and discuss the implications for the theoretical models.

4.1 Flare Energetics

The characteristic peak synchrotron energy emitted by an isotropic distribution of relativistic electrons with Lorentz factor γ spiraling in a magnetic field with strength B is (e.g., Rybicki & Lightman 1979)

$$\epsilon_{\rm pk}(\gamma) = \xi \frac{B}{B_{\rm crit}} \gamma^2 m_e c^2 = 231.5 \text{ MeV } \xi \left(\frac{\gamma}{10^{10}}\right)^2 \left(\frac{B}{200\mu\text{G}}\right) , \tag{4.1}$$

where m_e is the electron mass, c is the speed of light, the constant $\xi \sim 1$, and the critical magnetic field is defined by

$$B_{\rm crit} \equiv \frac{2\pi m_e^2 c^3}{eh} = 4.41 \times 10^{13} \text{ G} . \tag{4.2}$$

Observational estimates of the magnetic field strength in the Crab nebula are typically close to $B \sim 200$ μG (e.g., Aharonian et al. 2004). The generation of synchrotron emission with an energy of ~ 1 GeV by an isotropic electron distribution in the presence of such a field therefore requires a Lorentz factor $\gamma \sim 2 \times 10^{10}$.

The synchrotron lifetime of the relativistic electrons producing the flare can be estimated using

$$t_{\rm syn} = -\frac{\gamma}{<\dot{\gamma}>_{\rm syn}} , \tag{4.3}$$

where the synchrotron energy loss rate per electron, averaged over an isotropic distribution of pitch angles, is given by

$$<\dot{\gamma}>_{\rm syn}\, m_e c^2 = -\frac{4}{3}\gamma^2 \sigma_{\rm T} c \frac{B^2}{8\pi} \ . \tag{4.4}$$

Combining Equations (4.3) and (4.4) yields for the synchrotron lifetime

$$t_{\rm syn} = \frac{6\pi m_e c^2}{\sigma_{\rm T} c B^2 \gamma} = 22.4 \ {\rm days} \ \left(\frac{B}{200\mu{\rm G}}\right)^{-2} \left(\frac{\gamma}{10^{10}}\right)^{-1} \ . \tag{4.5}$$

We can also express the synchrotron lifetime as a function of the peak flare photon energy, $\epsilon_{\rm pk}$, by using Equation (4.1) to eliminate the Lorentz factor γ in Equation (4.5), obtaining

$$t_{\rm syn} = 10.8 \ {\rm days} \ \left(\frac{B}{200\mu{\rm G}}\right)^{-3/2} \left(\frac{\epsilon_{\rm pk}}{\rm GeV}\right)^{-1/2} \xi^{1/2} \ . \tag{4.6}$$

For a peak photon energy $\epsilon_{\rm pk} \sim 1\,{\rm GeV}$, and field strength $B \sim 200\,\mu{\rm G}$, we obtain roughly the observed flare duration. This fact has lent support to the interpretation that the observed γ-ray flares are the result of synchrotron emission (e.g., Abdo et al. 2011). However, the radiation reaction (synchrotron burnoff) limit places severe constraints on the particle acceleration mechanism required to power the observed emission, as discussed below. Variability on shorter timescales ($\sim 1\,$day) may have also been observed (Buehler et al. 2012; Mayer et al. 2013; Striani et al. 2013), perhaps as a consequence of instabilities in the structure of the termination shock and the strength of the associated magnetic field.

4.1.1 Synchrotron Burnoff

The minimum timescale for the acceleration of relativistic electrons via energetic collisions with MHD waves is the Larmor timescale,

$$t_{\rm L} = \zeta \frac{r_{\rm L}}{c} = \zeta \frac{m_e c}{qB} \gamma \ , \tag{4.7}$$

where $r_{\rm L}$ is the Larmor radius, ζ is an order unity constant, and q denotes the magnitude of the electron charge. The synchrotron burnoff limit is obtained by equating the Larmor timescale with the synchrotron loss timescale, given by Equation (4.5), which yields an expression for the maximum Lorentz factor, $\gamma_{\rm MHD}$, that can be achieved via MHD wave acceleration in the presence of a magnetic field of strength B. The result obtained is

$$\gamma_{\rm MHD} = \sqrt{\frac{6\pi q}{B\,\zeta\,\sigma_{\rm T}}} = 8.25 \times 10^9 \left(\frac{B}{200\,\mu{\rm G}}\right) \zeta^{-1/2} \ . \tag{4.8}$$

We can substitute Equation (4.8) into Equation (4.1) to obtain the radiation reaction-limited peak synchrotron energy, given by

$$\epsilon_{\rm MHD} \equiv \epsilon_{\rm pk}(\gamma_{\rm MHD}) = \frac{6\pi\,\xi q\, m_e c^2}{B_{\rm crit}\zeta\,\sigma_{\rm T}} = 158 \ {\rm MeV} \ \xi \ \zeta^{-1} \ , \tag{4.9}$$

where $\xi \sim 1$ and $\zeta \gtrsim 1$. This is far below the highest energy observations which are in excess of 1 GeV. Hence, the synchrotron burnoff limit implies that particle acceleration via interaction with MHD waves is insufficient to explain the energetics of the observed Crab nebula γ-ray flares.

The observation of gamma rays with energies exceeding the radiation reaction limit given by Equation (4.9) has motivated speculation that the radiating electrons are accelerated electrostatically in a magnetic reconnection region where electric fields are induced (e.g., Buehler at al. 2012; Cerutti et al. 2012). However, numerical simulations based on electrostatic acceleration in a magnetic reconnection region require the presence of a $\sim 5\,\mathrm{mG}$ magnetic field and PeV electrons (Cerutti et al. 2012, 2013a, 2014) . This field strength is substantially higher than that indicated by the multi-wavelength observations of the quiescent spectrum, which suggest that the ambient field has strength $B \sim 200\,\mu\mathrm{G}$ (e.g., Aharonian et al. 2004; Meyer & Horns 2010). These studies focused on the comprehensive broad-band (from radio through hard γ-rays) spectrum to infer the average ambient magnetic field responsible for the observed synchrotron emission from the Crab nebula.

In this paper, we seek to determine whether a theoretical framework can be developed that accounts for all of the Crab nebula γ-ray flare spectra detected by *Fermi*-LAT, while adopting the lower, ambient magnetic field value, $B \sim 200\,\mu\mathrm{G}$. Our model is based on a one-zone electron transport equation that includes terms describing particle injection, stochastic acceleration, electrostatic acceleration, shock acceleration, radiative losses, and particle escape. The model should be interpreted as a spatial average over the acceleration and emission regions, which may either be co-located or separate regions. The transport equation is solved to obtain a closed-form expression for the energy distribution of the relativistic electrons, which is then used to compute the γ-ray spectrum produced via direct synchrotron emission.

The remainder of the paper is organized as follows. In Section 4.2, we provide an overview of the physical background and develop the specific terms to be employed in the electron transport equation. In Section 4.3 we obtain the exact solution for the electron Green's function, and we develop expressions for computing the corresponding synchrotron spectrum. In Section 4.4 we make a specific application to modeling the γ-ray emission observed from the Crab nebula, and in Sections 4.5 and 5.2 we review our main conclusions and discuss their astrophysical significance.

4.2 Particle Transport Formalism

Since the energy range of the GeV flares observed from the Crab nebula exceeds the synchrotron burnoff limit by at least an order of magnitude, a natural conclusion seems to be that the radiating electrons must be accelerated, at least in part, by a strong electrostatic effect produced by the electric field created in a region of magnetic reconnection on the downstream side of the pulsar wind termination shock. Although numerical simulations have been employed to model this phenomenon, they have not been entirely successful at explaining the shape of the observed γ-ray spectrum, and furthermore they tend to invoke a magnetic field strength that does not agree very well with the observational estimates for the Crab nebula (Cerutti et al. 2012, 2013a, 2014).

The synchrotron lifetime given by Equation (4.6) provides a rough estimate for the time it takes the electron distribution to reach equilibrium. The fact that the synchrotron timescale is comparable to the flare duration suggests that the particle distribution during the peak of the flare is close to equilibrium. In this case, we are justified in setting the time derivative in Equation (4.10) equal to zero, and solving the steady-state transport equation. Hence the steady-state particle distribution we will obtain is best interpreted as the electron distribution during the peak of the flare.

The uncertainties regarding the numerical simulations have motivated us to revisit the problem using an analytical approach based on a transport equation that includes terms describing electrostatic acceleration, stochastic acceleration, shock acceleration, synchrotron losses, and particle escape. Since synchrotron losses are included in the transport equation, the subsequent calculation of the γ-ray synchrotron spectrum is self-consistent. It is always preferable to describe the particle distribution, and the resulting radiation spectrum, using an analytical expression because it facilitates the study of a wide range of parameter values, and it also allows us to maintain complete control over the relative importance of the various physical processes. Conversely, complex numerical simulations can sometimes make it difficult to pinpoint the specific effect of each process, and they are usually not amenable to fitting observational data. Another advantage of closed-form analytical models it that they can often be evaluated in real-time, allowing one to perform quantitative fits to the observational data, and they are also useful for benchmarking more sophisticated numerical simulations.

4.2.1 Particle Distribution and Transport Equation

The spatial transport of the electrons in the environment surrounding the pulsar wind termination shock is governed by a combination of advection in the wind and spatial diffusion relative to the wind. In the Crab nebula, the particle acceleration and the production of the observed γ-rays may occur in separate geometrical regions (e.g., Cerutti et al. 2012), but it is not clear whether this is the case. Therefore, in the present paper, we will develop a one-zone spatial model, which represents an average over the acceleration and emission regions. In this approach, the spatial aspects of the problem are modeled using a simple escape-probability formalism, with escape timescale $t_{\rm esc}$. The energy dependence of $t_{\rm esc}$ depends on the nature of the mechanism transporting electrons out of the acceleration region. In our application, the dominant escape mechanism is expected to be a combination of shock-regulated escape on small scales, and Bohm diffusion on large scales, as discussed in Section 4.4.5. Based on these physical considerations, the transport equation we will utilize to model the evolution of the relativistic electron momentum distribution, f, in the pulsar wind nebula is given by (e.g., Becker et al. 2006; Park & Petrosian 1995)

$$\frac{\partial f}{\partial t} = -\frac{1}{p^2}\frac{\partial}{\partial p}\left\{p^2\left[-D(p)\frac{\partial f}{\partial p} + <\dot{p}>_{\rm gain}f + <\dot{p}>_{\rm loss}f\right]\right\} - \frac{f}{t_{\rm esc}(p)} + \dot{f}_{\rm source}(p) \ , \quad (4.10)$$

where p is the particle momentum, and the terms on the right-hand side represent stochastic (second-order) Fermi acceleration (i.e., momentum diffusion); systematic gains due to electrostatic acceleration and first-order Fermi acceleration at the shock; systematic losses due to synchrotron emission; particle escape; and particle injection, respectively. The distribution function f is related to the total number of electrons, N_e, via

$$N_e(t) = \int_0^\infty 4\pi p^2 f(p,t)\, dp \ . \tag{4.11}$$

4.2.2 Stochastic MHD Acceleration

The γ-rays emitted during the *Fermi*-LAT flares are apparently produced in the vicinity of the Crab nebula pulsar wind termination shock. The relativistic electrons ejected from the central pulsar will have cooled substantially via synchrotron emission by the time they reach the shock, at a distance of $\sim 10^{17}$ cm, and therefore the production of the observed γ-ray emission at that distance implies the existence of an efficient acceleration mechanism. The acceleration is thought to occur in the vicinity of the shock via a variety of mechanisms, including first-order Fermi acceleration due to multiple shock crossings, second-order Fermi acceleration due to stochastic interactions with a random field of MHD waves, and direct electrostatic acceleration in the electric field generated in the magnetic reconnection region surrounding the shock. In this section, we derive the spatial and momentum diffusion coefficients describing the stochastic interaction with the random field of MHD waves.

The strongest possible MHD acceleration occurs in the Bohm regime, when the particle mean-free path is comparable to the Larmor radius (Krall & Trivelpiece 1986),

$$r_{\rm L} = \frac{pc}{qB} \ , \tag{4.12}$$

where c is the speed of light, q is the magnitude of the electron charge, and B is the local magnetic field strength. We therefore parameterize the mean-free path, ℓ, relative to the Larmor radius by writing

$$\ell = \eta \, r_{\rm L} \ , \tag{4.13}$$

where the constant $\eta \gtrsim 1$. The associated spatial diffusion coefficient, κ, for Bohm diffusion is given by (Dermer & Menon 2009)

$$\kappa = \frac{\eta c r_{\rm L}}{3} \ . \tag{4.14}$$

The general relation between the spatial diffusion coefficient κ and the momentum diffusion coefficient D can be written as (e.g., Reif 1965)

$$D(p)\kappa(p) = \frac{p^2 v_{\rm A}^2}{9} \ , \tag{4.15}$$

where $v_{\rm A}$ represents the Alfvén velocity of the MHD waves. Combining Equation (4.12), (4.14), and (4.15), we find that in the Bohm scenario, the momentum dependence of $D(p)$ is given by

$$D(p) = D_0 m_e c\, p \ , \tag{4.16}$$

where the constant D_0 has units of $\rm s^{-1}$. The value of D_0 is constrained by the requirement that the acceleration timescale must exceed the gyroperiod of the accelerated electrons, as discussed in Section 4.4.1.

4.2.3 Synchrotron Losses

The relativistic electrons in the Crab nebula loss energy primarily via the emission of synchrotron radiation. Assuming an isotropic electron distribution, the momentum loss rate due to synchrotron radiation can be written as

$$<\dot{p}>_{\rm loss} = -\frac{B_0}{m_e c} p^2 \ , \tag{4.17}$$

where the constant $B_0 \propto \rm s^{-1}$ is given by

$$B_0 = \frac{\sigma_{\rm T} B^2}{6\pi m_e c} \ . \tag{4.18}$$

The synchrotron energy loss rate per relativistic electron obtained by combining Equations (4.17) and (4.18) is (cf. Equation (4.4))

$$<\dot{\varepsilon}>_{\rm loss}= -\frac{4}{3}\frac{\sigma_{\rm T} U_B}{m_e^2 c^3}\,\varepsilon^2 \ , \tag{4.19}$$

where $\varepsilon = pc$ is the relativistic electron energy and $U_B = B^2/(8\pi)$ is the magnetic energy density.

4.2.4 Electrostatic and Shock Acceleration

In addition to the second-order Fermi acceleration discussed in Section 4.2.2, which the electrons experience as a result of stochastic wave-particle interactions, the particles also experience a combination of electrostatic and shock acceleration in the vicinity of the termination shock **?**. Electrostatic acceleration in an electric field of strength E, generated in the magnetic reconnection region around the shock, results in a constant momentum gain rate given by

$$<\dot{p}>_{\rm elec}= qE \ . \tag{4.20}$$

The electrostatic acceleration modeled by Equation (4.20) is extremely important in the pulsar wind application because it has the potential to accelerate electrons to energies far exceeding the conventional synchrotron burnoff limit, which is required in order to account for the observations of GeV γ-rays produced during the flares observed from the Crab nebula (Cerutti et al. 2012; Montani & Bernadini 2014).

The shape of the electron energy distribution resulting from first-order Fermi acceleration at the pulsar wind termination shock depends on the amount of time the particles spend in the acceleration region, which is regulated by the combined action of spatial diffusion and advection. The Crab pulsar termination shock is ultrarelativistic, with upstream Lorentz factor $\Gamma_u \sim 10^3 - 10^6$ (Lyubarsky 2003; Aharonian et al. 2004). On the downstream side of the shock, the flow is mildly relativistic, with speed $c/3$ in the shock frame (Achterberg et al. 2001). Since the termination shock is a standing shock, the shock frame is equivalent to the frame at infinity. Gallant & Achterberg (1999) show that the minimum cycle time, $t_{\rm cyc}$, required for a particle to cross the shock and return to the upstream side can be estimated, in the optimal case of Bohm diffusion, using

$$t_{\rm cyc} = \frac{r_{\rm L}}{\Gamma_u c} \ , \tag{4.21}$$

where $r_{\rm L}$ is the Larmor radius (see Equation (4.12)). Particles crossing the shock for the first time will experience an energy gain on the order of Γ_u^2 in the frame of the upstream gas, but subsequent crossings will increase the particle energy by a much smaller factor due to the dynamics of escape and acceleration. The first-order Fermi acceleration rate experienced by the electrons due to multiple shock crossings is computed in the laboratory (shock) reference frame using (e.g., Dermer & Menon 2009)

$$<\dot{p}>_{\rm shock} = \beta_{\rm eff} \frac{2p}{t_{\rm cyc}} = 2\beta_{\rm eff}\Gamma_u q B \ , \tag{4.22}$$

where the final result follows from Equations (4.12) and (4.21), and $\beta_{\rm eff}$ is an efficiency factor reflecting the fact that the particle acceleration rate cannot exceed the Bohm rate, even in a relativistic shock (Lemoine & Waxman 2009). The maximum value for the efficiency factor $\beta_{\rm eff}$ can be computed by setting $|<\dot{p}>_{\rm shock}|$ equal to the synchrotron loss rate $|<\dot{p}>_{\rm loss}|$ given by Equation (4.17) at the maximum Lorentz factor, $\gamma_{\rm MHD}$, given by Equation (4.8). The result obtained is

$$2\beta_{\rm eff}^{\rm max}\Gamma_u q B = \frac{\sigma_{\rm T} B^2 \gamma_{\rm MHD}^2}{6\pi} \ . \tag{4.23}$$

Solving this relation for $\beta_{\rm eff}^{\rm max}$, we conclude that in the pulsar wind application, the shock acceleration efficiency parameter $\beta_{\rm eff}$ must satisfy the constraint

$$\beta_{\rm eff} \le \beta_{\rm eff}^{\rm max} \equiv \frac{1}{2\zeta\Gamma_u} \ . \tag{4.24}$$

Using this result to eliminate $\beta_{\rm eff}$ in Equation (4.22), we find that the shock acceleration rate in the ultrarelativistic case is given by

$$<\!\dot{p}\!>_{\rm shock} = q\,\zeta^{-1}\rho B \ , \tag{4.25}$$

where we have defined the relative efficiency parameter, ρ, using

$$\rho \equiv \frac{\beta_{\rm eff}}{\beta_{\rm eff}^{\rm max}} \ . \tag{4.26}$$

The problem of estimating the value of ρ depends on many unknown physical details, such as the obliquity of the shock, and the distribution and mean coherence length of the MHD turbulence (Lemoine & Waxman 2009). Here, we will treat ρ as a free parameter in the range $0.1 \lesssim \rho < 1$. We will set $\rho = 0.1$ in our numerical examples.

Based on Equations (4.20) and (4.25), we conclude that in the pulsar wind application, the first-order momentum gain rate, $<\!\dot{p}\!>_{\rm gain}$, appearing in the transport equation (4.10) is actually composed of two constant components, with one describing electrostatic acceleration (Equation (4.20)), and the other describing shock acceleration (Equation (4.25)), so that

$$<\!\dot{p}\!>_{\rm gain} = <\!\dot{p}\!>_{\rm elec} + <\!\dot{p}\!>_{\rm shock} \ , \tag{4.27}$$

or, equivalently,

$$<\!\dot{p}\!>_{\rm gain} = qE + qB\rho\,\zeta^{-1} = A_0\,m_e c \ , \tag{4.28}$$

where the acceleration rate constant, $A_0 \propto \mathrm{s}^{-1}$, is defined by

$$A_0 \equiv \frac{q(E + B\rho\,\zeta^{-1})}{m_e c} \ . \tag{4.29}$$

4.2.5 Particle Escape

The one-zone model considered here represents an average over the acceleration and emission regions, and therefore the spatial diffusion of the particles through the nebula is treated implicitly using an escape-probability formalism. In this scenario, the electrons remain in the acceleration region for a mean time $t_{\rm esc}$ before escaping. In order for the model to accurately reflect the geometry of the pulsar-wind environment, the energy dependence of $t_{\rm esc}$ needs to be carefully considered, so that the dominant spatial transport processes on large and small scales are properly treated.

The nature of the electron's propagation through the pulsar wind nebula depends on its momentum, p, as depicted in Figure 4.1. For electrons with small momentum, the associated Larmor radius, $r_{\rm L} = pc/(qB)$, is much smaller than the pulsar wind termination shock radius, $r_t = 10^{17}\,$cm. In this case, the electrons are "trapped" in the flow, and the escape of the electrons from the acceleration region is regulated by advection in the outward direction (e.g., Becker & Begelman 1986). This is called "Shock-Regulated Escape" (SRE; see Steinacker & Schlickeiser 1989). Conversely, for electrons with large momentum, so that $r_{\rm L} \sim r_t$, the escape occurs via Bohm diffusion, with a mean-free path, ℓ, that is comparable to the Larmor radius $r_{\rm L}$ (see Equation (4.13)). This is called "Bohm diffusive escape" (e.g., Dermer & Menon 2009). Electrons with an intermediate momentum value tend to diffuse back into the upstream region, so that they are recycled through the shock, and experience additional acceleration.

In a proper three-dimensional numerical transport model, the large- and small-scale dependences of the particle propagation would automatically be taken into consideration as part of the simulation. Since we are using a simplified one-zone model here, representing an average over the acceleration/radiation regions, we must approximate the correct transport behavior by using a suitable expression for the dependence of the escape timescale $t_{\rm esc}(p)$ on the particle momentum p, taking into account both the large- and small-scale behaviors. The remainder of this Section focuses on the derivation of the correct functional form for $t_{\rm esc}(p)$.

Shock-Regulated Escape

In the shock-regulated escape model, the electron escape timescale, $t_{\rm esc}$, is proportional to the cycle timescale, $t_{\rm cyc}$, and the mean-free path is equal to the Larmor radius, corresponding to the limit of Bohm diffusion. It follows that particles with higher momentum take longer to cycle back from the downstream to the upstream side of the shock, and they also take longer to escape. We can use Equation (4.21) to write the momentum dependence of the shock-regulated escape timescale, $t_{\rm SRE}$, as (Jokipii 1987)

$$t_{\rm SRE}(p) \propto \frac{r_{\rm L}}{c} \propto p \ , \tag{4.30}$$

where we have used the fact that $r_{\rm L} \propto p$. We can quantify this relation by writing

$$t_{\rm SRE}(p) \equiv \frac{p}{C_0 m_e c} \ , \tag{4.31}$$

where $C_0 \propto {\rm s}^{-1}$ is the rate constant for shock-regulated escape. In the shock-regulated escape model, we find that $t_{\rm SRE} \propto p$, and therefore electrons with lower momenta tend to be trapped in the flow, and escape from the shock by advecting to larger radii on the downstream side of the shock (see Figure 4.1). The shock-regulated escape process therefore tends to harden the particle distribution, and enhance the high-energy component of the resulting synchrotron spectrum. In Section 4.3.2, we demonstrate that in the case of pure shock/electrostatic acceleration, the escape rate parameter C_0 defined in Equation (4.31) is linked with the acceleration rate parameter A_0 defined in Equation (4.29) via the relation

$m_{\rm shock} = -C_0/A_0$, where $m_{\rm shock}$ is the power-law spectral index of the electron number distribution for the case of pure electrostatic/shock acceleration.

Bohm Diffusive Escape

On spatial scales that are much larger than the thickness of the shock, the escape of particles is regulated by Bohm diffusion, which was discussed in Section 4.2.5. In this process, the electron diffusion mean-free path is given by $\ell = \eta r_{\rm L}$, where $r_{\rm L} = pc/(qB)$ is the electron's Larmor radius and η is an order-unity constant (see Equation (4.13)). The mean timescale for ultrarelativistic particles to escape into the outer region of the nebula (beyond the termination shock radius r_t) via this process, denoted by $t_{\rm Bohm}$, is therefore a function of the particle momentum, p, given by

$$t_{\rm Bohm}(p) \equiv \frac{r_t}{v_{\rm diff}} \ , \qquad v_{\rm diff} = \frac{c}{r_t/\ell} \ , \tag{4.32}$$

where $v_{\rm diff}$ is the Bohm diffusion velocity. The quantity $t_{\rm Bohm}$ represents the self-consistent timescale for escape via diffusion through a random field of MHD waves with wave index $q = 1$ (Becker et al. 2006; Dermer et al. 1996). Combining relations, we find that

$$t_{\rm Bohm}(p) = \frac{r_t^2 qB}{\eta c^2 p} \equiv \frac{m_e c}{F_0 p} \ , \tag{4.33}$$

where $F_0 \propto {\rm s}^{-1}$ is the rate constant for Bohm diffusive escape, defined by

$$F_0 \equiv \frac{\eta m_e c^3}{r_t^2 qB} = 2.56 \times 10^{-17}\ {\rm s}^{-1}\ \eta \left(\frac{r_t}{10^{17}\,{\rm cm}}\right)^{-2} \left(\frac{B}{200\,\mu{\rm G}}\right)^{-1} \ . \tag{4.34}$$

It follows from Equation (4.33) that electrons with sufficiently large momenta have a very small timescale for diffusive escape from the acceleration region. Of course, the escape timescale cannot be less than the light-crossing time for the termination shock radius, r_t, which corresponds to setting the diffusion velocity $v_{\rm diff} = c$. This is also equivalent to setting the mean-free path $\ell = r_t$, which is the Hillas (1984) condition, that can be used to calculate the Hillas upper limit, $\gamma_{\rm H}$, for the Lorentz factor of the electrons accelerated in the nebula. Using Equations (4.12) and (4.13), we obtain

$$\gamma_{\rm H} = \frac{r_t q B}{\eta m_e c^2} = 1.17 \times 10^{10}\ \eta^{-1} \left(\frac{r_t}{10^{17}\,{\rm cm}}\right) \left(\frac{B}{200\,\mu{\rm G}}\right)\ . \tag{4.35}$$

For the magnetic field assumed here, $B = 200\,\mu$G, and the termination shock radius $r_t = 10^{17}\,$cm, we find that the limiting Lorentz factor is $\gamma_{\rm H} \sim 10^{10}$. The associated maximum synchrotron energy computed by substituting $\gamma_{\rm H}$ into Equation (4.1) is in the GeV range, in agreement with the observed γ-ray emission from the Crab nebula.

Net Escape Rate

Taking into consideration Equations (4.31) and (4.33), we see that particles in the vicinity of the pulsar wind termination shock have two avenues available for escape from the acceleration region. Particles with small momentum p are like to advect away into the downstream region, since the shock-regulated escape timescale, $t_{\rm SRE}$, is small in this case according to Equation (4.31). On the other hand, particles with large momentum are likely to rapidly diffuse out of the nebula via Bohm diffusion, since in this case the Bohm diffusion timescale, $t_{\rm Bohm}$, is small, according to Equation (4.33). These two expressions can be combined to write down an expression for the net escape rate, given by

$$t_{\rm esc}^{-1}(p) = t_{\rm SRE}^{-1}(p) + t_{\rm Bohm}^{-1}(p)\ , \tag{4.36}$$

where $t_{\rm esc}(p)$ is the net escape timescale, taking both mechanisms into account. By combining Equations (4.31), (4.33), and (4.36), we find that the net escape timescale $t_{\rm esc}(p)$ can be written as

$$t_{\rm esc}(p) = \left(\frac{C_0 m_e c}{p} + \frac{F_0 p}{m_e c} \right)^{-1} \ . \tag{4.37}$$

This is the form for the escape timescale that will be substituted into the transport equation (4.10) in Section 4.2.6 in order to ensure that both the large- and small-scale behaviors are properly accounted for. The cross-over momentum, p_c, and Lorentz factor, γ_c, between the regions of dominance of the two escape mechanisms are computed by setting $t_{\rm SRE} = t_{\rm Bohm}$, which yields

$$\gamma_c = \frac{p_c}{m_e c} = \sqrt{\frac{C_0}{F_0}} \ . \tag{4.38}$$

In our numerical calculations, discussed in Section 4.4, we find that $\gamma_c \sim 10^{10} - 10^{11}$, which corresponds to a Larmor radius comparable to the termination-shock radius, $r_t = 10^{17}\,$cm.

4.2.6 Steady-State Transport Equation

The synchrotron lifetime given by Equation (4.6) provides a rough estimate for the time it takes the electron distribution to reach equilibrium. The fact that the synchrotron timescale is comparable to the flare duration suggests that the particle distribution during the peak of the flare is close to equilibrium. In this case, we are justified in setting the time derivative in Equation (4.10) equal to zero, and solving the steady-state transport equation. Hence the steady-state particle distribution we will obtain is best interpreted as the electron distribution during the peak of the flare.

Since Equation (4.10) is linear, it is sufficient to determine the steady-state Green's function, $f_{\rm G}(p, p_0)$, resulting from the reprocessing of monoenergetic seed particles, with source term

$$\dot{f}_{\rm source}(p) = \frac{\dot{N}_0 \, \delta(p - p_0)}{4 \pi p_0^2} \ , \tag{4.39}$$

corresponding to the continual injection of $\dot{N}_0$ electrons per unit time with momentum

p_0. Once the solution for $f_G(p, p_0)$ is known, the steady-state particular solution, $f(p)$, corresponding to an arbitrary source term, $\dot{f}_{\rm source}(p)$, can be obtained using the convolution

$$f(p) = \int_0^\infty \frac{4\pi p_0^2}{\dot{N}_0} \, f_{\rm G}(p, p_0) \, \dot{f}_{\rm source}(p_0) \, dp_0 \ . \tag{4.40}$$

By combining Equations (4.10), (4.16), (4.17), (4.28), (4.37), and (4.39), we find that in the pulsar wind nebula, the fundamental steady-state transport equation given by

$$\frac{\partial f}{\partial t} = -\frac{1}{p^2}\frac{\partial}{\partial p}\left[p^2\left(- D_0 m_e c \, p \frac{\partial f}{\partial p} + A_0 m_e c f - \frac{B_0 p^2}{m_e c} f\right)\right] \\ - \left(\frac{C_0 m_e c}{p} + \frac{F_0 p}{m_e c}\right) f + \frac{\dot{N}_0 \, \delta(p - p_0)}{4\pi p_0^2} = 0 \ , \tag{4.41}$$

where p_0 is the momentum of the injected electrons and $\dot{N}_0$ is the injection rate.

It is convenient to transform from the variables (p, t) to the dimensionless momentum, x, and the dimensionless time, y, defined by

$$x \equiv \frac{p}{m_e c}, \qquad x_0 \equiv \frac{p_0}{m_e c}, \qquad y \equiv D_0 t \ . \tag{4.42}$$

In general, the relationship between x and the Lorentz factor γ is given by $x = \sqrt{\gamma^2 - 1}$. Hence, for the ultrarelativistic ($x \gg 1$) electrons responsible for creating the γ-rays from the Crab pulsar wind nebula, we can write $x = \gamma$ without making any significant error. In terms of the new coordinates (x, y), the steady-state transport equation can be written as

$$\frac{\partial f_{\rm G}}{\partial y} = \frac{1}{p^2}\frac{\partial}{\partial x}\left[x^2\left(x\frac{\partial f_{\rm G}}{\partial x} - \tilde{A} f_{\rm G} + \tilde{B} x^2 f_{\rm G}\right)\right] - \frac{\tilde{C} f_{\rm G}}{x} - \tilde{F} x f_{\rm G} + \frac{\dot{N}_0 \, \delta(x - x_0)}{4\pi D_0 (m_e c)^3 x_0^2} = 0 \ , \tag{4.43}$$

where we have defined the dimensionless constants $\tilde{A}$, $\tilde{B}$, $\tilde{C}$, and $\tilde{F}$, using

$$\tilde{A} \equiv \frac{A_0}{D_0}, \qquad \tilde{B} \equiv \frac{B_0}{D_0}, \qquad \tilde{C} \equiv \frac{C_0}{D_0} \qquad \tilde{F} \equiv \frac{F_0}{D_0} \ . \tag{4.44}$$

4.2.7 Fokker-Planck Equation

It is instructive to rewrite Equation (4.43) in the form of a Fokker-Planck equation by defining the electron number distribution, $N_{\rm G}$, using

$$N_{\rm G}(x, x_0, y) \equiv 4\pi(m_e c)^3 x^2 f_{\rm G}(x, x_0, y) \ . \tag{4.45}$$

Note that the total number of electrons, N_e, is related to $N_{\rm G}$ via (cf. Equation (4.11))

$$N_e(y) = \int_0^\infty N_{\rm G}(x, x_0, y)\, dx \ . \tag{4.46}$$

Using Equation (4.45) to substitute for $f_{\rm G}$ in Equation (4.43) and rearranging terms yields the steady-state Fokker-Planck equation,

$$\frac{\partial N_{\rm G}}{\partial y} = \frac{\partial^2}{\partial x^2}\left(\frac{1}{2}\,\frac{d\sigma^2}{dy}\,N_{\rm G}\right) - \frac{\partial}{\partial x}\left(\left\langle\frac{dx}{dy}\right\rangle N_{\rm G}\right) - \frac{\tilde{C}}{x}\,N_{\rm G} - \tilde{F}xN_{\rm G} + \frac{\dot{N}_0\,\delta(x - x_0)}{D_0} = 0 \ , \tag{4.47}$$

where the "broadening" and "drift" coefficients are given, respectively, by

$$\frac{1}{2}\,\frac{d\sigma^2}{dy} = x \ , \qquad \left\langle\frac{dx}{dy}\right\rangle = 3 + \tilde{A} - \tilde{B}\,x^2 \ . \tag{4.48}$$

These expressions for the Fokker-Planck coefficients will be used in Section 4.4 to help us analyze the energy budget of the observed flares, and to determine the relative importance of electrostatic and stochastic acceleration in creating the distribution of relativistic electrons.

4.3 Particle Distribution and Radiation Spectrum

In this section, we obtain the closed-form solution for the steady-state electron Green's function, $N_{\rm G}$, representing the number distribution of electrons in dimensionless momentum x space (or equivalently, in Lorentz factor space γ). We also convolve the particle distribution with the synchrotron emission function to obtain the γ-ray spectrum emitted by the relativistic electrons accelerated at the pulsar wind termination shock.

4.3.1 Electron Green's Function

In a steady-state situation, $N_{\rm G}$ satisfies the ordinary differential equation

$$x\,\frac{d^2N_{\rm G}}{dx^2} + (\tilde{B}\,x^2 - 1 - \tilde{A})\,\frac{dN_{\rm G}}{dx} + \left(2\tilde{B}\,x - \frac{\tilde{C}}{x} - \tilde{F}x\right) N_{\rm G} = -\frac{\dot{N}_0\,\delta(x - x_0)}{D_0} \ . \tag{4.49}$$

The Green's function $N_{\rm G}$ must be continuous at the injection momentum, $x = x_0$, and its derivative displays a jump there, which can be evaluated by integrating Equation (4.49) with respect to x over a small region surrounding x_0. The result obtained is

$$\lim_{\delta\to 0}\,\frac{dN_{\rm G}}{dx}\bigg|_{x_0+\delta} - \frac{dN_{\rm G}}{dx}\bigg|_{x_0-\delta} = -\frac{\dot{N}_0}{D_0 x_0} \ . \tag{4.50}$$

The fundamental solutions to the homogeneous equation obtained when $x \neq x_0$, satisfying appropriate boundary conditions at large and small values of x, can be expressed in terms of the Whittaker functions $M_{\kappa,\mu}$ and $W_{\kappa,\mu}$ using

$$N_{\rm G}(x, x_0) \ \propto \ e^{-\tilde{B}x^2/4}\ x^{\tilde{A}/2} \begin{cases} M_{\kappa,\mu}(\tilde{B}x^2/2) \ , & x \le x_0 \ , \\ W_{\kappa,\mu}(\tilde{B}x^2/2) \ , & x \ge x_0 \ , \end{cases} \tag{4.51}$$

where the parameters κ and μ are defined by

$$\kappa \equiv 1 + \frac{\tilde{A}}{4} - \frac{\tilde{F}}{2\tilde{B}} \ , \qquad \mu \equiv \frac{\sqrt{(2+\tilde{A})^2 + 4\,\tilde{C}}}{4} \ . \tag{4.52}$$

The continuity of the Green's function at $x = x_0$ implies that we can express the global solution for $N_{\rm G}$ using

$$N_{\rm G}(x, x_0) = Q_0 \left(\frac{x}{x_0}\right)^{\tilde{A}/2} e^{-\tilde{B}(x^2 - x_0^2)/4} M_{\kappa,\mu}\left(\frac{\tilde{B} x_{\rm min}^2}{2}\right) W_{\kappa,\mu}\left(\frac{\tilde{B} x_{\rm max}^2}{2}\right) \ , \tag{4.53}$$

where the normalization constant Q_0 is determined by applying the derivative jump condition, and we have made the definitions

$$x_{\rm min} \equiv \min(x, x_0) \ , \qquad x_{\rm max} \equiv \max(x, x_0) \ . \tag{4.54}$$

Substituting Equation (4.53) into Equation (4.50) yields

$$\tilde{B} x_0 Q_0 \left[M_{\kappa,\mu}\left(\frac{\tilde{B} x_0^2}{2}\right) W'_{\kappa,\mu}\left(\frac{\tilde{B} x_0^2}{2}\right) - W_{\kappa,\mu}\left(\frac{\tilde{B} x_0^2}{2}\right) M'_{\kappa,\mu}\left(\frac{\tilde{B} x_0^2}{2}\right)\right] = -\frac{\dot{N}_0}{D_0 x_0} \ . \tag{4.55}$$

We can evaluate the Wronskian in the square brackets using (Abramowitz & Stegun 1970)

$$M_{\kappa,\mu}(z) W'_{\kappa,\mu}(z) - W_{\kappa,\mu}(z) M'_{\kappa,\mu}(z) = -\frac{\Gamma(1+2\mu)}{\Gamma(\mu - \kappa + 1/2)} \ . \tag{4.56}$$

Combining Equations (4.55) and (4.56), we obtain for the normalization coefficient

$$Q_0 = \frac{\dot{N}_0 \Gamma(\mu - \kappa + 1/2)}{\tilde{B} D_0 \Gamma(1+2\mu) x_0^2} \ , \tag{4.57}$$

which can be substituted into Equation (4.53) to obtain the final result for the electron Green's function,

$$N_{\rm G}(x, x_0) = \frac{\dot{N}_0 \Gamma(\mu - \kappa + 1/2)}{\tilde{B} D_0 \Gamma(1 + 2\mu)\, x_0^2} \left(\frac{x}{x_0}\right)^{\tilde{A}/2} e^{-\tilde{B}(x^2 - x_0^2)/4} M_{\kappa,\mu}\left(\frac{\tilde{B} x_{\rm min}^2}{2}\right) W_{\kappa,\mu}\left(\frac{\tilde{B} x_{\rm max}^2}{2}\right) , \tag{4.58}$$

where κ and μ are given by Equations (4.52) and $x_{\rm min}$ and $x_{\rm max}$ are given by Equations (4.54). The solution to the steady-state transport equation given by Equation (4.58) represents the electron distribution resulting from a balance between particle injection, acceleration, energy losses, and particle escape.

The general shape of the particle distribution is a peak around the injection momentum x_0, surrounded by power-law sections, and terminating in a high-energy exponential cutoff where synchrotron losses overwhelm particle acceleration. Examples of the particle distribution for the Crab nebula application are plotted and discussed in Section 4.5. The electron distribution given by Equation (4.58) can be used to compute the theoretical synchrotron spectrum produced from a population of radiating relativistic electrons accelerated in the nebula under the combined action of stochastic MHD wave-particle interactions, electrostatic acceleration, shock acceleration, particle escape, and synchrotron losses. In Section 4.5, we will compare the model predictions with the observational γ-ray data and analyze the energetics of the flares.

4.3.2 Approximate Power-Law Solution for $N_{\rm G}$

Equation (4.58) for the electron number distribution, $N_{\rm G}$, represents the exact solution to the steady-state Fokker-Planck equation (4.47). It is interesting to note that for values of the particle momentum p far below the onset of the synchrotron losses in Equation (4.47), and also below the cross-over momentum indicating the onset of Bohm diffusion (see Equation (4.38)), we find that Equation (4.47) reduces to an equidimensional equation, which implies the existence of power-law solutions of the form

$$N_{\rm G}(x, x_0) = H_0 x^m \ , \tag{4.59}$$

where H_0 is a normalization constant and m is an unknown power-law index. By substituting the power-law form $N_{\rm G}(x) \propto x^m$ into Equation (4.49) and simplifying, we can obtain a quadratic equation for m, given by

$$m^2 - (2 + \tilde{A})\, m - \tilde{C} = 0 \ , \tag{4.60}$$

with corresponding solutions

$$m_{\pm} = \frac{2 + \tilde{A} \pm \sqrt{(2 + \tilde{A})^2 + 4\tilde{C}}}{2} \ . \tag{4.61}$$

Here, the positive power-law index m_+ applies at low energies ($x < x_0$), and the negative index m_- applies at high energies ($x > x_0$). The global solution for $N_{\rm G}$ can now be written as

$$N_{\rm G}(x, x_0) = \ H_0 \begin{cases} \left(\frac{x}{x_0}\right)^{m_+} \ , & x \le x_0 \ , \\ \left(\frac{x}{x_0}\right)^{m_-} \ , & x \ge x_0 \ , \end{cases} \tag{4.62}$$

where the normalization constant H_0 can be determined via application of the derivative jump condition given by Equation (4.50). After some algebra, the result obtained is

$$H_0 = \frac{\dot{N}_0}{4 D_0 \mu} \ . \tag{4.63}$$

This normalization coefficient can be substituted back into Equation (4.62) to obtained the properly normalized global solution for $N_{\rm G}$, given by

$$N_{\rm G}(x, x_0) = \frac{\dot{N}_0}{4D_0\mu} \begin{cases} \left(\frac{x}{x_0}\right)^{m_+} , & x \le x_0 \ , \\ \left(\frac{x}{x_0}\right)^{m_-} , & x \ge x_0 \end{cases} \tag{4.64}$$

The broken power-law solution given by Equation (4.64) is valid if we restrict attention to values of x below the exponential turnover created by synchrotron losses, and also below the cross-over Lorentz factor, γ_c, where the transition to Bohm diffusive escape occurs (see Equation (4.38)). We will compare the approximate power-law solution with the exact solution in our applications to the Crab nebula flares in Section 4.5.

4.3.3 Power-Law Index for Electrostatic/Shock Acceleration

We have demonstrated that for energies below the onset of synchrotron losses, the particle distribution is well represented by a broken power-law. A case of particular interest is the case of pure electrostatic/shock acceleration, which corresponds to the limit $D_0 \to 0$, where D_0 is the momentum diffusion rate coefficient. Physically, momentum diffusion is the result of stochastic wave-particle interactions. In the limit $D_0 \to 0$, the contribution to the acceleration due to the random motions of the MHD waves vanishes, and we are left with only the contribution due to electrostatic/shock acceleration. We can explore this limit in detail by using Equations (4.44) to make the substitutions $\tilde{A} = A_0/D_0$ and $\tilde{C} = C_0/D_0$ in Equation (4.61) for the power-law index $m_\pm$. The result obtained for the high-energy index, m_-, is

$$m_- = \left(1 + \frac{A_0}{2D_0}\right) - \frac{1}{2}\sqrt{\left(2 + \frac{A_0}{D_0}\right)^2 + \frac{4C_0}{D_0}} \ , \tag{4.65}$$

which can be rewritten as

$$m_- = \left(1 + \frac{A_0}{2D_0}\right)\left[1 - \sqrt{1 + \frac{4D_0C_0}{A_0^2}\left(\frac{2D_0}{A_0} + 1\right)^{-2}}\right] . \tag{4.66}$$

Making an expansion in terms of the small parameter D_0/A_0 and keeping only the highest-order term yields the power-law index of the electron number distribution for the case of pure electrostatic/shock acceleration. After some algebra, the result obtained is

$$m_{\rm shock} \equiv \lim_{D_0 \to 0} m_- = -\frac{C_0}{A_0} = -\frac{\tilde{C}}{\tilde{A}} . \tag{4.67}$$

In the case of strong electrostatic/shock acceleration, we expect to find that the high-energy power-law index $m_{\rm shock}$ is in the range $-3 \lesssim m_{\rm shock} \lesssim -2$, as is typically found in PIC simulations of acceleration in regions of magnetic reconnection near the Crab pulsar termination shock (e.g., Cerutti et al. 2014).

4.3.4 Synchrotron Spectrum

The γ-rays emitted during the recent flares observed from the Crab nebula are thought to represent direct synchrotron radiation produced by the relativistic electrons accelerated at the pulsar wind termination shock (Buehler at al. 2012; Abdo et al. 2011). Since synchrotron losses are included in the transport equation we have solved (Equation (4.41)), we are now in a position to self-consistently calculate the resulting γ-ray spectrum. Assuming an isotropic distribution of electrons, the theoretical synchrotron spectrum can be computed by convolving the electron Green's function (Equation (4.58)) with the synchrotron emission function, P_ν, which gives the power emitted per electron per Hz. The isotropic synchrotron emission function is given by (e.g., Rybicki & Lightman 1979)

$$P_\nu(\nu,\gamma) = \frac{\sqrt{3}\, q^3 B}{m_e c^2} R\left(\frac{\nu}{\gamma^2 \nu_s}\right) \quad \propto \quad \text{erg s}^{-1}\ \text{Hz}^{-1} \ , \tag{4.68}$$

where

$$\nu_s \equiv \frac{3qB}{4\pi m_e c} \ , \tag{4.69}$$

and

$$R(x) \equiv \frac{x^2}{2} K_{4/3}\Big(\frac{x}{2}\Big) K_{1/3}\Big(\frac{x}{2}\Big) - \frac{3x^3}{20}\Big[K^2_{4/3}\Big(\frac{x}{2}\Big) - K^2_{1/3}\Big(\frac{x}{2}\Big)\Big] \ , \tag{4.70}$$

Crusius & Schlickeiser (1986). Here, $K_{4/3}(x)$ and $K_{1/3}(x)$ denote modified Bessel functions of the second kind. The synchrotron spectrum emitted by the entire electron distribution is computed by performing the integral convolution

$$P^{\rm tot}_\nu(\nu) = \int_1^\infty N_{\rm G}(\gamma,\gamma_0) P_\nu(\nu,\gamma) d\gamma \ \propto \ \text{erg s}^{-1}\ \text{Hz}^{-1} \ , \tag{4.71}$$

where $N_{\rm G}$ is evaluated using the analytic solution for the electron distribution given by Equation (4.58). The corresponding observational flux levels are given by

$$\mathscr{F}_\nu(\nu) = \frac{1}{4\pi D^2} \int_1^\infty N_{\rm G}(\gamma,\gamma_0) P_\nu(\nu,\gamma) d\gamma \ \propto \ \text{erg s}^{-1}\ \text{cm}^{-2}\ \text{Hz}^{-1} \ , \tag{4.72}$$

where D is the distance to the source and $N_{\rm G}$ is given by Equation (4.58), and we remind the reader that $\gamma = x$ for the ultrarelativistic electrons of interest here.

4.4 Application to the Crab Nebula Flares

In this section, we test our model for the transport and acceleration of relativistic electrons at a pulsar wind termination shock by making an application to the interpretation of the γ-ray flares observed from the Crab nebula using *Fermi*-LAT. We also examine the constraints on the model parameters required in order to ensure that the computational results we obtain are physically reasonable.

4.4.1 Parameter Constraints

In the model considered here, the stochastic acceleration is due to repeated interactions between the relativistic electrons and a random field of MHD waves propagating with the Alfvén velocity $v_{\rm A}$ in the local magnetic field. In this scenario, discussed in Section 4.2.2, the momentum diffusion coefficient $D(p)$ is given by $D(p) = D_0 m_e c$, where the diffusion rate constant D_0 can be computed explicitly by combining Equations (4.12), (4.14), and (4.15) to obtain

$$D_0 = \frac{qB\sigma_{\rm mag}}{3\eta m_e c} = 1172 \ {\rm s}^{-1} \ \sigma_{\rm mag} \left(\frac{B}{200\,\mu{\rm G}}\right) \ \eta^{-1} \ , \tag{4.73}$$

where the constant $\eta \gtrsim 1$, and the magnetization parameter, $\sigma_{\rm mag}$, is defined using (e.g., Sironi & Spitkovsky 2014)

$$\sigma_{\rm mag} \equiv \left(\frac{v_{\rm A}}{c}\right)^2 \ . \tag{4.74}$$

As discussed in Section 4.1.1, the radiation-reaction (synchrotron burnoff) limit places severe constraints on the stochastic particle acceleration rate resulting from collisions between electrons and MHD waves. We can use this fact to develop a quantitative restriction on the value of the diffusion rate constant, D_0. We begin by writing the mean stochastic momentum gain rate as (e.g., Becker et al. 2006)

$$<\dot{p}>_{\rm stoch} = \frac{1}{p^2}\frac{\partial}{\partial p}\left[p^2 D(p)\right] = 3D_0 m_e c \ , \tag{4.75}$$

where the final result follows from Equation (4.16). The synchrotron momentum loss rate is likewise obtained by combining Equations (4.17) and (4.18), which yields

$$<\dot{p}>_{\rm syn} = -\frac{\sigma_{\rm T} B^2 p^2}{6\pi m_e^2 c^2} \ . \tag{4.76}$$

The maximum possible momentum that can be achieved via stochastic MHD acceleration in the presence of synchrotron losses was found to be (see Equation (4.8))

$$p_{\rm MHD} = m_e c \sqrt{\frac{6\pi q}{B\,\zeta\,\sigma_{\rm T}}} \ , \tag{4.77}$$

where ζ is an order unity constant. This result was obtained by equating the synchrotron loss timescale with the Larmor timescale. The synchrotron burnoff limit requires that the stochastic gain rate cannot exceed the synchrotron loss rate at the highest energy of interest in the problem, which implies that

$$\left(<\dot{p}>_{\rm stoch} + <\dot{p}>_{\rm syn}\right)\Big|_{p=p_{\rm MHD}} \le 0 \ . \tag{4.78}$$

We can use this inequality to constrain the value of the momentum diffusion constant, D_0. Combining Equations (4.75), (4.76), (4.77), and (4.78), we obtain

$$D_0 \le D_0^{\rm max} \ , \tag{4.79}$$

where

$$D_0^{\max} \equiv \frac{qB}{3m_e c\zeta} = 1172 \text{ s}^{-1} \left(\frac{B}{200\,\mu\text{G}}\right) \zeta^{-1} \tag{4.80}$$

represents the maximum value of D_0 such that the synchrotron burnoff limit is not violated at the maximum momentum for MHD acceleration, given by Equation (4.77). We point out that the value of D_0 calculated using the MHD model (Equation (4.73)) will automatically satisfy the synchrotron burnoff constraint given by Equation (4.79) provided $\zeta \sim 1$, $\eta \sim 1$, and $v_{\rm A} \sim c$, which are all reasonable expectations in the pulsar wind nebula. However, in our applications, we will check to ensure that D_0 satisfies Equation (4.79).

4.4.2 Maximum Radiation Energy

We have confirmed that when the synchrotron burnoff limit is taken into consideration, the maximum Lorentz factor, $\gamma_{\rm MHD}$, resulting from MHD wave acceleration (Equation (4.8)) yields a maximum photon energy, $\epsilon_{\rm MHD} \sim 158\,\text{MeV}$ (Equation (4.9)), that is too low to account for the GeV γ-ray emission observed using the *Fermi*-LAT instrument during the Crab nebula flares. This motivates the incorporation of electrostatic acceleration into the model, since this process can extend the maximum particle energy into the range required to reproduce the observations (Buehler at al. 2012; Cerutti et al. 2012).

The transport equation considered here includes electrostatic and stochastic acceleration, as well as synchrotron losses and particle escape. We can estimate the maximum particle energy achieved in our model by examining the Fokker-Planck "drift" coefficient given by Equation (4.48). This yields for the mean rate of change of the momentum

$$\left\langle \frac{dp}{dt} \right\rangle = D_0\, m_e c \left\langle \frac{d\gamma}{dy} \right\rangle = D_0\, m_e c\, (3 + \tilde{A} - \tilde{B}\,\gamma^2) \ , \tag{4.81}$$

where we have used the fact that $\gamma = x \equiv p/(m_e c)$ for the ultrarelativistic electrons considered here. We can compute the maximum Lorentz factor, corresponding to a balance between acceleration and synchrotron losses, by setting $<dp/dt>= 0$, which yields

$$\gamma^2_{\rm max} = \frac{\tilde{A}+3}{\tilde{B}} = \frac{A_0+3D_0}{B_0} \ . \tag{4.82}$$

This result can be rewritten as

$$\gamma^2_{\rm max} = \gamma^2_{\rm elec} + \gamma^2_{\rm shock}\,\rho + \gamma^2_{\rm MHD}\,\frac{D_0}{D_0^{\rm max}} \ , \tag{4.83}$$

where $\gamma_{\rm MHD}$ is the maximum Lorentz factor for pure MHD acceleration given by Equation (4.8), $D_0^{\rm max}$ is the maximum value of D_0 defined by Equation (4.80), and ρ is the shock acceleration efficiency parameter defined by Equation (4.26). The quantities $\gamma_{\rm elec}$ and $\gamma_{\rm shock}$ represent the maximum Lorentz factors for pure electrostatic acceleration and pure shock acceleration (at the Bohm rate), respectively, defined by

$$\gamma^2_{\rm elec} \equiv \frac{6\pi qE}{\sigma_{\rm T}B^2} \ , \tag{4.84}$$

and

$$\gamma^2_{\rm shock} \equiv \frac{6\pi q}{B\,\zeta\,\sigma_{\rm T}} = \gamma^2_{\rm MHD} \ , \tag{4.85}$$

where we have made use of Equations (4.18) and (4.29). Note that $\gamma_{\rm shock} = \gamma_{\rm MHD}$, as expected, since both the shock acceleration rate and the stochastic wave-particle acceleration rate are limited by synchrotron burnoff.

Cerutti et al. (2013a) also derived an expression for the maximum Lorentz factor for pure electrostatic acceleration, and it is interesting to compare their result with ours. They give the maximum Lorentz factor as a function of the particle pitch angle θ in their Equation (1), which can be written as

$$\gamma^2_{\rm elec}(\theta) = \frac{4\pi qE}{\sigma_{\rm T}B^2\sin^2\theta} \ . \tag{4.86}$$

In the present paper, we are assuming an isotropic distribution of electron velocities. We can average the Cerutti et al. (2013a) result with respect to pitch angle by noting that $< \sin^2\theta >= 2/3$, in which case we obtain our result given by Equation (4.84). Hence the two results for the maximum Lorentz factor for pure electrostatic acceleration are consistent.

Using Equations (4.83), (4.84), and (4.85) to substitute for γ in Equation (4.1) yields an expression for the peak photon energy during the flare, taking into account stochastic MHD acceleration, shock acceleration, and electrostatic acceleration. The result obtained is

$$\epsilon_{\rm max} \equiv \epsilon_{\rm pk}(\gamma_{\rm max}) = \frac{6\pi\,\xi q\, m_e c^2}{B_{\rm crit}\sigma_{\rm T}} \left[\frac{E}{B} + \frac{\rho}{\zeta} + \frac{1}{\zeta}\,\frac{D_0}{D_0^{\rm max}}\right] \ , \tag{4.87}$$

which can be rewritten as

$$\epsilon_{\rm max} = 158 \ {\rm MeV} \ \xi \ \left[\frac{E}{B} + \frac{\rho}{\zeta} + \frac{1}{\zeta}\,\frac{D_0}{D_0^{\rm max}}\right] \ . \tag{4.88}$$

In the absence of electrostatic and shock acceleration, we regain the peak energy given by Equation (4.9), which is not adequate to explain the highest energy photons emitted during the γ-ray flares from the Crab nebula. A maximum photon energy of $\sim 1\,$GeV can be obtained if $E/B \gtrsim 5$, but it is not clear whether this can be achieved if the magnetic field is equal to the ambient value in the nebula, $B \sim 200\,\mu$G. This led Cerutti et al. (2012) to hypothesize that the magnetic field is reduced in the reconnection region, where the particle acceleration is thought to occur, and therefore a larger ratio of E/B may be possible. In the model considered here, we have adopted the ambient field value, $B \sim 200\,\mu$G, but the required electric field value is reduced by the shock acceleration contribution.

4.4.3 Electrostatic Acceleration Versus Shock Acceleration

We have found that in the pulsar wind termination shock, the systematic first-order momentum gain rate is given by (see Equations (4.20), (4.25), and (4.28))

$$< \dot{p} >_{\rm gain} = < \dot{p} >_{\rm elec} + < \dot{p} >_{\rm shock} = qE + qB\rho\zeta^{-1} \ . \tag{4.89}$$

It is interesting to compare the relative contributions from shock acceleration and electrostatic acceleration in the vicinity of the termination shock. We have

$$\frac{< \dot{p} >_{\rm shock}}{< \dot{p} >_{\rm elec}} = \frac{\rho B}{\zeta E} \ . \tag{4.90}$$

The efficiency factor ρ is set at 0.1 while $\zeta = 1$. Adopting these values in Equation (4.90) yields

$$\frac{< \dot{p} >_{\rm shock}}{< \dot{p} >_{\rm elec}} \approx 0.10 \ \frac{B}{E} \ , \tag{4.91}$$

In our numerical results for the Crab nebula flares, we generally find that $B/E \sim 0.2$, and therefore we can conclude from Equation (4.91) that the first-order systematic momentum gain at the termination shock is dominated by electrostatic acceleration, rather than shock acceleration. However, it should be emphasized that despite the negligible role of shock acceleration, the shock nonetheless plays a crucial role in regulating the escape of particles from the acceleration region, and therefore the shock is an essential ingredient in the model.

4.4.4 Crab Nebula γ-Ray Flare Spectra

Application of our model requires the specification of the dimensionless theory parameters $\tilde{A}$, $\tilde{B}$, $\tilde{C}$, and $\tilde{F}$, the magnetic field strength, B, the Lorentz factor of the injected electrons, x_0, and the electron injection rate, $\dot{N}_0$. We remind the reader that the parameters $\tilde{A}$, $\tilde{B}$, $\tilde{C}$, and $\tilde{F}$ describe, in turn, the effects of electrostatic/shock acceleration, synchrotron losses, shock-regulated particle escape, and Bohm diffusive particle escape. Using Equations (4.18), (4.29), (4.34), (4.44), and (4.60), we find that the dimensionless parameters are related to the physical properties of the plasma via

$$\tilde{A} = \frac{q(E + B\rho\,\zeta^{-1})}{m_e c D_0} \ , \quad \tilde{B} = \frac{\sigma_{\rm T} B^2}{6\pi m_e c D_0} \ , \quad \tilde{C} = m_-^2 - (2 + \tilde{A})m_- \ , \quad \tilde{F} = \frac{6\pi\eta m_e^2 c^4}{r_t^2 q B^3 \sigma_{\rm T}} \tilde{B} \ , \tag{4.92}$$

where m_- is the high-energy electron power-law index discussed in Section 4.3.2. In our approach, we treat $\tilde{A}$, $\tilde{B}$, and $\tilde{C}$ as free parameters, and then compute m_- and $\tilde{F}$ using the final two relations in Equations (4.92). Hence $\tilde{F}$ and m_- are not free parameters in our model.

In our consideration of the γ-ray flares from the Crab nebula, the magnetic field strength is set to the value $B = 200\,\mu$G, in agreement with multiple studies of the quiescent emission from the Crab nebula (e.g., Aharonian et al. 2004; Meyer et al. 2010). The termination shock radius is set to the value $r_t = 10^{17}$ cm (Montani & Bernadini 2014). In the present paper, we do not perform detailed quantitative fits, because our goal is to make general comparisons between the model and the spectral data. We plan to develop quantitative fits in future work. The remaining model free parameters $\tilde{A}$, $\tilde{B}$, $\tilde{C}$, x_0, and $\dot{N}_0$ are varied until a reasonable qualitative fit to the γ-ray spectral data is obtained for a given flare. We set $\zeta = 1$, $\eta = 1$, and $\rho = 0.1$ in all of our numerical calculations.

Once the theory parameters have been estimated by using the model to qualitatively fit the γ-ray spectrum for a given flare, the value of the momentum diffusion parameter D_0 and the value of the electric field E are computed by rearranging Equations (4.92) to obtain

$$D_0 = \frac{\sigma_{\rm T} B^2}{6\pi m_e c \tilde{B}} \ , \qquad E = \frac{\sigma_{\rm T} B^2 \tilde{A}}{6\pi \tilde{B} q} - \frac{B\rho}{\zeta} \ . \tag{4.93}$$

In Figure 4.2, we plot the γ-ray spectra computed using Equation (4.72) along with the data for the five flares observed by *Fermi*-LAT and *AGILE* and discussed by Abdo et al. (2011), Buehler et al. (2012), Buehler & Blandford (2014), and Striani et al. (2013). The theory parameters have been varied to obtain a reasonably good qualitative fit to the γ-ray data for each flare. It is clear from Figure 4.2 that the analytical electron transport model considered here is able to roughly reproduce the observed γ-ray spectra for each of the observed *Fermi*-LAT flares. The corresponding model parameters are reported in Table 2.1. We have set $\zeta = 1$, $\eta = 1$, and $\rho = 0.1$ in all of the flare spectrum computations. The magnetic field strength is consistent for all of the models, $B = 200\,\mu$G, and therefore the maximum value for D_0 computed using Equation (4.80) is the same, $D_0^{\rm max} = 1172$. In each case, we observe that $D_0 < D_0^{\rm max}$, as required, which confirms that our model is not violating the synchrotron burnoff limit.

Table 2.1 also includes the cross-over Lorentz factor, γ_c, computed using Equation (4.38), which represents the energy at which the transition occurs between shock-regulated escape at low energies and Bohm diffusive escape at high energies. In our applications to the Crab nebula flares, we find that $\gamma_c \sim 10^{10} - 10^{11}$. The Hillas (1984) condition implies that the maximum particle Lorentz factor in the nebula is $\gamma_{\rm H} \sim 10^{10}$ (see Equation (4.35)), and therefore we conclude that when $\gamma_c \sim 10^{11}$, Bohm diffusion is not a significant contributor to the particle escape. We also list in Table 2.1 the values obtained for the high-energy power-law index, m_-, computed using Equation (4.61).

The corresponding electron distributions for each flare are plotted in Figures 4.3 and 4.4. The plots include a comparison of the exact solution for $N_{\rm G}$ computed using Equation (4.58) with the approximate power-law solution given by Equation (4.64). We note that the agreement between the asymptotic and exact solutions is excellent, up to the energy where synchrotron losses become dominant, and the electron distribution transitions into an exponential turnover. The electron distributions for the 2009 February, 2010 September, and 2013 March flares are plotted in Figure 4.3. In each of these cases, the electron distribution closely resembles the broken power-law solution, with the break occurring at the injection Lorentz factor γ_0. On the high-energy side, the spectrum extends as a straight power-law until the exponential turnover begins, at $\gamma \sim 10^{10}$, and there is no particle pile-up visible. We note that the maximum value of γ is in good agreement with the predicted upper limit $\gamma_{\rm H} \sim 10^{10}$ set by the Hillas condition (see Equation (4.35)).

The electron distributions for the 2007 September and 2011 April flares are plotted in Figure 4.4. In these two cases, the electron distributions resemble the approximate broken power-law solution at low energies, but it displays a distinctive pile-up at the maximum Lorentz factor $\gamma \sim 10^{10}$, resulting in the sharply peaked γ-ray spectra for these two flares, as depicted in Figure 4.2. The maximum particle energy is in agreement with the Hillas upper limit $\gamma_{\rm H} \sim 10^{10}$ given by Equation (4.35). The 2007 September and 2011 April flares also have the flattest high-energy power-law index for the electron distribution, with $m_- \sim -0.3$ (see Table 2.1), suggesting that extremely efficient electrostatic/shock acceleration is occurring during these two flares. Hence we view the 2007 September and 2011 April flares as indicative of the strongest particle acceleration ever observed in the Crab nebula.

We can determine the specific amount of acceleration associated with the shock and the electric field by writing the acceleration parameter $\tilde{A}$ as the sum

$$\tilde{A} = \tilde{A}_{\rm shock} + \tilde{A}_{\rm elec} \ , \tag{4.94}$$

where the electric field and shock acceleration parameters, $\tilde{A}_{\rm elec}$ and $\tilde{A}_{\rm shock}$, respectively, are given by

$$\tilde{A}_{\rm elec} \equiv \frac{qE}{m_e c D_0} \ , \qquad \tilde{A}_{\rm shock} \equiv \frac{qB\rho}{m_e c D_0 \zeta} \ . \tag{4.95}$$

The results for $\tilde{A}_{\rm elec}$ and $\tilde{A}_{\rm shock}$ are included in the Crab nebula γ-ray flare parameters listed in Table 2.1, and one can see that electrostatic acceleration dominates in each flare model, as expected. It is apparent that the production of the γ-ray flares requires substantial electrostatic acceleration, as expected. The inferred electric field values in the magnetic reconnection layer found using Equation (4.93) falls in the range $E \sim 50 - 600\,\mu$G in Gaussian units for an ambient magnetic field $B = 200\,\mu$G. These values generally satisfy the condition $E \gtrsim B$, which is consistent with rapid magnetic reconnection, giving rise to efficient electrostatic acceleration. The only exception is the weakest flare, observed in 2009 February, for which we obtain $E/B \sim 0.25$. However, this particular flare barely exceeded the level of the quiescent nebular emission, so our results are reasonable in the sense that strong electrostatic acceleration is not required to explain the spectrum observed during that flare.

The values for the magnetization parameter $\sigma_{\rm mag}$ obtained by substituting B, η, and D_0 into Equation (4.73) are reported in Table 4.1. We find that $0.04 \lesssim \sigma_{\rm mag} \lesssim 0.1$, which is within the range deduced by Mori et al. (2004) in their analysis of the asymmetry of the X-ray brightness between the far and near sides of the equatorial region of the nebula. However, it should be emphasized that the value of $\sigma_{\rm mag}$ is not well constrained by the observations or the models, and could range from $\sigma_{\rm mag} \sim 10^{-3}$ in the magnetohydrodynamical models (e.g., Kennel & Coroniti 1984) up to $\sigma_{\rm mag} \sim 1$ in the striped wind models (e.g., Komissarov 2013). Table 2.1 includes the values used in each flare model for the Lorentz factor of the injected electrons, $\gamma_0 = x_0$, and the particle injection rate, $\dot{N}_0$. The associated power in the injected particles is given by $L_0 = \gamma_0 m_e c^2 \dot{N}_0$, assuming isotropic emission. We confirm in each case that the injected power L_0 does not exceed the pulsar spin-down power, which is $\sim 5 \times 10^{38}\,{\rm ergs\,s^{-1}}$. In general, we set $\gamma_0 = 10^6$ in order to simulate the effect of the injection of electrons from the "cold" pulsar wind, in which the electrons have a high bulk Lorentz factor but a small random component (Lyubarsky 2003). However, in the case of the 2013 March flare, we find it necessary to set $\gamma_0 = 5 \times 10^8$ in order to avoid an injection power L_0 that exceeds the spin-down power. The value $\gamma_0 = 5 \times 10^8$ is much higher than expected for the cold pulsar wind, but it is in the expected range if one considers the absorption of the electromagnetic Poynting flux by the electrons near the termination shock, leading to a "hot" input distribution rather than a cold one (Rees & Gunn 1974). This is essentially the scenario considered by Cerutti et al. (2103b), who assumed that the injected electrons were sampled from an ultrarelativistic Maxwellian distribution with temperature

$kT/(m_e c^2) = 10^8$. Similarly, Cerutti et al. (2013a) assumed the injection of a power-law electron distribution extending up to a maximum Lorentz factor equal to 4×10^8.

4.4.5 Synchrotron Afterglow

Although the γ-ray flares observed from the Crab nebula are intrinsically time-dependent phenomenon, in this paper, we have employed a steady-state approach to model the underlying electron distribution, under the assumption that the electrons reach equilibrium during the peak of the flare. This is reasonable provided the flare duration timescale is comparable to the synchrotron loss timescale, which is in fact the case, according to Equation (4.6). In our one-zone model, the electrons that create the observed γ-ray synchrotron flares are accelerated and radiate in the same region, which is in the vicinity of the pulsar wind termination shock.

The electrons that produce the peak level of γ-ray emission observed during a given flare eventually escape into the downstream (outer) region, at radius $r > r_t$, where $r_t = 10^{17}$ cm is the pulsar wind termination shock radius. The escape of the electrons into the outer region of the nebula occurs via a combination of advection for the low-energy electrons that are "trapped" in the outflow, and Bohm diffusion for the high-energy electrons. The transition between these two escape channels occurs at the cross-over Lorentz factor, $\gamma_c \sim 10^{10} - 10^{11}$ (see Equation (4.38) and Table 2.1).

Once the electrons escape, they are subject to continued synchrotron cooling in the outer region of the nebula, but they do not experience any additional acceleration. Since this is a non-equilibrium situation, the synchrotron spectrum emitted by the cooling electrons varies with time, and therefore the electrons in the cooling region produce a variable "synchrotron afterglow" spectrum that gradually fades away and shifts to lower frequencies. We can use our model to compute the time-dependent synchrotron afterglow spectrum, and to make predictions that can be compared with multi-wavelength observations of future γ-ray flares from the Crab nebula.

The transport equation for the escaping electrons in the cooling region is quite simple, since they only experience losses. Here, we will focus solely on the synchrotron losses, in order to obtain an upper limit on the afterglow radiation. If adiabatic losses are also taken into consideration, that will reduce the level of the resulting spectrum below that predicted here. As an escaping electron cools in response to synchrotron losses, its Lorentz factor γ varies according to (see Equation (4.4))

$$-\frac{1}{\gamma^2}\frac{d\gamma}{dt} = \frac{\sigma_{\rm T} B_{\rm cool}^2}{6\pi m_e c} \ , \tag{4.96}$$

where $B_{\rm cool}$ is the magnetic field in the cooling region. We can rewrite Equation (4.96) as

$$-\frac{d\gamma}{\gamma^2} = \mathscr{B}_0 dt \ , \tag{4.97}$$

where the constant $\mathscr{B}_0 \propto {\rm s}^{-1}$ is given by (cf. Equation (4.18))

$$\mathscr{B}_0 = \frac{\sigma_{\rm T} B_{\rm cool}^2}{6\pi m_e c} \ . \tag{4.98}$$

The solution obtained for the time variation of the Lorentz factor is

$$\gamma(\gamma_*, t) = \left(\frac{1}{\gamma_*} + \mathscr{B}_0 t\right)^{-1} \ , \tag{4.99}$$

where γ_* is the initial value of the electron's Lorentz factor at time $t = 0$ as it enters the downstream cooling region and begins the cooling phase of its evolution in the nebula. The initial Lorentz factor γ_* can be computed in terms of the Lorentz factor γ at time t by inverting Equation (4.99) to obtain

$$\gamma_*(\gamma, t) = \left(\frac{1}{\gamma} - \mathscr{B}_0 t\right)^{-1} \ . \tag{4.100}$$

This result implies that the maximum possible Lorentz factor at time t is equal to $1/(\mathscr{B}_0 t)$.

The time-dependent electron distribution in the cooling region, denoted by $\mathscr{N}_{\rm G}(t,\gamma)$, evolves under the influence of synchrotron losses according to the relation

$$\mathscr{N}_{\rm G}(t,\gamma) = J(t)\,\mathscr{N}_{\rm G}(0,\gamma_*) \ , \tag{4.101}$$

where $\mathscr{N}_{\rm G}(0,\gamma_*)$ is the initial distribution at time $t=0$, and the normalization function $J(t)$ can be determined by requiring that the total number of electrons is conserved during the cooling phase. Conservation of electron number during the cooling phase implies the differential relation

$$\mathscr{N}_{\rm G}(t,\gamma)\,d\gamma = \mathscr{N}_{\rm G}(0,\gamma_*)\,d\gamma_* \ , \tag{4.102}$$

or, equivalently,

$$\mathscr{N}_{\rm G}(t,\gamma) = \mathscr{N}_{\rm G}(0,\gamma_*)\left(\frac{\partial\gamma_*}{\partial\gamma}\right)_t \ , \tag{4.103}$$

where γ_* is computed using Equation (4.100). The required partial derivative is given by

$$J(t) \equiv \left(\frac{\partial\gamma_*}{\partial\gamma}\right)_t = \frac{\gamma_*^2}{\gamma^2} \ . \tag{4.104}$$

By combining this result with Equation (4.101), we find that the electron distribution in the cooling region after time t is related to the electron distribution at time $t=0$ using

$$\mathscr{N}_{\rm G}(t,\gamma) = \gamma^{-2}\left(\frac{1}{\gamma}-\mathscr{B}_0 t\right)^{-2}\mathscr{N}_{\rm G}\left[0,\left(\frac{1}{\gamma}-\mathscr{B}_0 t\right)^{-1}\right] \ , \tag{4.105}$$

where the value of γ at time t cannot exceed the limit $\gamma < 1/(\mathscr{B}_0 t)$.

Equation (4.105) relates the electron distribution $\mathscr{N}_{\rm G}(t,\gamma)$ in the cooling region to the starting distribution $\mathscr{N}_{\rm G}(0,\gamma)$ at time $t=0$. Our remaining task is to compute the initial distribution at $t = 0$. This can be accomplished by recognizing that the initial distribution in the downstream cooling region is equal to the population of electrons that escapes from the acceleration region. Hence we can write

$$\mathscr{N}_{\rm G}(0,\gamma) = t_* \, N_{\rm G}(\gamma,\gamma_0) \, t_{\rm esc}^{-1}(\gamma) \ , \tag{4.106}$$

where γ_0 is the Lorentz factor of the monoenergetic electrons injected into the acceleration region, the acceleration-region particle distribution $N_{\rm G}$ is computed using Equation (4.58), and t_* is the timescale for electrons to accumulate in the downstream cooling region, before advection sweeps them into the outer part of the nebula. The advection timescale is independent of the particle energy. In our application to the Crab nebula, we set t_* equal to 7 days since this is the approximate flare duration. The escape timescale, $t_{\rm esc}(\gamma)$, appearing in Equation (4.106) is given by (see Equation (4.37))

$$t_{\rm esc}(\gamma) = \left(\frac{C_0}{\gamma} + F_0\gamma\right)^{-1} \ , \tag{4.107}$$

which exhibits the variation between shock-regulated escape at low particle energies and Bohm diffusive escape at high particle energies (see Section 4.2.5). The transition between the two escape mechanism occurs at the cross-over Lorentz factor, γ_c, computed using Equation (4.38). In our models, we find that $\gamma_c \sim 10^{10} - 10^{11}$ (see Table 2.1).

By combining Equations (4.105), (4.106), and (4.107), we find that the advanced-time electron distribution in the cooling region can be written in the explicit form

$$\mathscr{N}_{\rm G}(t,\gamma) = \left(\frac{1}{\gamma} - \mathscr{B}_0 t\right)^{-3} t_* \, \gamma^{-2} \left[C_0 \left(\frac{1}{\gamma} - \mathscr{B}_0 t\right)^2 + F_0\right] N_{\rm G}\left[\left(\frac{1}{\gamma} - \mathscr{B}_0 t\right)^{-1}, \gamma_0\right] \ , \tag{4.108}$$

where $N_{\rm G}$ is computed using Equation (4.58). The synchrotron afterglow spectrum generated at time t by the population of electrons that have escaped into the downstream (cooling) region is computed using (see Equation (4.72))

$$\mathscr{F}_\nu^{\rm cool}(t,\nu) = \frac{1}{4\pi D^2}\int_1^{(\mathscr{B}_0 t)^{-1}} \mathscr{N}_{\rm G}(t,\gamma)P_\nu(\nu,\gamma)d\gamma \ \propto \ {\rm erg\ s^{-1}\ cm^{-2}\ Hz^{-1}}\ , \qquad (4.109)$$

where D is the distance to the source, $\mathscr{N}_{\rm G}$ is evaluated using Equation (4.108), and $P_\nu(\nu,\gamma)$ is given by Equation (4.68). Note that the upper bound for the integration over γ at time t is equal to $(\mathscr{B}_0 t)^{-1}$ due to the action of synchrotron cooling.

In Figure 4.5 we plot the synchrotron afterglow spectrum for the flares calculated using Equation (4.109), and varying the accumulation timescale value t_* until the flux magnitude of the afterglow immediately after the flare equals that of the flare spectrum. This is a temporal continuity condition that we apply which allows t_* to vary. The spectrum is plotted as a series of "snapshots" at times $t = 1\,$s, $t = 9\,$days, and $t = 21\,$days. The magnetic field strength in the downstream (cooling) region, $B_{\rm cool}$, is likely to be lower than that in the upstream acceleration region, B, so that $B_{\rm cool} \le B$. In Figure 4.5, we have set $B_{\rm cool} = B = 200\,\mu$G, and we have also ignored the effect of adiabatic losses in the expanding wind. Hence, the spectral snapshots plotted in Figure 4.5 represent upper limits on the predicted level of the afterglow emission. It is clear that the synchrotron afterglow is not much less luminous than the primary γ-ray flare observed in 2011 April, even if the magnetic field in the cooling region has the relatively high value $B_{\rm cool} = 200\,\mu$G, in which case Figure 4.5 suggests that the afterglow may be detectable above the quiescent background for a period of at least 3 weeks. However, the levels of emission reported in Figure 4.5 will be reduced by adiabatic losses in the wind, and also by the decreasing magnetic field strength experienced by the electrons as they advect to larger radii in the wind and so our afterglow spectral snapshots represent the upper limit on the observable flux levels for each flare's afterglow.

4.4.6 Conservation of Energy

It is important to analyze the energy budget of the flare by computing the energy loss and gain rate for each term in the transport equation. The gains are the injection energy, shock and electrostatic acceleration, and the energy gain rate from stochastic wave-particle acceleration via interactions with MHD waves. The sum of these energy gain channels should be equal to the loss rate channels given by synchrotron losses and particle escape. We compute each one below and summarize the results in Tables 4.3 and 4.4.

The flares have a luminosity that is on the order of a few percent of the pulsar spin-down power which is a constraint that the model satisfies. However, it is instructive to compute the synchrotron energy loss rate due to the total electron population after being accelerated. We define the synchrotron power, $P_{\rm synch}$. We have,

$$P_{\rm synch} = \frac{4}{3}\sigma_{\rm T} c U_B \int_1^\infty N_{\rm G}(\gamma)\gamma^2 d\gamma \ , \tag{4.110}$$

where $N_{\rm G}$ is given by Equation (4.58) and U_B is the magnetic energy density. The value of $L_{\rm synch}$ should be about 1% the pulsar spin-down power.

Another energy loss channel is particle escape. The Bohm diffusive escape and shock-regulated escape scenarios both occur in the nebula and we must take into account both of these processes to get the total energy losses due to particle escape. The escaped particle power, $P_{\rm esc}$, is given by

$$P_{\rm esc} = \int_1^\infty (t_{\rm SRE}^{-1} + t_{\rm Bohm}^{-1})\gamma m_e c^2 N_{\rm G}(\gamma) d\gamma = \int_1^\infty \left(\frac{C_0}{\gamma} + F_0\gamma\right)\gamma m_e c^2 N_{\rm G}(\gamma) d\gamma \ , \tag{4.111}$$

where C_0 and F_0 are the escape rates for the shock-regulated and Bohm diffusive escape scenarios, respectively.

The energy gains due to electrostatic and shock acceleration are combined and the model parameter $\tilde{A}$ sets the strenght for the total first order energy gain rate. The stochastic MHD acceleration process is second order and so is treated separately. We have the power gained from first order acceleration processes, P_{elec}, given by

$$P_{\mathrm{elec}} = \int_1^\infty qEcN_{\mathrm{G}}(\gamma)d\gamma \ , \tag{4.112}$$

where E is the electric field. The energy gain rate due to only shock acceleration is given by

$$P_{\mathrm{shock}} = \int_1^\infty \frac{\rho qB}{\zeta} cN_{\mathrm{G}}(\gamma)d\gamma \ , \tag{4.113}$$

where ρ is the fractional shock efficiency, q is the charge of an electron, and ζ is of order unity. The energy gain rate due to only the stochastic MHD acceleration process, P_{MHD}, is given by

$$P_{\mathrm{MHD}} = \int_1^\infty 3D_0 m_e c^2 N_{\mathrm{G}}(\gamma)d\gamma \ , \tag{4.114}$$

where D_0 is given by the first case in Equation (4.93).

We can compute the power gain and loss contributions from each term in the transport equation and demonstrate that the total energy budget can be accounted for. Additionally, it will be insightful to connect the flare spectral shape with where most of the energy is being channeled. The magnitude of each channel is reported in Tables 4.3 and 4.4. The synchrotron loss column is seen to be $1 - 5\%$ of the pulsar spin-down power as expected.

Efficient Gamma-Ray Flares

The April 2011 and September 2007 flares are the most similar to each other than any other. This is to be expected since even the flare spectra have similar shapes and peak flux magnitudes. Additionally they each display particle distribution functions with peaks at very high Lorentz factors. Furthermore, these two flares have the highest values of $\tilde{A}$ and the lowest values of $\tilde{C}$ indicating that the accelerating region during these flares were characterized by very efficient conversion of magnetic energy to electrostatic fields. The low value of $\tilde{C}$ indicates that the nature of the termination shock was such that shock-regulated escape was very inefficient. This could be due to a change in the obliquity of the shock to the outflowing pulsar wind which increased the probability of additional shock crossings instead of shock-regulated escape for particles with low momentum. These shock-recycled particles could survive long enough at the termination shock to undergo additional electrostatic acceleration as well. The escaped particle power for these two flares have the smallest magnitude (by a factor of one hundred) as is seen in Table 4.4.

Inefficient Gamma-Ray Flares

The weakest flare on February 2009 displays a peak below the synchrotron burn-off limit and flux levels similar to that of the quiescent background emission. The values for the energy gain and loss rates reported in Tables 4.3 and 4.4 shows that the escaping power represents a significant fraction of all the energy gain rates. We note that $P_{\rm esc}$ for this flare is twice the pulsar spin-down power. There could be mild bulk boosting which could explain this. Additionally, the emission could be anisotropic yet in this model we assume isotropic emission. This implies that during this flare the accelerating mechanisms were weak and the escape mechanisms were very efficient. Most of the injected particles underwent insignificant acceleration and then escaped efficiently without further acceleration. Figure 4.3 shows $\gamma^2 N_G$ plots and it can be seen that the February 2009 flare spectrum resulted from the least amount of very high energy electrons as is seen by the fact that the peak occurs at the lowest values of γ.

The second weakest flare occured in September 2010. Table 4.4 shows that the escaping particle power is comparable to the energy gain rate due to electrostatic acceleration and shock acceleration. However, the fractional ($P_{\rm esc}$ compared with $P_{\rm gain}$) particle escape power is not as significantly high as it is in the February 2009 flare. Correspondingly, the flare spectrum for September 2010 has a peak slightly above or comparable to the synchrotron burn-off limit and displays flux levels sufficiently above background levels.

Lastly, the March 2013 flare has escaped particle power that is comparable to the two weakest flares, despite being characterized by significant flux above the synchrotron burn-off limit and being the most broad spectrum. Namely, the theoretical spectrum predicts γ-ray flux significantly above any other flare at energies in excess of that reported by the *Fermi* observational data. This flare is reproduced by the model with the largest induced electrostatic fields and the smallest dimensionless gain parameter $\tilde{A}$, but it has one of the largest values of $\tilde{C}$ meaning shock-regulated escape was efficient. This could imply a unique termination shock morphology which more efficiently ejects low momenta particles. We note that as the synchrotron afterglow fades in the synchrotron nebula the spectrum seems to approach the well-known quiescent spectrum of the nebula. This suggests that the electrons accelerated at the termination shock in our model may merge with the native electron population in the nebula.

4.5 Discussion

We have developed and applied a new analytical model for the acceleration and transport of relativistic electrons in pulsar wind termination shocks, including the effects of stochastic wave-particle acceleration, electrostatic acceleration, shock acceleration, particle escape, and radiative losses via the production of synchrotron emission. Since losses are included in our transport equation, the synchrotron flare γ-ray spectra that we obtain are self-consistent. The model considered here differs significantly from that developed by previous authors such as Cerutti et al. (2012, 2013a, 2014) in that we do not explicitly treat the spatial transport, and instead, we focus on a one-zone model in which the the electron energy distribution is interpreted as an average over the acceleration/emission region. However, the spatial geometry of the problem is treated implicitly through the utilization of a realistic dependence of the escape timescale, $t_{\rm esc}$, on the particle momentum, p, expressed by Equation (4.37). At low energies, the electrons are trapped in the flow, and the escape of the particles is regulated by advection in the vicinity of the shock; at high energies, the particles are able to escape into the outer region of the nebula because the Larmor radius becomes comparable to the termination shock radius, $r_t = 10^{17}\,\mathrm{cm}$. The transition between the dominance of the two escape mehanisms occurs at the cross-over Lorentz factor, γ_c (Equation (4.38)), and the highest-energy electrons accelerated in our model reach a peak Lorentz factor of $\sim 10^{10}$, which is consistent with the Hillas condition for the Crab nebula termination shock radius $r_t \sim 10^{17}\,\mathrm{cm}$ (see Equation (4.35)).

In the model of Cerutti et al. (2012), the acceleration occurs in a thin layer of magnetic reconnection, and the electrons leave that region as a tightly focused beam, to enter a separate radiation region where the electrons generate synchrotron emission in the presence of a stronger magnetic field than that in the acceleration region. While this scenario is plausible, it relies on two assumptions that may not be warranted. The first assumption is that the acceleration occurs in a region of greatly suppressed magnetic field, where the field strength is far below the observed ambient value. The second assumption is the imposition of a magnetic guide field, which is required in order to render the simulations stable, so that the electrons can reach the energies required to explain the observed γ-ray emission. Furthermore, the γ-ray spectra obtained by Cerutti et al. (2012) do not fit the observed γ-ray spectra very well. We demonstrated in Figure 4.2 that the model developed here is able to fit reasonably well the γ-ray spectra for all five of the γ-ray flares from the Crab nebula observed by *Fermi*-LAT and *AGILE*, up to photon energies of $\sim 1\,\mathrm{GeV}$. We have also reported computations of the synchrotron afterglow emission produced by the accelerated electrons after they escape into the downstream (outer) cooling region in Figures 4.5. We predict that the afterglow should be observable for approximately 3 weeks, at a maximum. However, this estimate neglects the effects of adiabatic cooing and the decreasing magnetic field that the escaping particles will experience as that advect through the outer region of the pulsar wind nebula.

Table 4.1: Input Model Parameters

Flare	σ_{mag}	$\tilde{A}_{\mathrm{shock}}$	$\tilde{A}_{\mathrm{elec}}$	$\tilde{B}$	$\tilde{C}$	$\tilde{F}$
September 2007	0.0802	3.740	32.26	5.50×10^{-19}	10.0	2.89×10^{-21}
February 2009	0.0401	7.480	17.52	1.10×10^{-18}	45.0	1.16×10^{-20}
September 2010	0.0980	3.060	32.94	4.50×10^{-19}	53.0	1.94×10^{-21}
April 2011	0.1026	2.925	46.80	4.30×10^{-19}	15.0	1.77×10^{-21}
March 2013	0.6784	0.440	13.56	6.50×10^{-19}	40.0	4.04×10^{-23}

Table 4.2: Additional Parameters

Flare	m_{-}	$D_0(\mathrm{s}^{-1})$	$\frac{E}{B}$	γ_{c}	γ_0	$\dot{N}_0(\mathrm{s}^{-1})$
September 2007	-0.261	94.00	0.862	1.12×10^{11}	1×10^{6}	4.50×10^{33}
February 2009	-1.575	47.00	0.234	5.58×10^{10}	1×10^{6}	4.50×10^{38}
September 2010	-1.347	114.9	1.076	1.36×10^{11}	1×10^{6}	4.32×10^{37}
April 2011	-0.288	120.2	1.600	9.21×10^{10}	1×10^{6}	8.10×10^{33}
March 2013	-2.198	795.4	3.065	5.89×10^{11}	5×10^{8}	8.00×10^{35}

Table 4.3: Energy Budget: Gains

Flare	$L_0(\mathrm{ergs\,s^{-1}})$	$P_{\mathrm{elec}}(\mathrm{ergs\,s^{-1}})$	$P_{\mathrm{shock}}(\mathrm{ergs\,s^{-1}})$	$P_{\mathrm{MHD}}(\mathrm{ergs\,s^{-1}})$
September 2007	3.68×10^{33}	5.54×10^{36}	6.44×10^{35}	1.08×10^{36}
February 2009	3.68×10^{38}	3.69×10^{38}	1.58×10^{38}	6.34×10^{37}
September 2010	4.91×10^{37}	1.10×10^{38}	1.02×10^{37}	1.01×10^{37}
April 2011	6.63×10^{33}	1.02×10^{37}	6.39×10^{35}	1.29×10^{36}
March 2013	3.28×10^{38}	1.89×10^{38}	6.17×10^{36}	4.21×10^{37}

Table 4.4: Energy Budget: Losses

Flare	$P_{\mathrm{synch}}(\mathrm{ergs\,s^{-1}})$	$P_{\mathrm{esc}}(\mathrm{ergs\,s^{-1}})$
September 2007	1.04×10^{37}	3.66×10^{36}
February 2009	2.25×10^{36}	9.51×10^{38}
September 2010	1.75×10^{36}	1.78×10^{38}
April 2011	1.62×10^{37}	6.52×10^{36}
March 2013	3.24×10^{36}	5.61×10^{38}

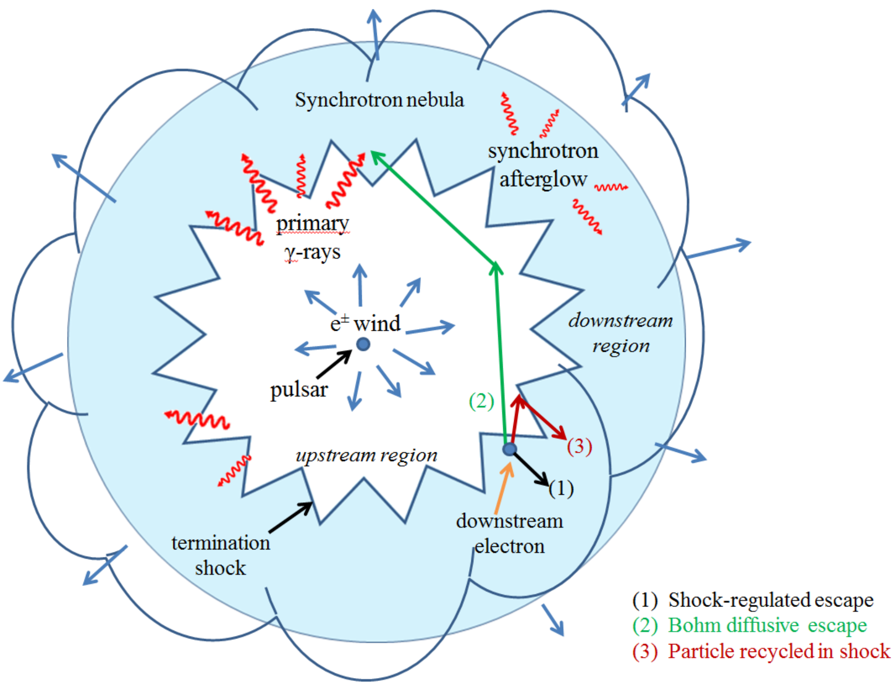

Figure 4.1: Diagram summarizing the geometry of the pulsar wind termination shock and the associated particle acceleration and transport.

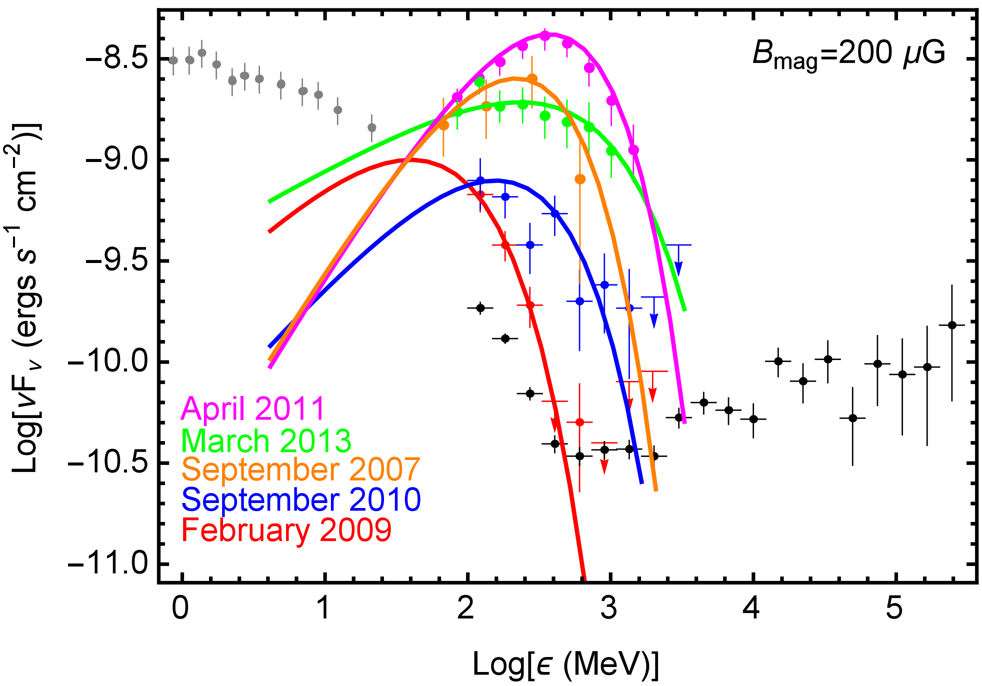

Figure 4.2: Gamma-ray synchrotron flare spectra computed using Equation (4.72) are plotted using the parameters listed in Tables 4.1 and 4.2 (solid lines). The associated electron distributions are computed using Equation (4.58). Also plotted are the corresponding data for each of the γ-ray flares observed by *Fermi*-LAT and *AGILE*, taken from Abdo et al. (2011), Buehler et al. (2012), and Buehler & Blandford (2014).

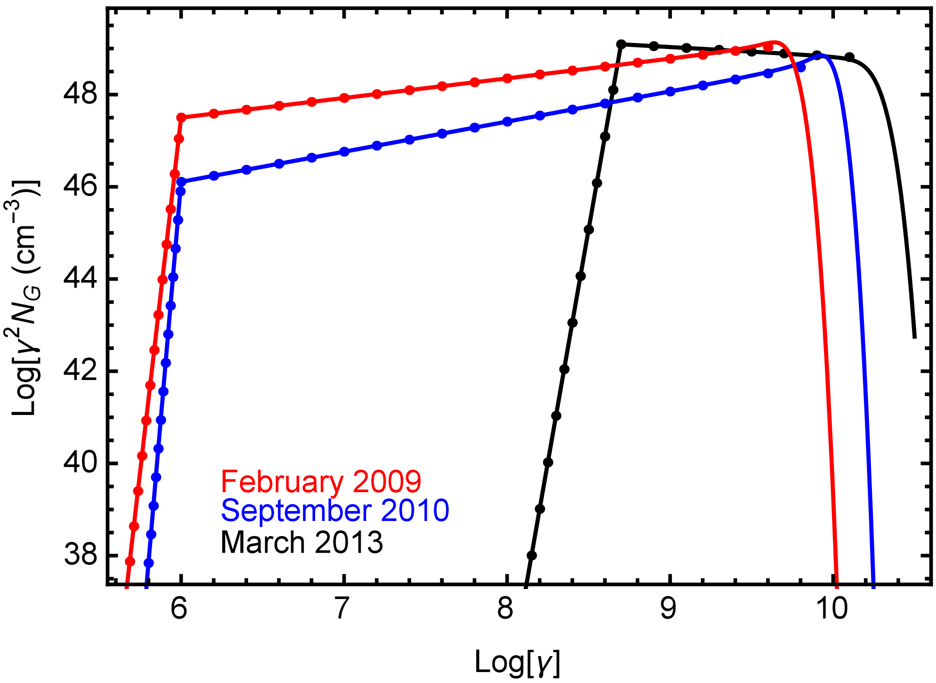

Figure 4.3: The electron number distributions given by the exact solution (Equation (4.58), solid lines) are compared with the approximate broken power-law solution (Equation (4.64), filled circles). Here we consider the electron distributions for the 2009 February, 2010 September, and 2013 March flares, which agree closely with the corresponding power-law distributions up to the exponential turnover created by synchrotron losses.

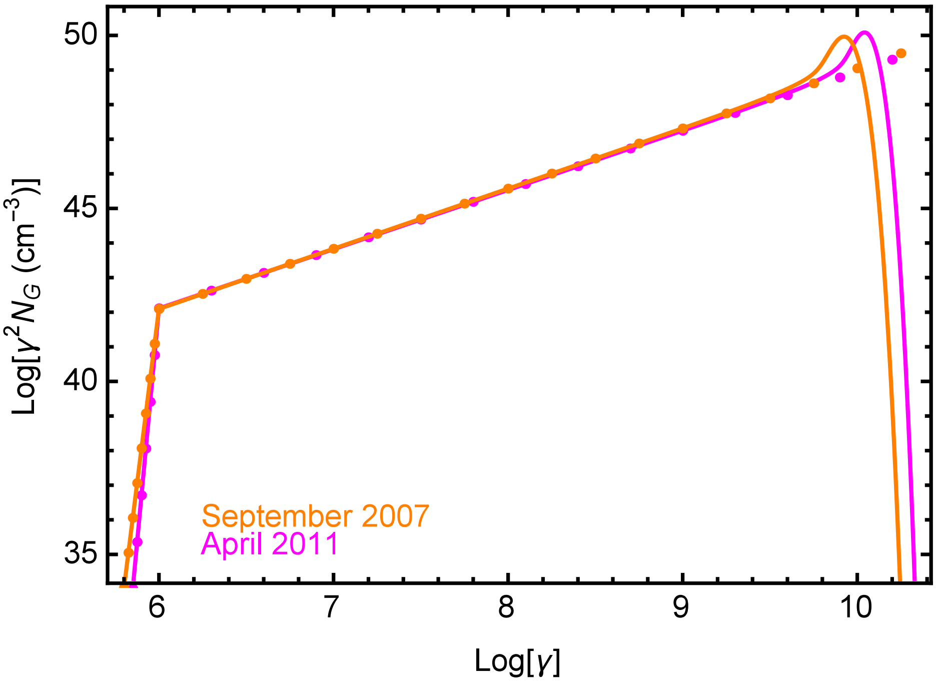

Figure 4.4: Same as Figure 4.3, except here we plot the electron distributions corresponding to the 2011 April and 2007 September flares. In these two cases, a distinctive particle pile-up occurs at the energy where synchrotron losses produce an exponential turnover. At lower energies, the exact solutions agree with the approximate power-law solution given by Equation (4.64).

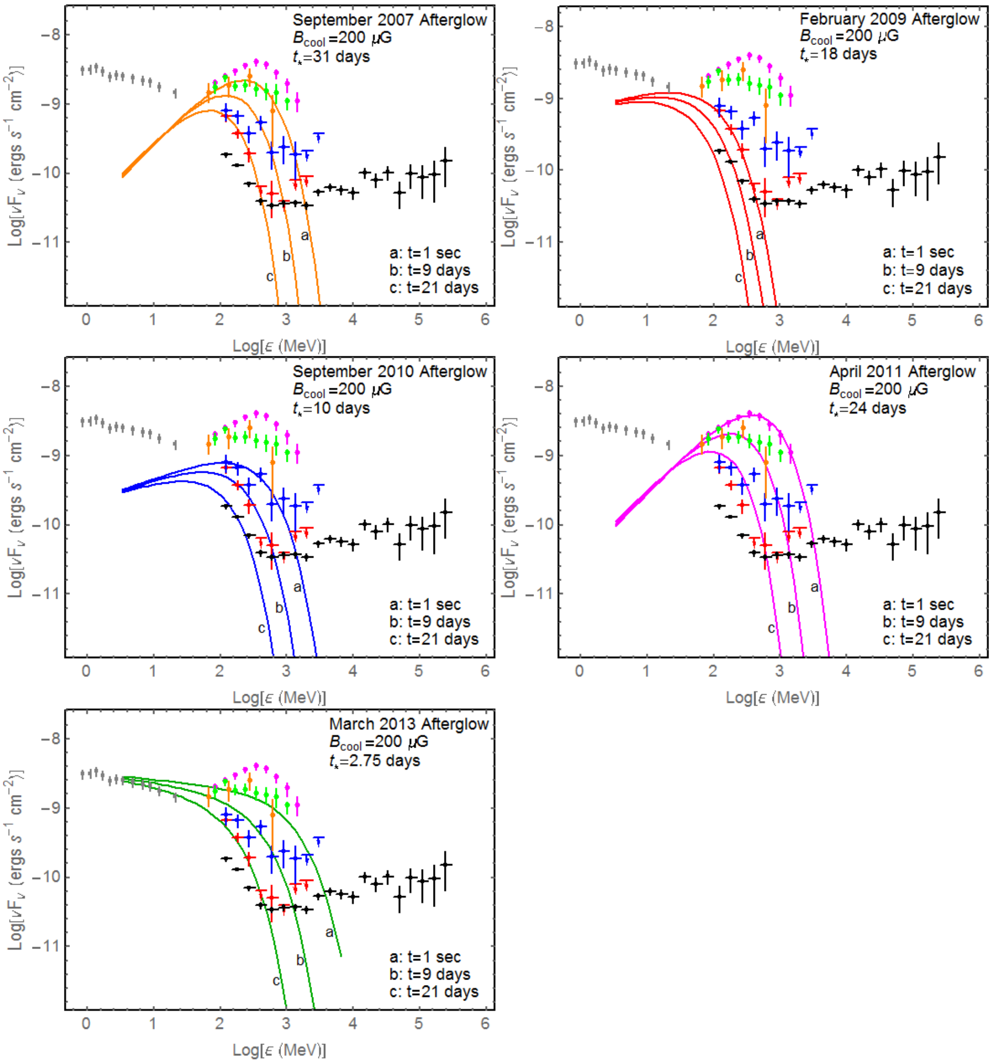

Figure 4.5: Synchrotron afterglow spectra computed using Equation (4.109) for the flares are plotted along with the *Fermi*-LAT and *AGILE* data for all of the flares, as well as the quiescent emission. Here we set the magnetic field in the cooling region on the downstream (outer) side of the pulsar wind termination shock equal to $B_{\rm cool} = 200\,\mu$G as an upper limit. We also vary the particle accumulation timescale t_* which is also an upper limit based on flux continuity between the flare and the instant the cooling spectrum begins. Adiabatic losses in the expanding wind have been neglected. Under these assumptions, the afterglow would be detectable above the quiescent emission for about 3 weeks depending on the flare.

Chapter 5: Conclusions

In this dissertation I have developed analytic models describing a variety of high-energy astrophysical phenomenon for which there is a wealth of observational data. These models were tested by comparison with the data and the validity of the underlying assumptions that compose them were evaluated. The convenience and versatility of developing analytic models stems from the explicit control of the model parameters as well as the potential for the models to be ported into standard data analysis software. Furthermore, this dissertation research represents a significant improvement in the current understanding of several processes of interest in modern high-energy astrophysics. In the remaining sections I summarize the detailed conclusions reached in the two major projects that I have focused on in this dissertation.

5.1 X-Ray Time Lags and Spectra

Our goal in Chapter 2 was to develop an integrated model, based on the diffusion and thermal Comptonization of seed photons in an optically thick scattering cloud, that can naturally reproduce both the observed X-ray spectra and the time lags for Cyg X-1 and GX 339-04 using a single set of cloud parameters (density, radius, temperature). We have derived and presented a new set of exact mathematical solutions describing the Comptonization of seed photons injected into a scattering cloud of finite size that is either homogeneous, or possesses an electron number density that varies with radius as $n_e(r) \propto r^{-1}$. The results developed there include new expressions for (a) the Green's function describing the radiated quiescent X-ray flux (corresponding to the reprocessing of continually injected monochromatic seed photons), (b) the Green's function for the Fourier transform of the time-dependent radiation spectrum resulting from the impulsive injection of monochromatic seed photons, and (c) the associated X-ray Fourier time lags.

By exploiting the linearity of the fundamental transport equation, we used our results for the Green's function to explore a variety of seed photon injection scenarios. One of our main conclusions is that the integrated model can successfully explain the data regardless of the cloud configuration (homogeneous or inhomogeneous), provided the optical thickness and the temperature are comparable in the two models, as expected based on the Compton reverberation scenario (Payne 1980). Our results demonstrate that the bremsstrahlung injection model fits the observational time-lag data reasonably well for both Cyg X-1 and GX 339-04, whether the scattering corona is homogeneous or inhomogeneous. We therefore conclude that the constant time lags found by HKC in the homogeneous cloud configuration were the result of their utilization of a quasi-monochromatic (low-temperature blackbody) injection spectrum for the seed photon distribution.

The injection location in our model is different from that considerd by HKC, who assumed that the seed photons were always injected at the center of the spherical cloud. In our model, the injection location is arbitrary, and we find that the best agreement with the time lag data is obtained when the injection is relatively close to the surface of the cloud, so that the prompt escape of some of the unprocessed bremsstrahlung seed photons is able to explain the diminishing time lags observed at high Fourier frequencies. At longer timescales, the standard thermal Comptonization process sets the delay between the soft and hard channels, and this naturally leads to the observed plateau in the time lags at low Fourier frequencies.

In Chapter 3 we developed a fully relativistic time lag model based off of the same Comptonization processes studied in Chapter 2, but with the addition of a uniform rotation component. We found that the time lags in the rotating cloud model are frame-dependent lending, in part, to the Lorentz transformations of the relevant variables (e.g. Fourier frequency, energy, etc.). We implemented the same injection paradigm in this rotating cloud model whereby seed photons are injected on the surface of the homogeneous cloud and with a broadband injection spectrum due to a bremsstrahlung flash. We found that the resulting theoretical time lags reproduce the observational data just as well as the non-rotating cloud model provided the rotation angular velocity is the Keplerian rotation rate. In fact, we found that the rotating cloud model agrees exactly with the non-rotating cloud model indicating that any bulk rotation of coronae does not modify the resulting time lags, provided the rotation is Keplerian.

As an academic demonstration, we produce plots of the time lags produced from a homogeneous cloud when the rotation is super-Keplerian yet without regard to the mechanism driving such rapid rotation rates. It was interesting to see deviations from the non-rotating case at high Fourier frequency. Additionally, we saw different behavior in the Fourier frequency regimes between the sources Cyg X-1 and GX 339-04. Namely, the Cyg X-1 super-Keplerian model showed longer lags at high Fourier frequency than the non-rotating model and the reverse was true for GX 339-04 for the same rotation rates. It is likely that these deviations from the "base-line" time lags (i.e. the non-rotating model) result from significant boosting of the radiated flux emanating from the surface of a relativistically rotating cloud.

In future work, we plan to develop a more general Green's function in which the injection occurs on a ring or a point, rather than on a spherical shell as in the model considered here. As in the presesent study, the resulting Fourier transform of the time-dependent Green's function in the general case will allow us to investigate a variety of seed photon energy distributions (e.g., blackbody or bremsstrahlung). The additional geometric flexibility in the general model should allow us to further improve the agreement between the model predictions and the data, hence providing new insights into the structure of the scattering corona and the underlying accretion disk. We also plan to examine scenarios in which the electrons cool during the transient in response to the upscattering of the injected photons. This may help to explain the soft time lags observed in some accreting black-hole sources (e.g., Fabian et al. 2009).

5.2 Gamma-Ray Flares from the Crab Nebula

The model developed to quantitatively reproduce the γ-ray flare spectra from the Crab nebula represents a first ever fully analytic and self-consistent model which incorporates a wide range of relevant physics likely at work in the accelerating region of the Crab. The fits to the observational data are excellent and will allow future studies to glean information surrounding the nuances of the high-environment in the Crab near the termination shock.

Although transients are, by definition, a time-dependent phenomenon their spectra are time-averaged and can be studied using a time-independent model as was done in the γ-ray flare model developed in Chapter 4. The electron distribution function resulting from a variety of gains and losses is computed self-consistently, because the transport equation includes synchrotron losses as well as particle escape formalisms at high and low momenta. With the analytic solution for the particle distribution function resulting from acceleration, synchrotron losses, and escape we computed the exact synchrotron spectrum via a synchrotron convolution integral.

With explicit control over the model parameters that determine the relative contribution of each physical process (i.e. acceleration, losses, escape) we can produce unique fits to the observational data and draw conclusions from the parameter values that produce the fits. Furthermore, this model was capable of fitting the spectra of all the major super-flares thereby lending confidence to the model. We found that the electrostatic acceleration mechanism from the magnetic reconnection zone dominates over the relativistic shock acceleration mechanism.

Lastly, we provided a physical picture to constrain the size of the accelerating region by application of a dual escape formalism that includes Bohm diffusive escape and shock-regulated escape. The former describes high energy particles that escape from the system when their Larmor radius is large and approaches the size of the accelerating region. This is quantified through the Hillas condition. On the other hand, shock-regulated escape describes low-energy particles whose Larmor radius is small so they have a small probability of being recycled back through the shock. Instead they advect downstream and leave the vicinity of the accelerating region. By including both of these escape scenarios, each of which operates at either high or low energies, we provide both a great fit to the observed flare spectra and a comprehensive physical model.

In addition to the application of the model to the flare spectra, we also provided predictions of the after-glow spectrum. As particles escape from the accelerating region and enter the expanding nebula they cool via synchrotron losses with no further acceleration. This population of electrons were found to emit synchrotron radiation above quiescent levels for up to three weeks. It would be interesting if future observational studies could look for such a signature in the weeks following a major flare event. This auxillary model component should provide an upper limit on the flux levels due its simplicity, for we have neglected adiabatic losses and have little information regarding the strength and nature of the magnetic field topology in this region.

The model developed for the Gamma-Ray Flare phenomenon in the Crab Nebula is analytical in nature, and therefore it provides a very flexible tool with which to conduct a broad range of parameter studies. It should be straight forward to port the model into any of the standard data analysis packages to perform quantitative fits, which we do not pursue in this dissertation. In future work, we intend to pursue a fully time-dependent solution, as well as the analysis of the spectrum resulting from the acceleration of an injected power-law distribution of electrons, rather than the monoenergetic injection considered here.

Appendix A:

A.1 Appendix A

In order to use the series expansions developed in Sections 3 and 4 to represent the Green's functions for the quiescent spectrum and for the Fourier transform of the time-dependent spectrum, it is necessary to establish the orthogonality of the various spatial eigenfunctions. In this section, we present a global proof of orthogonality of the spatial eigenfunctions for both the homogeneous case (utilizing the mirror inner boundary condition) and for the inhomogeneous case (utilizing the dual free-streaming boundary condition). First we define the generic spatial ODE, encompassing Equations (2.46), (2.69), (2.87), and (2.106), by writing

$$\frac{1}{z^{2-\alpha}} \frac{d}{dz} \left(z^{2+\alpha} \frac{d\Gamma_n}{dz} \right) + \eta^2 \xi_n \Gamma_n(z) = 0 \ , \tag{A.1}$$

such that,

$$\alpha = \begin{cases} 0, & \text{homogeneous (quiescent \& Fourier transform)} \ , \\ 1, & \text{inhomogeneous (quiescent \& Fourier transform)} \ , \end{cases} \tag{A.2}$$

$$\Gamma_n(z) = \begin{cases} Y_n(z), & \text{homogeneous (quiescent \& Fourier transform)} \ , \\ y_n(z), & \text{inhomogeneous (quiescent)} \ , \\ g_n(z), & \text{inhomogeneous (Fourier transform)} \ , \end{cases} \tag{A.3}$$

and

$$\xi_n = \begin{cases} \lambda_n, & \text{homogeneous (quiescent \& Fourier transform)} \ , \\ \lambda_n, & \text{inhomogeneous (quiescent)} \ , \\ \lambda_n + 3i\tilde{\omega}z, & \text{inhomogeneous (Fourier transform)} \ . \end{cases} \tag{A.4}$$

To establish orthogonality, we multiply Equation (A.1) by $\Gamma_m(z)$ and then duplicate it with the indices exchanged, after which we subtract the second equation from the first, yielding

$$\Gamma_m \frac{d}{dz}\left(z^{2+\alpha}\frac{d\Gamma_n}{dz}\right) - \Gamma_n \frac{d}{dz}\left(z^{2+\alpha}\frac{d\Gamma_m}{dz}\right) = -\eta^2 z^{2-\alpha}(\xi_n - \xi_m)\Gamma_n(z)\Gamma_m(z) \ . \tag{A.5}$$

Next, we integrate by parts with respect to z over the computational domain $z_{\rm in} \le z \le 1$ to obtain, after simplification,

$$\left(z^{2+\alpha}\Gamma_m\frac{d\Gamma_n}{dz} - z^{2+\alpha}\Gamma_n\frac{d\Gamma_m}{dz}\right)\Bigg|_{z_{\rm in}}^{1} = -\eta^2(\xi_n - \xi_m)\int_{z_{\rm in}}^{1} z^{2-\alpha}\Gamma_n(z)\Gamma_m(z)\, dz \ . \tag{A.6}$$

The left-hand side of Equation (A.6) needs to be evaluated separately for the homogeneous and inhomogeneous cases, since the spatial boundary conditions are different in the two situations. We consider each of these cases in turn below.

For the homogeneous cloud configuration, with $\alpha = 0$ and $z_{\rm in} = 0$, the inner and outer spatial boundary conditions can be written as (cf. Equations (2.51) and (2.53))

$$\lim_{z\to 0}\ z^2\,\frac{d\Gamma_n}{dz} = 0 \ , \qquad \lim_{z\to 1}\ \frac{1}{3\eta}\frac{d\Gamma_n}{dz} + \Gamma_n = 0 \ . \tag{A.7}$$

Likewise, in the inhomogeneous case, with $\alpha = 1$, we can express the inner and outer boundary conditions as (cf. Equations (2.92) and (2.94))

$$\lim_{z\to z_{\rm in}}\ \frac{z}{3\eta}\frac{d\Gamma_n}{dz} - \Gamma_n = 0 \ , \qquad \lim_{z\to 1}\ \frac{z}{3\eta}\frac{d\Gamma_n}{dz} + \Gamma_n = 0 \ . \tag{A.8}$$

Using either the homogeneous or inhomogeneous boundary conditions given by Equations (A.7) and (A.8), respectively, we find that the left-hand side of Equation (A.6) vanishes, which establishes the required orthogonality of the spatial eigenfunctions. The orthogonality condition can be written in general as

$$\int_{z_{\rm in}}^{1} z^{2-\alpha}\, \Gamma_n(z)\, \Gamma_m(z)\, dz = 0 \ , \qquad n \neq m \ . \tag{A.9}$$

A.2 Appendix B

As shown in Section 5, the particular solution for the Fourier transform in the case of bremsstrahlung, $F_{\rm brem}$, injection is given by the convolution (see Equation (2.128))

$$F_{\rm brem}(x, z, z_0, \tilde{\omega}) = \int_{x_{\rm abs}}^{\infty} F_{\rm G}(x, x_0, z, z_0, \tilde{\omega})\, A_0\, x_0^{-1} e^{-x_0} N_0^{-1}\, dx_0 \ , \tag{A.10}$$

where $x_{\rm abs}$ is the dimensionless self-absorption cutoff energy, the constant A_0 is given by Equation (2.127), and the Fourier transform Green's function, $F_{\rm G}$, is given by Equations (2.83) and (2.123) in the homogeneous and inhomogeneous cases, respectively. In general, we can write $F_{\rm G}$ in the generic form

$$F_{\rm G}(x, x_0, z, z_0, \tilde{\omega}) = N_0\, e^{(x_0 - x)/2} (x x_0)^{-2} \sum_{n=0}^{\infty} M_{2,\lambda}(x_{\rm min}) W_{2,\lambda}(x_{\rm max})\, \mathscr{A}_n(z, z_0, \tilde{\omega}) \ , \tag{A.11}$$

where $x_{\rm min} = \min(x, x_0)$, $x_{\rm max} = \max(x, x_0)$, and $\mathscr{A}_n$ is a composite function containing the expansion coefficients and the spatial eigenfunctions, given by

$$\mathscr{A}_n(z, z_0, \tilde{\omega}) = \frac{e^{i\tilde{\omega} p_0} \eta^3}{4\pi R^3 \Theta^4 (m_e c^2)^3} \begin{cases} \dfrac{\Gamma(\mu - 3/2) Y_n(z_0) Y_n(z)}{\Gamma(1 + 2\mu) \mathscr{I}_n} \ , & \text{homogeneous} \ , \\ \dfrac{\Gamma(\sigma - 3/2) g_n(z_0) g_n(z)}{\Gamma(1 + 2\sigma)\, \eta^3 \mathscr{K}_n} \ , & \text{inhomogeneous} \ . \end{cases} \tag{A.12}$$

In the homogeneous case, μ is computed using Equation (2.76), and in the inhomogeneous case, σ is computed using Equation (2.109). Combining Equations (A.10) and (A.11), and reversing the order of summation and integration, we obtain

$$F_{\rm brem}(x, z, z_0, \tilde{\omega}) = A_0 \, e^{-x/2} x^{-2} \sum_{n=0}^{\infty} \mathscr{A}_n(z, z_0, \tilde{\omega}) B(\lambda, x) \ , \tag{A.13}$$

where

$$B(\lambda, x) \equiv \int_{x_{\rm abs}}^{\infty} e^{-x_0/2} x_0^{-3} M_{2,\lambda}(x_{\rm min}) W_{2,\lambda}(x_{\rm max}) \, dx_0 \ , \tag{A.14}$$

and we set $\lambda = \mu$ to treat the homogeneous case, and we set $\lambda = \sigma$ to treat the inhomogeneous case.

Our remaining task is to evaluate the integral function B analytically, if possible. The expression for B can be broken into two integrals by writing, for $x \geq x_{\rm abs}$,

$$B(\lambda, x) = I_M(\lambda, x_0) \Big|_{x_{\rm abs}}^{x} W_{2,\lambda}(x) + I_W(\lambda, x_0) \Big|_{x}^{\infty} M_{2,\lambda}(x) \ , \tag{A.15}$$

and, for $x \leq x_{\rm abs}$,

$$B(\lambda, x) = I_W(\lambda, x_0) \Big|_{x_{\rm abs}}^{\infty} M_{2,\lambda}(x) \ , \tag{A.16}$$

where we have defined the indefinite integrals $I_M(\lambda, x_0)$ and $I_W(\lambda, x_0)$ using

$$I_M(\lambda, x_0) \equiv \int e^{-x_0/2} x_0^{-3} M_{2,\lambda}(x_0) dx_0 \, , \qquad I_W(\lambda, x_0) \equiv \int e^{-x_0/2} x_0^{-3} W_{2,\lambda}(x_0) dx_0 \ . \tag{A.17}$$

It is convenient to rewrite the Whittaker functions in the integrands for I_M and I_W using the Kummer function identities (Abramowitz & Stegun 1970),

$$M_{\alpha,\beta}(z) = e^{-z/2} z^{\frac{1}{2}+\beta} M\Big(\frac{1}{2} + \beta - \alpha, 1 + 2\beta, z\Big) \ , \tag{A.18}$$

$$W_{\alpha,\beta}(z) = e^{-z/2} z^{\frac{1}{2}+\beta} U\Big(\frac{1}{2} + \beta - \alpha, 1 + 2\beta, z\Big) \ , \tag{A.19}$$

which yield

$$I_M(\lambda, x) = \int e^{-x} x^{b-a-5} M(a, b, x) dx \ , \qquad I_W(\lambda, x) = \int e^{-x} x^{b-a-5} U(a, b, x) dx \ , \tag{A.20}$$

where

$$a = \lambda - \frac{3}{2} \ , \qquad b = 2\,\lambda + 1 \ . \tag{A.21}$$

The integral $I_W(\lambda, x)$ can be carried out analytically using Slater's (1960) identity,

$$\int e^{-x} x^{b-a-2} U(a, b, x) dx = -e^{-x} x^{b-a-1} U(a + 1, b, x) \ . \tag{A.22}$$

Integrating Equation (A.20) by parts once yields

$$\int x^{-3} e^{-x} x^{b-a-2} U(a, b, x) dx = -x^{-3} e^{-x} x^{b-a-1} U(a + 1, b, x) \\ - 3 \int x^{-4} e^{-x} x^{b-a-1} U(a + 1, b, x) dx \ . \tag{A.23}$$

Integrating by parts again gives

$$\int x^{-3}e^{-x}x^{b-a-2}U(a,b,x)dx = -x^{-3}e^{-x}x^{b-a-1}U(a+1,b,x)$$
$$-3\Big[-x^{-2}e^{-x}x^{b-a'-1}U(a'+1,b,x) - 2\int x^{-3}e^{-x}x^{b-a'-1}U(a'+1,b,x)dx\Big]\ , \quad \text{(A.24)}$$

where $a' = a+1$. Integrating by parts a third time yields

$$\int x^{-3}e^{-x}x^{b-a-2}U(a,b,x)dx = -x^{-3}e^{-x}x^{b-a-1}U(a+1,b,x)$$
$$-3\Big\{-x^{-2}e^{-x}x^{b-a'-1}U(a'+1,b,x) - 2\Big[-x^{-1}e^{-x}x^{b-a''-1}U(a''+1,b,x)$$
$$-\int x^{-2}e^{-x}x^{b-a''-1}U(a''+1,b,x)dx\Big]\Big\}\ , \quad \text{(A.25)}$$

where $a'' = a'+1$. The remaining integral can be evaluated directly using Equation (A.22) to obtain, after some algebra,

$$\int x^{-3}e^{-x}x^{b-a-2}U(a,b,x)dx = e^{-x}x^{b-a-4}\Big[-U(a+1,b,x)+3U(a+2,b,x)$$
$$-6U(a+3,b,x)+6U(a+4,b,x)\Big]\ . \quad \text{(A.26)}$$

By converting the Kummer functions to Whittaker functions, we obtain the final expression

$$I_W(\lambda,x) = e^{-x/2}x^{-2}\Big[-W_{1,\lambda}(x)+3W_{0,\lambda}(x)-6W_{-1,\lambda}(x)+6W_{-2,\lambda}(x)\Big]\ . \quad \text{(A.27)}$$

Likewise, the integral $I_M(\lambda,x)$ in Equation (A.20) can be evaluated using Slater's (1960) identity

$$\int e^{-x}x^{b-a-2}M(a,b,x)dx = \frac{e^{-x}x^{b-a-1}}{b-a-1}M(a+1,b,x)\ . \quad \text{(A.28)}$$

Following the same iterative procedure used to evaluate $I_W(\lambda, x)$, we eventually arrive at the result

$$I_M(\lambda, x) = \frac{e^{-x} x^{b-a-4}}{b-a-1} \Bigg(M(a+1, b, x) + \frac{3}{b-a-2} \Bigg\{ M(a+2, b, x)$$
$$+ \frac{2}{b-a-3} \Big[M(a+3, b, x) + \frac{1}{b-a-4} M(a+4, b, x) \Big] \Bigg\} \Bigg) \,, \quad \text{(A.29)}$$

which can be rewritten in terms of the Whittaker functions as

$$I_M(\lambda, x) = \frac{x^{-2} e^{-x/2}}{\lambda + \frac{3}{2}} \Bigg(M_{1,\lambda}(x) + \frac{3}{\lambda + \frac{1}{2}} \Bigg\{ M_{0,\lambda}(x) + \frac{2}{\lambda - \frac{1}{2}} \Big[M_{-1,\lambda}(x) + \frac{1}{\lambda - \frac{3}{2}} M_{-2,\lambda}(x) \Big] \Bigg\} \Bigg) \,. \tag{A.30}$$

Our final expression for the integral function $B(\lambda, x)$ is obtained by rewriting Equations (A.15) and (A.16) as

$$B(\lambda, x) = \begin{cases} W_{2,\lambda}(x)[I_M(\lambda, x) - I_M(\lambda, x_{\rm abs})] - M_{2,\lambda}(x) I_W(\lambda, x) \,, & x \ge x_{\rm abs} \,, \\ -M_{2,\lambda}(x) I_W(\lambda, x_{\rm abs}) \,, & x \le x_{\rm abs} \,, \end{cases} \tag{A.31}$$

where $I_W(\lambda, x)$ and $I_M(\lambda, x)$ are evaluated using Equations (A.27) and (A.30), respectively. We can now combine Equations (A.12) and (A.13) to express the bremsstrahlung injection Fourier transform $F_{\rm brem}$ as

$$F_{\rm brem}(x, z, z_0, \tilde{\omega}) = \frac{e^{i\tilde{\omega} p_0} \eta^3 A_0 \, e^{-x/2}}{4\pi R^3 \Theta^4 (m_e c^2)^3 x^2} \sum_{n=0}^{\infty} \begin{cases} \dfrac{\Gamma(\mu - 3/2) Y_n(z_0) Y_n(z)}{\Gamma(1 + 2\mu) \mathscr{I}_n} B(\mu, x), & \alpha = 0, \\ \dfrac{\Gamma(\sigma - 3/2) g_n(z_0) g_n(z)}{\Gamma(1 + 2\sigma) \, \eta^3 \mathscr{K}_n} B(\sigma, x), & \alpha = 1, \end{cases} \tag{A.32}$$

where $B(\mu, x)$ and $B(\sigma, x)$ are evaluated using Equation (A.31).

A.3 Appendix C

The time lags computed using the homogeneous and inhomogeneous models presented in Chapter 2 are based off the exact solution to the Fourier transformed transport equation. The solution is the Fourier transformed Green's function which is convolved with a bremsstrahlung source distribution which yields the Fourier transformed particular solution for a bremsstrahlung injection spectrum. We found that the observed dependence of the time lags on Fourier frequency cannot be reproduced with a monochromatic injection spectrum, but rather a broadband spectrum. This flash occurs near the outer edge of the corona.

The corona is modeled by a sphere of constant temperature with the black hole at the center. The corona is found to have a size on the order of 10^9 cm depending on which model and source. Obviously, this presents a large surface area through which radiated flux emanates. The success of the time lag model produced in Chapter 3 makes the assumption that there are no time lag effects introduced when considering propagation delays from different parts of the extended cloud surface. In this Appendix we will provide a proof showing this assumption to be correct.

We wish to obtain the Fourier transform of the signal flux at the detector by performing a transformation between reference frames of the cloud and the observer. The observed intrinsic occupation number, $f_{\rm obs}$, is related to the intrinsic occupation number in the reference frame of the source, $f_{\rm source}$, via

$$f_{\rm obs}(\epsilon, t_{\rm obs}) = f_{\rm source}(\epsilon, t_{\rm obs} - \frac{r}{c}) \tag{A.33}$$

where

$$t_{\rm source} = t_{\rm obs} - \frac{r}{c} \ , \tag{A.34}$$

and r is found from an application of the law of cosines. An emitting band has differential area given by

$$dA_{\rm band} = R^2 \sin\theta d\theta d\phi = 2\pi R^2 \sin\theta d\theta \ . \tag{A.35}$$

The observed flux at the detector is expressed differentially in terms of the observed intrinsic occupation number as

$$dg_{\rm obs}(\epsilon, t_{\rm obs}) \equiv \epsilon^2 c f_{\rm source}(\epsilon, t_{\rm source})\Big(\frac{1}{4\pi D^2}\Big) dA_{\rm band} \propto {\rm s^{-1}cm^{-2}erg^{-1}} \ . \tag{A.36}$$

By substituting Equation (A.34) into Equation (A.36) and integrating we obtain

$$g_{\rm obs}(\epsilon, t_{\rm obs}) = \epsilon^2 c\Big(\frac{R^2}{4\pi D^2}\Big)\int_0^{\pi/2} f_{\rm source}(\epsilon, t_{\rm obs} - \frac{r}{c}) 2\pi \sin\theta d\theta \ . \tag{A.37}$$

The standard Fourier transform is defined as,

$$\mathscr{G}(\epsilon, \omega) \equiv \int_{-\infty}^{\infty} e^{i\omega t_{\rm obs}} g_{\rm obs}(\epsilon, t_{\rm obs}) dt_{\rm obs} \ . \tag{A.38}$$

By applying (A.38) to (A.37) yields,

$$\mathscr{G}_{\rm obs}(\epsilon, \omega) = \epsilon^2 c \frac{R^2}{2D^2}\int_0^{\pi/2}\int_{-\infty}^{\infty} \sin\theta e^{i\omega t_{\rm obs}} f_{\rm source}(\epsilon, t_{\rm obs} - \frac{r}{c}) d\theta dt_{\rm obs} \ . \tag{A.39}$$

Next, let's substitute Equation (A.34) into the Equation (A.39) giving

$$\mathscr{G}_{\rm obs}(\epsilon, \omega) = \epsilon^2 c \frac{R^2}{2D^2}\int_0^{\pi/2}\int_{-\infty}^{\infty} \sin\theta e^{i\omega r/c} e^{i\omega t_{\rm source}} f_{\rm source}(\epsilon, t_{\rm source}) d\theta dt_{\rm source} \ . \tag{A.40}$$

According to the geometry of the figure and by simple application of the law of cosines we obtain the expression for r given by

$$r = \sqrt{R^2 + D^2 - 2DR\cos\theta}\ . \tag{A.41}$$

Substituting this result into Equation (A.40) gives

$$\mathscr{G}_{\rm obs}(\epsilon,\omega) = \epsilon^2 c \frac{R^2}{2D^2} \int_0^{\pi/2} \sin\theta e^{i\omega\sqrt{R^2+D^2-2DR\cos\theta}/c} d\theta \int_{-\infty}^{\infty} e^{i\omega t_{\rm source}} f_{\rm source}(\epsilon, t_{\rm source}) dt_{\rm source}\ . \tag{A.42}$$

Substituting the definition for the Fourier transform for $f_{\rm source}$ gives

$$\mathscr{G}_{\rm obs}(\epsilon,\omega) = \epsilon^2 c \mathscr{F}_{\rm source}(\epsilon,\omega) \frac{R^2}{2D^2} \int_0^{\pi/2} \sin\theta e^{i\omega\sqrt{R^2+D^2-2DR\cos\theta}/c} d\theta\ . \tag{A.43}$$

This can be written as

$$\mathscr{G}_{\rm obs}(\epsilon,\omega) = \frac{R^2}{2D^2} \epsilon^2 c \mathscr{F}_{\rm source}(\epsilon,\omega) H(\omega)\ , \tag{A.44}$$

where

$$H(\omega) \equiv \int_0^{\pi/2} \sin\theta e^{i\omega\sqrt{R^2+D^2-2DR\cos\theta}/c} d\theta\ , \tag{A.45}$$

Time Lag Set-up

We wish to prove that there are no time lags introduced from consideration of propagation delays from different parts of the cloud surface. If the cloud is static (not rotating), then the time lags can be computed from either the source frame or from an observer's frame. To show this we first define the complex cross spectrum, $\tilde{C}$ from van der Klis et al. (1987)

$$\tilde{C}(\omega) \equiv \mathscr{G}^*_{\rm obs}(\epsilon_s,\omega) \mathscr{G}_{\rm obs}(\epsilon_h,\omega)\ . \tag{A.46}$$

The phase lags are given by taking the argument of this cross spectrum. The time lags are computed by dividing the phase lag by the corresponding frequency given by

$$\delta t = \frac{\mathrm{Arg}(\tilde{C}(\omega))}{\omega} \ . \tag{A.47}$$

We can rewrite Equation (A.46) by substituting in Equation (A.44) giving

$$\tilde{C}(\omega) = \left(\frac{R^2}{2D^2} \epsilon_s^2 c \mathscr{F}^*_{\mathrm{source}}(\epsilon_s, \omega) H^*(\omega) \right) \left(\frac{R^2}{2D^2} \epsilon_h^2 c \mathscr{F}_{\mathrm{source}}(\epsilon_h, \omega) H(\omega) \right) \ , \tag{A.48}$$

which can be rearranged to obtain

$$\tilde{C}(\omega) = \left(\frac{R^2}{2D^2} \right)^2 \epsilon_s^2 \epsilon_h^2 c^2 |H(\omega)|^2 \mathscr{F}^*_{\mathrm{source}}(\epsilon_s, \omega) \mathscr{F}_{\mathrm{source}}(\epsilon_h, \omega) \ . \tag{A.49}$$

We define the complex cross spectrum at the surface of the cloud

$$\tilde{C}_{\mathrm{source}}(\omega) \equiv \mathscr{F}^*_{\mathrm{source}}(\epsilon_s, \omega) \mathscr{F}_{\mathrm{source}}(\epsilon_h, \omega) \ , \tag{A.50}$$

which can be substituted back into Equation (A.50) giving

$$\tilde{C}(\omega) = \left(\frac{R^2}{2D^2} \right)^2 \epsilon_s^2 \epsilon_h^2 c^2 |H(\omega)|^2 \tilde{C}_{\mathrm{source}}(\omega) \ . \tag{A.51}$$

Since the multiplier on the right hand side is a real number, we find that the observed time lag is given by

$$\delta t = \frac{\mathrm{Arg}(\tilde{C}(\omega))}{\omega} = \frac{\mathrm{Arg}(\tilde{C}_{\mathrm{source}}(\omega))}{\omega} = \delta t_{\mathrm{source}} \ . \tag{A.52}$$

Hence the observed time lags are not influenced by light propagation delays across the surface of the non-rotating cloud.

References

Abdo, A., et al. 2011, Science, 331, 739

Abramowitz, M., & Stegun, I. A. 1970, Handbook of Mathematical Functions, (New York: Dover)

Achterberg, A., et al. 2001, MNRAS, 328, 393

Aharonian, F., et al. 2004, ApJ, 614, 897

Becker, P. A., & Begelman, M. C. 1986, ApJ, 310, 534

Becker, P. A., 2003, MNRAS, 343, 215

Becker, P. A., Le, T., & Dermer, C. D. 2006, ApJ, 647, 539

Begelman, M.C. 1979, MNRAS, 187, 237

Begelman, M.C. & Meier, D.L. 1982, ApJ, 253, 873

Bianchi, S., Maiolino, R., Risaliti, G., 2012, Ad. Ast., 2012

Buehler, B., & Blandford, R. 2014, RPPh, 77, 66901

Buehler, B., Scargle, J. D., et al. 2012, ApJ, 749, 26

Cadolle Bel, M., Sizun, P., Goldwurm, A., et al. 2006, A&A, 446, 591

Cadolle Bel, M., Rodriguez, J., D'Avanzo, P., et al. 2011, A&A, 534, 119

Cassatella. P., Uttley, P., Wilms, J., & Poutanen, J. 2012, MNRAS, 422, 2407

Cerutti, B., Uzdensky, D. A., & Begelman, M.C. 2012, ApJ, 746,148

Cerutti, B., Werner, G. R., Uzdensky, D. A., & Begelman, M. C. 2013a, ApJ, 770, 147

Cerutti, B., Werner, G. R., Uzdensky, D. A., & Begelman, M. C. 2013b, arXiv:1401.3016 [astro-ph.HE]

Cerutti, B., Werner, G. R., et al. 2014, ApJ, 782, 104

Corbel, S., Brocksopp, C., Tzioumis, A. K. 2013, MNRAS, 428, 2500

De Marco, B., et al. 2013, MNRAS, 431, 2441

Dermer, C. D., & Menon, G. 2009, High Energy Radiation from Black Holes: Gamma Rays, Cosmic Rays, and Neutrinos (Princeton, NJ: Princeton Univ. Press)

Dermer, C. D., Miller, J. A., & Li, H. 1996, ApJ, 456, 106

Done, C., Gierliński, M. 2005, MNRAS, 364, 208

Eardley, D.M., Lightman, A.P., Shapiro, S.L. 1975, ApJL, 199, L153

Esin, A.A., McClintock, J.E., Narayan, R. 1997, ApJ, 489, 865

Fabian, A.C., et al., 2009, Nature, 459, 540

Falcke, H., Kórding, E., Markoff, S. 2004, A&A, 414, 895

Fender, R.P., Belloni, T. 2004, Annu. Rev. Astron. Astrophys., 42, 317

Fender, R.P. Stirling, A.M., Spencer, R.E., et al. 2006, MNRAS, 369, 603

Gallant, Y. A., & Achterberg, A. 1999, MNRAS, 305, L6

Hester, J.J. 2008, Annu. Rev. Astron. Astrophys., 46, 127-55

Hillas, A. M. 1984, ARA&A, 22, 425

Hua, X.-M., Kazanas, D., & Cui, W. 1999, ApJ, 512, 793

Ichimaru, S. 1977, ApJ, 214, 840

Kroon, J. J., & Becker, P. A. 2014, ApJL, 785, L34

Jokipii, J. R. 1987, ApJ, 313, 842

Kennel, C. F., & Coroniti, F. V. 1984, ApJ, 283, 710

Komissarov, S. S. 2013, MNRAS, 428, 2459

Komissarov, S. S., & Lyutikov, M. 2011, MNRAS, 414, 2017

Krall, N. A., & Trivelpiece, A. W. 1986, Principles of Plasma Physics (San Francisco: McGraw-Hill)

Lemoine, M., & Waxman, E. 2009, JCAP, 2009, 9

Ling, J. C., Wheaton, W. A., Wallyn, P., et al. 1997, ApJ, 484, 375

Lyubarsky, Y. E. 2003, MNRAS, 345, 153

Malzac J., & Jourdain, E., 2000, A&A, 359, 843

Mayer, M., et al. 2013, ApJ Letters, 775, L37

Merloni, A., Heinz, S., DiMatteo, T. 2003, MNRAS, 345, 1057

Meyer, M., Horns, D., & Zechlin, H. S. 2010, A&A, 523, A2

Meyer, F., Liu, B. F., & Meyer-Hofmeister, E. 2007, A&A, 463, 1

Miyamoto, S., Kitamoto, S., Mitsuda, K., & Dotani, T. 1988, Nature, 336, 450

Miyamoto, S., Sayuri, I., Shunji, K., et al., 1993, ApJL, 403, L39-L42

Montani, G., & Bernardini, M. G. 2014, Physics Letters B, 739, 433

Mori, K., et al. 2004 ApJ, 609, 186

Mushotzky, R.F., Done, C., & Pountds, A.K. 1993, Annu. Rev. Astron. Astrophys., 31, 717

Nowak, M. A., Vaughan, B. A., Wilms, J., Dove, J. B., & Begelman, M. C. 1999, ApJ, 510, 874

Nowak, M. A., Wilms, M., Hanke, K., et al., 2012, Mem. S.A.It., 83, 202

Park, B. T., & Petrosian, V. 1995, ApJ, 446, 699

Payne, D.G. 1980, ApJ, 237, 951

Pietrini, P., & Krolik, J. H. 1995, ApJ, 447, 526

Poutanen, J., & Fabian, A. C. 1999, MNRAS, 306, L31

Reif, F. 1965, Fundamentals of Statistical and Thermal Physics (New York: McGraw-Hill)

Rees, M. J., & Gunn, J. E. 1974, MNRAS, 167, 1

Remillard, R.A., & McClintock, J.E., 2006, Annu. Rev. Astron. Astrophys., 44:49-92

Rybicki, G. B., & Lightman, A. P. 1979, Radiative Processes in Astrophysics (New York: Wiley)

Sironi, L., Keshet, U., & Lemoine, M. 2015, SSRv, in press

Sironi, L., & Spitkovsky, A. 2014, ApJ, 783, L21

Schnittman, J. D., Krolik, J. H., & Noble, S. C. 2013, ApJ, 769, 156

Slater L. J. 1960, Confluent Hypergeometric Functions. (Cambridge: Cambridge Univ. Press)

Steinacker, J., & Schlickeiser, R. 1989, A&A, 224, 259

Sunyaev, R. A., & Titarchuk, L. G. 1980, A&A, 86, 121

Striani, E., et al. 2013, ApJ, 765, 52

Tachibana, Y., Kawamuro, T., Ueda, Y., et al., 2016, Publ. Astron. Soc. Jpn., doi:10.1093/pasj/psw001

Tananbaum, H., Gursky, H., Kellogg, E.M., et al. 1972, ApJ, 174, L143-L149

Thorne, K.S., Price, R.H. 1975, ApJL, 195, L101

Uttley, P., Wilkinson, T., Cassatella, P., et al. 2011, MNRAS, 414, L60

van der Klis, M., Hasinger, G., Stella, L., et al. 1987, ApJL, 319, L13

You, B., Cao, X., & Yuan, Y.-F. 2012, ApJL, 761, 109

Yuan, F., Cui, W. 2005, ApJ, 629, 408

Yuan, F., Yu, Z., & Ho, L.C. 2009a, ApJ, 703, 1034

Yuan, F., Narayan, R. 2014, Annu. Rev. Astron. Astrophys., 52, 529

Zdziarski, A. A., Gierlinski, M., Mikotajewska, J., et al. 2004, MNRAS, 351, 791

Zoghbi, A., Uttley, P., Fabian, A.C. 2011, MNRAS, 418, 2642

Curriculum Vitae

John J. Kroon graduated from Mt. Vernon High School, Fairfax County, Virginia, in 2006. He received his Bachelor of Science from James Madison University, Rockingham County in 2010. He received his Master of Science from George Mason University in 2013.